Cape Peninsula
University of Technology

The design and kinematic modelling of a novel single-sensor three-dimensional coordinate measuring machine

By

Bandile Jama

Thesis submitted in fulfilment of the requirements for the degree

Doctor of Engineering in Mechanical Engineering

In the Faculty of Engineering and the Built Environment

At Cape Peninsula University of Technology

Supervisor: Dr Ali Rugbani

Bellville
2024-01-30

Declaration

I, Bandile Jama, declare that the contents of this thesis represent my own unaided work and that the thesis/dissertation has not previously been submitted for academic examination towards any qualification. Furthermore, it represents my own opinions and not necessarily those of the Cape Peninsula University of Technology.

Signature: _____   Date: _____2024-01-30_____

Abstract

Traditional measuring equipment such as callipers, gauges and micrometres are well-known measuring instruments and they have been trusted for decades by industries to perform dimensional measurements. However, in situations where complex shapes or less uncertainty is required a unique but more advanced metrology system such as a coordinate measuring machine (CMM) is employed to provide a solution.

CMMs are highly recommended measuring equipment because of their versatile capabilities, measuring flexibility and measurement setup that is easy to perform. They have displayed potential for automated measurement, reverse engineering, and the ability to be integrated with computer design and manufacturing systems.

The new developments towards miniaturization and the changes in technical specifications from foundries and aerospace, automotive, medical, semiconductor, electronic, and other manufacturing industries have driven the need for CMMs with less uncertainty. Therefore, to keep up with miniaturization and the technical specification changes of parts, a fast three-dimensional (3D) CMM with acceptable uncertainty becomes necessary.

The industry has presented unique developments of CMMs with great speed at micro and nanometres accuracy. These designs have demonstrated potential for further innovation(s) to reduce the manufacturing cost of the machines. Thus, this study proposes a novel CMM design that has the potential to measure 3D objects using only one displacement sensor without compromising the Abbe principle.

The novel CMM design discussed in this study considers the conceptual bases of the ultra-precision CMM by reducing the number of displacement sensors or interferometers from three to one while achieving micrometre measurement uncertainty. To satisfy these conditions, the design incorporates Abbe's principle as the fundamental basis to achieve positioning accuracy. Also, the metrology frame and structural frame are separated to allow for optimising the design.

The design suggests a workpiece supported by the mirror table and is translated into the x and y-axis by the manipulation system. The mirror is positioned at 45° to the vertical axis of the mirror table, and towards each plane surface of the coordinate system. The displacement sensor is mounted at 45° at the lower end of the vertical member of the metrology frame while the probe is fixed at the horizontal end. The functional line (laser beam) of the displacement sensor is always fixed to the tip of the probe. This configuration allows the alignment to be maintained and fulfil Abbe's fundamental requirements in all translations of the machine in a global coordinate system. The mirror is perpendicular and always intersects the laser beam at a gap distance between the displacement sensor and the probe.

The kinematic and error modelling were developed to determine the positioning of the probe and the out-of-squareness of the mirror respectively. During the measurement process, the probe approaches the workpiece at a gradually decreased speed. This is achieved by dividing the travel distance until the probe contacts the workpiece, and a signal will command the motor to stop. The position of the probe is computed after every movement by solving a kinematic model. This is supported by understanding the direction of the translation, and the distance between the displacement sensor and the mirror.

Therefore, the experiment was performed to validate the proposed kinematic model and the out-of-squareness of the mirror. During the experiment, the machine was employed to measure a calibrated gauge block from Matrix-Pitter with Grade 1. The developed kinematic model was proven to be relevant in determining the position of the probe. With a measurement standard deviation of 0.012, 0.016, and 0.018 mm on the x, y, and z-axis respectively.

Dedication

To the love of my life "my wife" Amanda "Linathi" Jama, and my beautiful kids,
Iminathi, Imibongo and Imiyalo

for their love, support, and encouragement.

I Love You

Acknowledgements

I wish to thank:

Table of content

List of Figures

xiv

List of tables

List of abbreviations

CAD	Computer Aid Design/Drawing
CAGR	Compound annual growth rate
CMM	Coordinate Measuring Machine
CNC	Computer Numerical Control
DAQ	Data Acquisition Cards
DAS	Data Acquisition System
DH	Denavit-Hartenberg
DMT	Dissociated Metrological Structure
DoF	Degrees of Freedom
GRBL	Open-source software used as motion control for an Arduino
GUM	Guide to the Expression of Uncertainty in Measurement
HTM	Homogeneous Transformation Matrix
LED	Light-Emitting Diode
LOM	Light optical Microscope
MAS	Multi-Axis System
MC	Monte-Carlo Simulation
MDF	Medium Density Fiberboard
MEMS	Micro Electromechanical System
Micro-CMM	Micro-measurement Coordinate Measuring Machine
NEMA	National Electrical Manufacturers Association
OEM	original Equipment manufacture
PE	Precision Engineering
ROI	Return on Investment
SEM	Scanning Electron Microscopy
SMEs	Small and Medium-Sized Enterprises
SPM	Scanning Probe Microscope
USB	Universal serial bus
USD	United States Dollar

Nomenclature

α	the angle of the mirror on the horizontal axis
β	the angle of the mirror on the vertical axis
Θ	the angle of the displacement sensor in a horizontal position.
Φ	the angle of the displacement sensor a in vertical position.
T_{mi}	distance travelled by the machine/mirror
T_{ti}	difference between the initial and new laser beam measurement
e_i	error of the mirror in x, y and z axis
L_0	is a laser beam measurement
L_{0x}	laser beam measurement when the machine is translated into the o x-axis
L_{0y}	laser beam measurement when the machine is translated into a y-axis
L_{0z}	laser beam measurement when the machine is translated into a z-axis
N	number of bodies
M	degrees of freedom
j	number of joints
fi	freedom of the ith joint
x, y, z	*global* coordinates of the machine
$P_i\ (x_i,\ y_i,\ z_i)$	position of the probe in the global coordinate system
$P_x\ (x_i,\ y_0,\ z_0)$	position of the probe when translated into x-axis
$P_y\ (x_0,\ y_i,\ z_0)$	position of the probe when translated in y-axis
$P_z\ (x_0,\ y_0,\ z_i)$	position of the probe when translated in z-axis
$a_i\ (x_i,\ y_i,\ z_i)$	Original position of the global coordinate system
$a_x\ (x_i,\ y_0,\ z_0)$	Change in original position when translated in x-axis

$a_y (x_0, y_i, z_0)$ Change in original position when translated in y-axis

$a_z (x_0, y_0, z_i)$ Change in original position when translated in z-axis

Metrology Glossary

Accuracy: Is the degree of approximation between the measurand and the accepted standard value [1]. Raghavendra and Krishnamurthy [2] defines accuracy as the maximum amount by which the result differs from the standard acceptable value.

Alignment: The line of measurement and the line of dimension being measured should be coincident. This is a basic principle for good design to ensures accuracy and reliability of measurements [2].

Calibration: Can be define as means to achieving traceability. It is a procedure used to establish a relationship between the values of the quantities indicated by the measuring instrument and the corresponding values realized by standards under specified conditions [2].

Dimensional Inspection: The physical measurement such as sizes, distances, angles, form, or co-ordinates of a feature on an artefact [3].

Dimensional Metrology: The science and application of physical measurement, such as length, area, volume, flatness, and roundness [4].

Maximum Permissible Error: The maximum value of the measurement error, compared to the given reference value, permitted by specifications or regulations for a given measurement, measuring instrument, or measuring system [5] [6].

Measurement Result: The measurand quantities obtained from a measurement. Environmental conditions or measurement uncertainty are two examples of other relevant information [6] [7]

Measurement Traceability: The property of a measurement result whereby the result can be related to a reference through a documented unbroken chain of calibrations, each contributing to the measurement uncertainty [6].

Measurement Uncertainty: An estimate of the uncertainty of a measurement, usually in metrology it refers to measuring equipment uncertainty [6] [8].

Measurand: A physical quantity intended to be measured such as mass, force, length, etc., in dimensional metrology. It can also be defined as a feature of an object being measured [7].

Precision: The ability of the measuring instrument to repeat the same results during the act of measurements for the same quantity it is known as repeatability [2].

Probe: The touch trigger probe is recently the most used type of probe in CMM. It has a precision-built-in and touch-sensitive device that generates an electronic signal through probe tip contact with the specimen surface, which is usually indicated as visual LED and an audible touch signal. The probe head itself is mounted at the end of one of the CMM's moving axes; it can be rotated automatically, and many different probe stylus tips can be accommodated and attached [9].

Resolution: The small change in a quantity being measured that causes a noticeable change
in the corresponding indication [6] [8].

Reverse Engineering: Reverse engineering, is a process in which software, machines, aircraft, architectural structures, and other products are deconstructed to extract design information from them [10]. The reverse engineering process enables one to determine how a part was designed so that it can be recreated. Companies often use this approach when purchasing a replacement part from an original equipment manufacturer (OEM) is not an option [11].

Verification: The proof, that an item meets the specification requirements. In dimensional inspection the object's dimensions would be measured and compared to the drawing or computer-aid drawing (CAD) model of the object [10].

Abbe's effect: This principle states that to improve measurement accuracy, the measurement target and the scale of the measuring instrument must be placed in a collinear fashion in the measurement direction [12] [13].

Coordinate measuring machine: A three-dimensional (3D) machine that measures the geometry of physical objects by sensing discrete points on the surface of the object with a probe. [14].

Degrees of freedom: The number of independent parameters that define the motion possibilities of rigid bodies.

Forward Kinematics Model: A technique applied to formulate the position and orientation of the end effector when the values of the angles of the joints are given [15] [16] [17].

Error Modelling: In ideal situation when performing the measurements, the workpiece should coincide with the probe at the specific point. However, due to errors, they meet at another point. According to the difference between the two points, a model can be established to improve the precision of the machine [18].

Inverse Kinematics Model: It is an inverse of forward kinematic modelling. The model suggest the position and the orientation of the end effector are given to calculate the angles of the joint [15] [16] [17].

Kinematics Model: A kinematic model describes the motion of a robot in mathematical form without considering the forces that affect motion and concerns itself with the geometric relationship between elements [15].

Metrology: The science of measurement [6]. Metrology may be divided depending upon the quantity to be measured such as metrology of length, metrology of time. Metrology includes all theoretical and practical aspects of measurement, whatever the measurement uncertainty and field of application [7].

Chapter 1:

Introduction and Background

1. Introduction and Background

1.1 Introduction

Coordinate measuring machines (CMMs) are mechanical devices that are used for 3D inspection of physical components in manufacturing industries. CMMs includes the movement of measuring probe to determine the coordinates of discrete points on work piece surfaces [19]. Unlike the traditional measuring method such as callipers, gauges, and micrometres etc, CMM is employed where a unique but more complex metrology system is required to provide a solution [20]. CMMs consists of four major functional components; including the main structure, the metrology system, the computer interface system, and the software to perform measurements [19]. The design and the configuration of the components varies depending on the required metrology arrangement and automation systems. According to Cheng *et al* [21] coordinate measurement technology is the most common and fundamental measurement technology in the field of modern machinery manufacturing, especially in aerospace, automobile manufacturing, mould processing, and other industries.

The first CMM was introduced in the late 1950s when they first appeared at the international machine tool exhibition in Paris, and gradually introduced into the manufacturing industries in the early 1960s [22]. When the touch-trigger probe was introduced by Renishaw in the 1970s, the application of CMMs grew and swiftly attracted manufacturing companies [22].

The design of CMMs consists of four major functional components which include the main structure of the machine, the metrology system, the computer interface system, and the software to perform measurements [19]. These components can be designed and configured depending on the required metrology and automation systems. Generally, the workpiece is fixed on a measuring table/stage, with a probe mounted on the metrology system to determine the discrete coordinates on the surface of the workpiece [19] [23]. CMM applications include geometric measurements, positioning measurements, profile

measurements, reverse engineering, and prototyping. Figure 1-1 illustrate the types of CMM machines and the definitions are given in Table 1-1 as defined by [24]. [25].

Figure 1-1: Typical conventional CMMs; (a) Horizontal arm, (b) Column type, (c) Gantry, (d) Cantilever, and (e) Bridge type.

Table 1-1: The description of different types of CMM machines.

(a) Horizontal arm	Unlike other CMM types that hold the probe vertically, the horizontal arm mounts theirs' horizontally. These CMMs are employed to measure long and slender parts. They are less accurate compared to others.
(b) Column type	The ram of the column CMM moves vertically with a fixed column. The workpiece to be measured is placed on the manipulation system which is moving in x and y directions.
(c) Gantry type	Gantry types are mostly used to measure large products such as automobiles. These designs do not require the lifting of parts to be placed on the table. They are expensive compared to others because of the size of the machine.
(d) Cantilever	They are less rigid compared to other machines since they are supported at one point. They measure small parts while providing three accesses to the part.
(e) Bridge type	Bridge-type CMMs are classified into moveable tables and moveable bridges. They are stable during the measurements and can measure small and medium parts that can fit the machine.

In principle, the workpiece is placed on a manipulated table/stage, with a probe secured to the metrology system [23]. When the probe encounters a workpiece it triggers, and the machine is activated to take samples from the measuring system on machine axis. The samples are translated to the global coordinate system of the machine to determine the coordinates of the triggered location(s). When the full representative points are recorded, the data gets converted into the numerical model through a computer interface into physical measurement data. This application includes the geometric measurements, positioning measurements, profile measurements, reverse engineering, and prototyping. According to Cheng *et al* [21] coordinate measurement technology is the most common

and fundamental measurement technology in the field of modern machinery manufacturing, especially in aerospace, automobile manufacturing, mould processing, and other industries.

Figure 1-2 shows a typical application of CMMs, where at (a), the real object is probed in discrete positions with a sound representative sample, at (b) developed a numerical model of the part from the samples registered, and (c) compute the physical dimensions of parts using the positioning samples from (a). The more points taken/probed almost to an infinite number on the workpiece the better the representation of the measurement [26] [27].
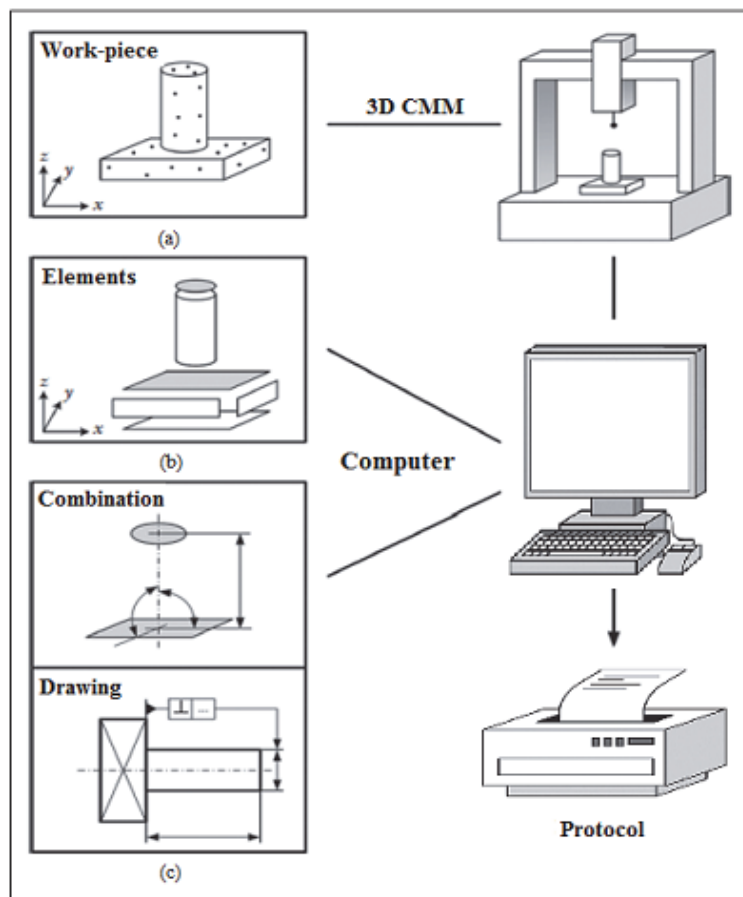
Figure 1-2: The representation of the typic CMM measurement process [27].

There are two architectural concepts for the movement of a CMM probe: serial link manipulation and parallel manipulation. Serial link manipulators are widely used for the design of measuring machines [28]. The system members are stacked connected to each

other like a chain and orthogonal to create three axes. The probe location is determined by reading the travel distance of each axis. If one link causes a measurement error, it is directly propagated through the entire system [29]. According to Takamasu *et al* [30], the traditional CMM is based on a serial link manipulation, components from base unit to an end-effector (the measuring probe) are connected serially.

Parallel manipulator components are related, and errors are not cumulative and amplified. They have higher structural rigidity than the serial CMMs, since the end-effector is simultaneously carried by several legs in parallel [30] [31] . Parallel manipulators consist of several links connected in parallel to create a closed-chain structure with a moving platform and a fixed base, connected by several links. Each link is directly connected to the probe resulting in zero accumulation of errors. The probe position is determined by solving the relatively complex kinematics of the closed chain mechanism [29, 32].

CMMs are constrained by the background vibration levels, environmental conditions, metrology system accuracy, structural deformations, etc. These limitations vary depending on the type of CMM and the operating conditions. Structural deflection is always an important limiting element because it introduces an error in the indicated position of the part sensor. The resolution and the capability to provide precise research to resolve the measurement issues is limited by the specification and cost of the CMM components. Thus, this study proposes an invention of a novel serial link manipulation design for a single sensor 3D CMM as an initiative to minimizes capital cost of the machine by reducing the number of costly machine components.

1.2 Background of the study

Coordinate Measuring Machines (CMM) have successfully superseded traditional measuring techniques, resulting in reduced quality control operations, time, and effort [33]. They have displayed the potential for automated measurements, reverse engineering, and the ability to be integrated with computer manufacturing systems [33] [34].

The new developments towards miniaturization and the changes in technical specifications from foundries and aerospace, automotive, medical, semiconductor,

electronic, and other manufacturing industries have driven the need for CMMs with less uncertainty [33] [35]. Therefore, to keep up with the miniaturization developments, while observing the upcoming market demands, the industry is engaging in the development of fast 3D CMMs for measuring small products in an array with nanometre uncertainty [20] [33] [35] [36]. These include ear implants or hearing aids, gears of micro motors, small freeform lenses of mobile phones, injection systems for the automotive industry, or in the telecom sector for fibre optic or next-generation radio frequency technology components [37], see Figure 1-3.

Microturbine   Array of needles   Pennymotor within bearing   Piezo motor
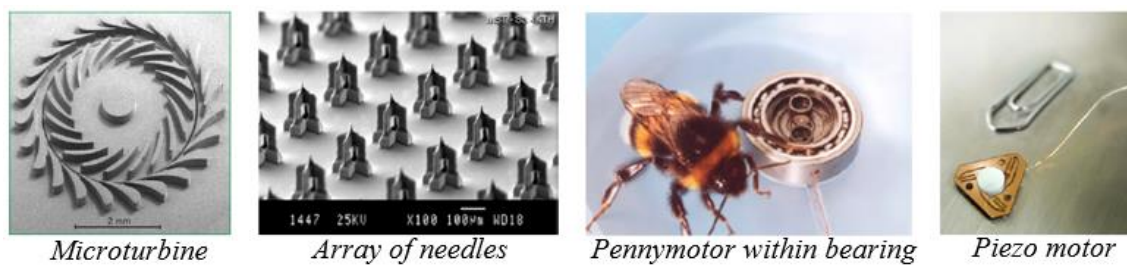
Figure 1-3: The example of micro and nano components [38].

Such micro parts are often complex and too large for optical microscopy techniques and their tiny structures are hardly accessible through conventional tactile coordinate measuring machines. [35] [39]. According to Cao *et al* [40] and Yang *et al* [36], conventional measuring methods cannot meet these requirements because the measurement scales of conventional coordinate measuring machines (CMMs) are usually limited to several tens of millimetres or more, which is not suitable for measuring small parts of the order of sub-millimetres or even sub-micrometres. In addition, conventional CMMs lack good 3D measurement uncertainty levels and are often not supplied with the proper probing systems in many applications.

The conventional CMMs includes three perpendicular travelling orthogonal axes x, y, and z, mounted with the linear measurement transducers to physically describe the reference coordinate system with the probe system attached to the third moving z axis [41] [42]. When the probe stylus contact the workpiece it triggers, then the machine samples the three position linear measurements of the transducers (through the encoders mounted in each moving axis), and translates to the cartesian coordinate system (x, y and z) the measurement of the location of one point on the object's surface [43]. Figure 1-4 is a

typical bridge type CMM, other types include the conventional CMMs such as horizontal arm, gantry type, cantilever, and bridge type.

The metrology system is the interaction of the various parts of the CMM machine that work together to sense different parameters/coordinates of a workpiece required for the calculation of measurements. The arrangement of the metrology system and the type of parts used vary per the design of CMM. With conventional CMMs, the metrology system includes the three perpendicular travelling orthogonal axes x, y, and z, mounted with the linear measurement transducers to physically describe the reference coordinate system with the probe system attached to the third moving z-axis [44] [36].
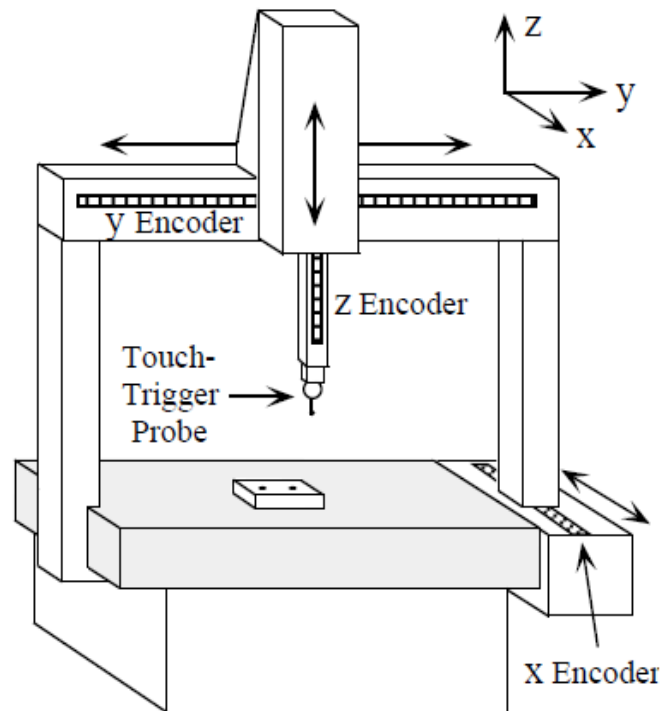
Figure 1-4: Typical positioning of the conventional CMM measuring system [45].

Since the development of the conventional CMM there have been several novel CMMs with different metrology systems developed with accuracy in the order of tens of nanometers [35] [38]. In 1999, Peggs *et al* [46] designed a compact highly accurate CMM

with a reference corner mirror closer to the CMM probe, see Figure 1-5 . The system employs three laser interferometers and three autocollimators to measure the position of the probe. Peggs *et al* [46] extended a commercial CMM with a 6D interferometric measurement system, which accurately determined the probe's position relative to the workpiece. This novel design reduces the Abbe offset, thus offering high 3D measurement accuracy (estimated as 50 nm at the 95% confidence level) over a measurement volume of 50 x 50 x 50 mm^3. Autocollimators are used to measure the angular deviations of the mirrors to compensate for Abbe's errors. Each autocollimator uses a laser beam that reflects from the measurement mirror. The position of this beam onto a 4-quadrant photodetector is used to calculate the angular variations.
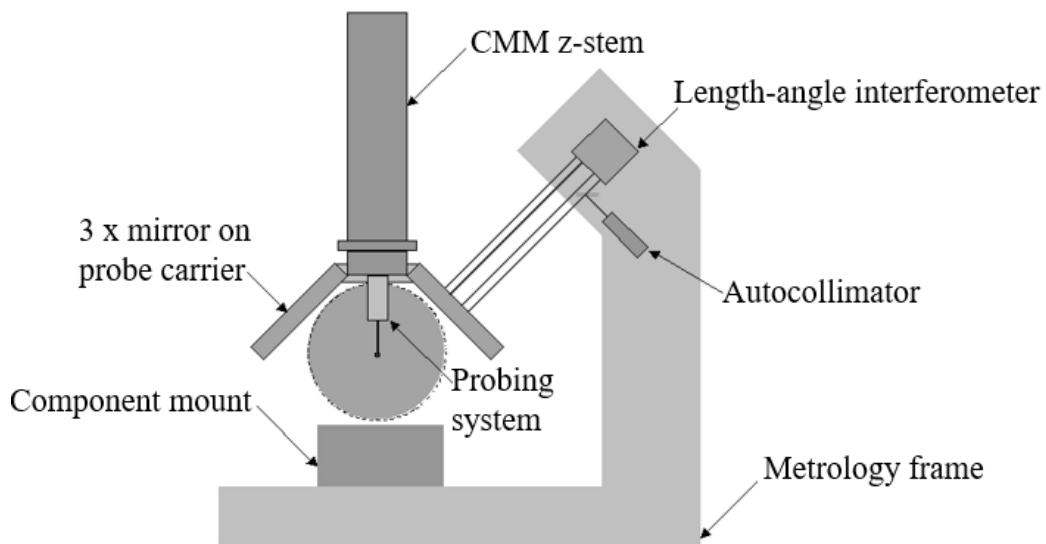
Figure 1-5: A Schematic view of a compact high-accuracy CMM by Peggs *et al* [46].

To improve the conventional CMM accuracy, Vermeulen [47] separated the machine slides from the vertical direction and had the horizontal slides supported independently in the vertical direction and constrained by separate parallel paths. Vermeulen designed a 2D concept of the metrology system that uses optical linear encoders mounted on two intermediate bodies to measure the position of the probe. This arrangement eliminates

Abbe's errors on the x and y-axis. Vermeulen further integrated two design concepts to measure the third measuring axis (vertical z-axis) called "pinhole", see Figure 1-6. A similar design to that of Vermeulen was employed by Seggelen [20] for a design with a low moving mass in all directions. The design was intended for measuring micro products in an array setup with a vertical stroke limited to 4 mm.
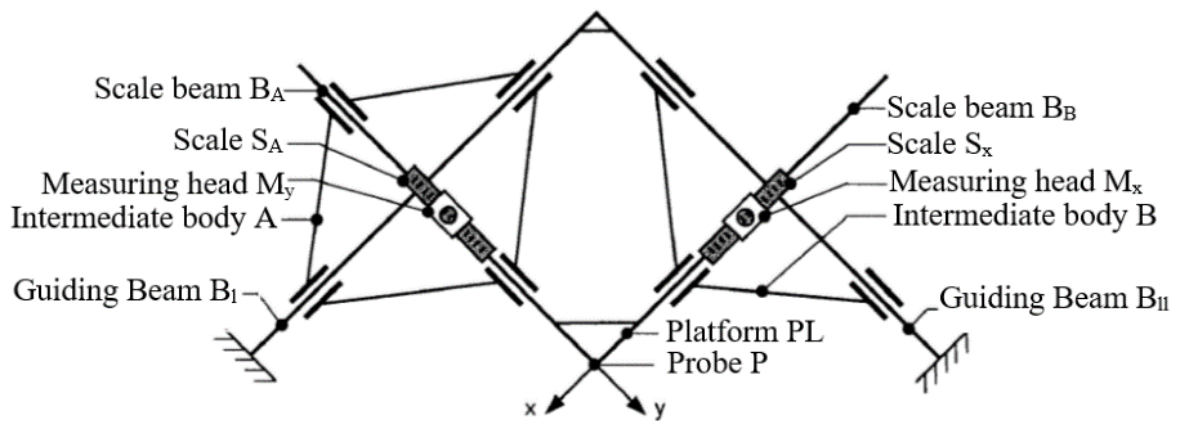
Figure 1-6: The 2D concept of the metrology system [47].

Ruijl and Eijk [48] developed an ultra-precision CMM which was further commercialized as ISARA400 [49]. ISARA400 features include a volume measurement of 400 x 400 x 100 mm and a volumetric (3D) measurement uncertainty of 100 nm (2σ). This ultra-precision CMM has been realized and is currently operational at IBS Precision Engineering. Figure 1-7 is a typical ultra-precision CMM design by Ruijl and Eijk [48]. The workpiece is secured and supported by the mirror table. The position of the probe in the global coordinate system is measured using three laser interferometers. The functional lines of the laser interferometers are fixed to the tip of the probe to comply with Abbe's principle. The laser interferometers and the probe are secured to a common metrology frame, to maintain the alignment in all measurement directions [48].
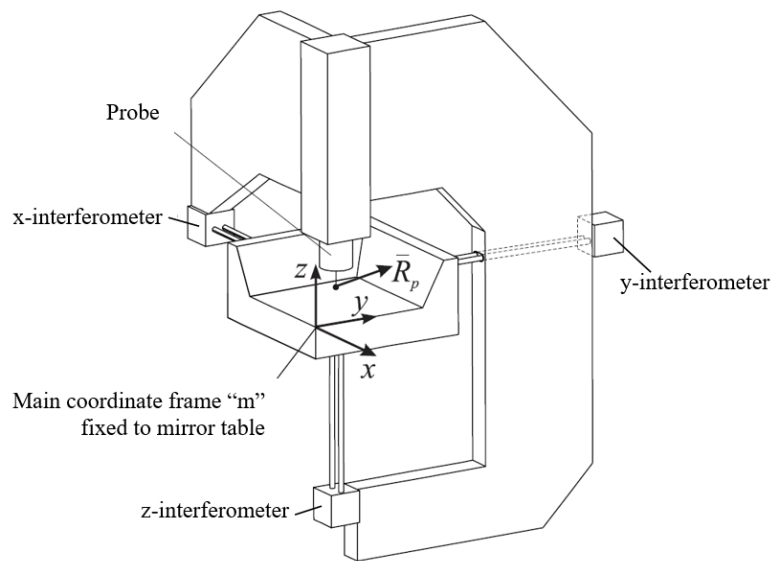
Figure 1-7: Ultra precision coordinate measuring machine metrology system [48].

The Molecular Measuring Machine (M3) was developed by the National Institute of Standards and Technology (NIST) [37]. M3 is a scanning probe microscopy (SPM) based metrology instrument that is designed to achieve sub-nanometer resolution with its probe and metrology system, over a macroscopic area of 50 x 50 mm². M3's goal was to achieve 1 nm combined uncertainty for point-to-point measurements within the working area. The M3 design considerations for sub-nanometer scale metrology over centimeter scale areas and the large range-over-resolution goal are vibration isolations, machine stiffness and low noise in the control electronics, which together are needed to minimize the positional noise. Then to achieve measurement accuracy, the design considers the motion accuracy and repeatability, and high-stability temperature control to minimize measurement uncertainty due to thermal expansion effects. The M3 design operates in a vacuum environment to reduce sample contamination and adsorbed overlayers, and to remove measurement errors in the interferometers due to changes in the refractive index of the ambient air.

Fan *et al* [50], designed a high precision low-cost micro-CMM with an expected measuring range of 25 x 25 x 10 mm³ and resolution of 1 nm, and 30 nm repeatability. The design consideration includes the arch-shape bridge for better stiffness and thermal

accuracy, co-planar stage for less Abbe error, diffraction gratings with interferometric fringes and subdivision technique for nanometer resolution, and the focusing probe on the laser interferometer feedback spindle to guarantee nano-meter stability. Fan *et al* [50] proposed an innovative co-planar stage where the top table is moved in the x-direction along the guideway mounted onto the frame, and the frame is moved in the y-direction along the precision ground rods of the base. Four guiding rods (two for the upper axis and the other two for the lower axis) are in the same plane, which means they share the same vertical height, and thus reducing the Abbe error in the vertical direction. Fan *et al* [50] further presented the design considerations of a novel micro precision CMM with a measurement volume of 25 x 25 x 10 mm^3, with a force-balanced structure to yield high stiffness and conforms to the Abbé principle in 3D space. Driven by the ultrasonic nanomotor and fed back by the hologram scale, each axis can achieve a 1nm resolution. Fan *et al* [51] performed a finite element analysis comparing the rectangular, arch and pagoda bridge, and the results showed the pagoda bridge as a preferred structural system, due to its symmetrically constructed structure with forced balance. This pagoda bridge has a force-balanced structure in all directions.

The National Institute of Advanced Industrial Science and Technology (AIST) have developed a novel high-precision micro-CMM called M-CMM with a moving volume of 160 x 160 x 100 mm^3 (x, y and z), aiming to achieve a measuring uncertainty of 50nm measurement uncertainty with a measuring volume of 30 x 30 x 10 mm^3 (x, y and z) [36]. The M-CMM configuration comprises three main parts: a cross x, y, and z-axis, and a probe unit. Each axis has a linear motion stage system that comprises air-bearing sliders, a glass linear scale, a moving table, a driving motor. Linear motion stage systems have been successfully employed in precision measurement systems because of the lack of friction in the air-bearing sliders. In addition, the linear scales feedback the position signal within the range of the nano-meter resolution. The design considerations for M-CMM design as an initiative to reduce thermal effects include the main structure made of alumina ceramic having high rigidity and low coefficient of thermal expansion (CTE; 7 ppm/K), and the base plate is made of granite having (CTE of 5 ppm/K). The measurement area is covered with an enclosure to minimize heat inputs from the machine environment. The x, y and z-axis are separated into two mechanical parts: the x-y linear stages stacked and the z-axis, which is separately designed and constructed at the center

of the frame table. The primary reason for this division is that the measurement uncertainties of the z-axis are larger than those of the x and y-axis This discrepancy is attributed to the lower sensitivity of 3D contacting micro-probes in the z-direction compared to the x and y plane. This reduced sensitivity is, in turn, influenced by the effect of the length of the probe stylus on the horizontal probing direction.

Despite these advancements, challenges persist, including the high cost associated with achieving high precision. Precise CMMs often involve advanced technologies, high-quality components, and sophisticated calibration processes, making them financially prohibitive for small and medium-sized enterprises (SMEs) or budget-constrained industries. Therefore, there is a need for cost-effective alternatives that can deliver comparable levels of precision. This research aims to develop a novel CMM system that incorporates a single displacement sensor while adhering to fundamental metrology principles. By reducing the number of costly machine components, the objective is to maintain accuracy and reduce costs, contributing to the progression of metrology techniques in manufacturing industries.

The proposed concept in this study demonstrates a possible alteration of an ultra-precision CMM such as ISARA 400, see Figure 3-1. The novel CMM design includes the measuring system that provides 3-D measurements using one displacement sensor instead of three measuring units as it is with conventional CMMs, other micro-CMMs and ultra-precision CMMs. The study describes the novelty of having a single displacement sensor placed in a position at an angle of 45º to each plane surface (x-y, x-z, and y-z) pointing directly towards the probe's tip at a fixed distance, hence theoretically complying with Abbe's principle. The position of the probe in the global coordinate system was identified by solving the kinematic model. The proposed concept might stimulate in a small way more research towards accuracy improvement.

The design considerations required to archive small measuring uncertainty should include Abbe's principle as the fundamental basis of achieving high positioning accuracy [48] [35], and the separation of the metrology frame and structural frame of the machines [48] [28]. Further, the thermal distortion of the machine structure is considered an important aspect, it is not discussed in this study; however, it is highly recommended as a follow-up study since it is viewed by Bryan [52] as one of the main contributing error sources.

13

This section will further discuss the ability of the machine to calibrate the geometric deviations of the metrology system and evaluate the measurement uncertainty.

1.3   Objectives of the research

The main objective is to demonstrate a potential novel CMM design, with acceptable uncertainty and capability to measure a 3D workpiece using a single distance sensor. The design considers a complete prototype of the machine, including a structure for better stiffness, stability, and adherence to Abbe principles. The kinematic model is employed to compute the positioning of the probe. In particular, the study has the following sub-objectives:

- A design to consider the separation of the measurement and movement loops to minimise the effects of vibrations and heat dissipation.
- Develop a kinematic model to determine the position of the probe.
- Formulate an error modelling technique for mirror out-of-squareness.
- An experiment to determine the effectiveness of kinematic modelling.
- Identify geometric parameters, such as the machine dimensions, distances, parallelism of trajectories, angle, and uncertainty due to inaccurate manufacturing and assembly as well as to deviation range in movement.
- Experimental tests to confirm the results and validate the concept.
- Perform the calibration of the mirror out-of-squareness.

1.4   Organisation of the report

Chapter 1   Provides a brief description of measurements and introduces the coordinate measuring machine. It also discusses the importance of CMMs, including the historical developments, and provides a background study of the report.

Chapter 2:   Discuss the design considerations of the machine, to ensure that the objective of achieving small positioning or measuring uncertainty is met.

Chapter 3:   Presents the design and the construction of the novel CMM prototype discussed in this study. It includes the machine structure, metrology frame, and manipulation system. It further discusses the integration and the advantages and disadvantages of the system.

Chapter 4:   The development of the kinematic model to determine the position of the probe. It further explains the coordinate system, including the movement of the machine and the kinematic error modelling.

Chapter 5:   This chapter discusses the development of the mirror out-of-squareness kinematic model.

Chapter 6:   Is the experimental evaluation and the calibration of the mirror out-of-squareness using the Monte Carlo Simulation?

Chapter 7:   Is the experimental evaluation where the novel CMM is used to measure the gauge blocks in x, y and z-axis to validate the kinematic model. The performance measurements are evaluated utilizing repeatability measurements. The study further compares the results of the novel CMM in discussion with the conventional CMM

Chapter 8:   Discuss the conclusions and the recommendation of the possible project to be considered to take this initiative to the next level.

Chapter 2:

Novel CMM Design Considerations

2. Design consideration

2.1 Introduction

This chapter presents a comprehensive description of the design considerations applicable to the novel CMM machine discussed in this study. The conceptual bases of the proposed design include the elements of ultra-precision machines, by Ruijl and Eijk [48]. These elements can be classified and designated to high repeatability, small geometric calibration uncertainty, and high predictability response to the main error sources. To archive these elements this study, consider Abbe and Bryan principle as the basis for the alignment of the measuring systems. It also considers separating the structural and metrology functions for design optimization. The considerations of the material selection, proper design of the geometric configuration and thermal insulation are important aspects to be considered to improve thermal distortions and the dynamic effects. However, they are discussed in this thesis. Lastly, the uncertainty analysis is considered as an important part of the design phase as well as the calibration systems and methods.

2.2 Alignment of the measuring system

CMM machines are subject to many factors that would lead to measurement errors, for example errors of the linear guides, deformation of machine parts due to finite stiffness, gravitational and driving forces, and temperature changes. These features cause unwanted translation and angular errors. Where the translational errors have direct effect on the measuring accuracy, angular errors act upon the measuring accuracy, through an offset between the slide and the end effector [47]. According to Ruij [53] the fundamental principle in achieving high positioning and measuring accuracy is the Abbe and Bryan principles.

Abbé's principle relates to accuracy when measuring dimensions and is said to be the basis of the measuring machine design [54], [55]. This principle states that; in order to improve measurement accuracy, the measurement target and the scale of the measuring

instrument must be placed in a collinear fashion in the measurement direction [54] [55] [53] [56]. This concept was acknowledged by Bryan [54] as the first principle of machine tool design and dimensional metrology. Bryan extended the concept to the straightness measurement and proposed the Bryan principle to state; the effective point of a straightness measuring system should lie along a line which is perpendicular to the direction of slideway travel and passes the functional point whose straightness is to be measured. If it is not possible, either the slideways that transfer the straightness must be free of angular motion or angular motion data must be used to calculate the consequences of the offset [54].

Given an example by Richard [13] Figure 2-1 is a typical unwanted angular slide-motion that demonstrate an Abbe error in the length measurement. Where the measurement distance occurs with an Abbe offset between the axis of measurement and the reflector axis (axis through the center of the probe ball, parallel to the measuring axis). An Abbe error arises in the nominal direction of the motion, due to an unwanted angular error. This is defined as the first principle of machine tool design and dimensional metrology [41]. The measurement error reflected on the standard scale is given by equation (1).

$$\varepsilon_{abbe\ error} = h_{abby\ offset} \times tan\theta \tag{1}$$
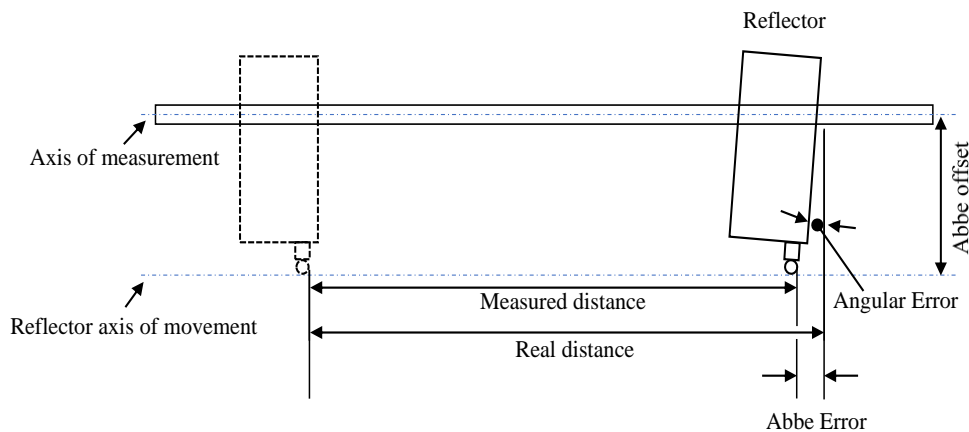
Figure 2-1: Typical angular slide-motion that demonstrate an Abbe error in the length measurement [13].

Figure 2-2 and Figure 2-3 show a typical 1-D working table with fixed work piece demonstrating Bryan measurement error in the vertical and horizontal direction (pitch and

yaw errors) respectively. The measured line is collinear with the standard scale in the contact measurement, so it is in line with the Abbe principle. When the working table moves toward the dotted position in the measurement, the working table rotates θ in the vertical plane due to the errors of rail and the rotating center is 0. Then, the measurement error reflected on the standard scale is presented by ΔA or $\varepsilon_{abbe\ error}$ as presented by equation 1. The distance h between the rotating center and the standard scale line is the first-order error arm. The laser beam is fixed to the tip of the probe with the same metrology frame.
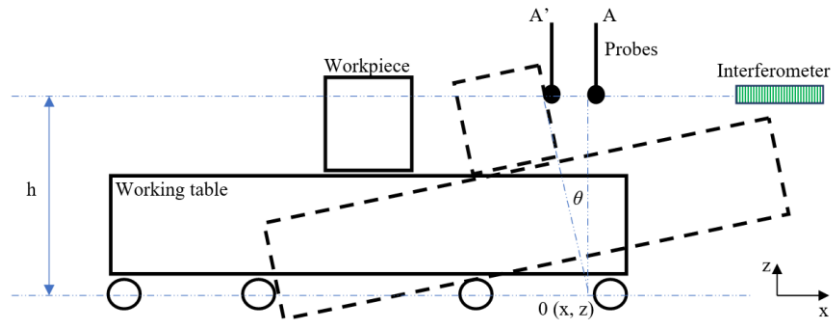
Figure 2-2: A typical Bryans measurement error in the vertical direction (pitch error) [41].
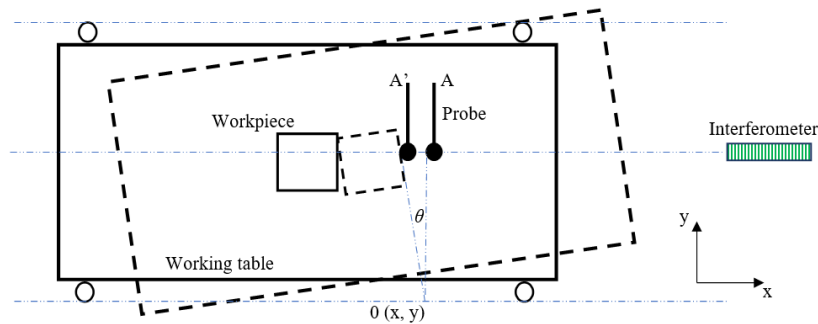
Figure 2-3: A typical Bryans measurement error in the horizontal direction (yaw error) [41].

Brayn [54] effectively generalized the Abbe Principle to state; "The displacement measuring system should be in line with the functional point whose displacement is to be

measured. If this is not possible, either the slideways that transfer the displacement must be free of angular motion or angular motion data must be used to calculate the consequences of the offset".

There have been developments to reduce Abbe error which included updating the machining procedure and manufacturing processes. However, according to Rujil [53], to obtain the correct alignment of the measuring system in a coordinate measuring machine, one has to consider the measuring principle of the machine presented in Figure 2-4. The metrology system consists of both measuring systems and probe systems attached to a common metrology frame. The functional line of the measuring system is fixed to the tip of the probe, and it is perpendicularly intercepted by the remote mirror. This concept is one of the most important metrological design principles that was maintained from the first Isara CMM to the design of the Isara 400 [49].
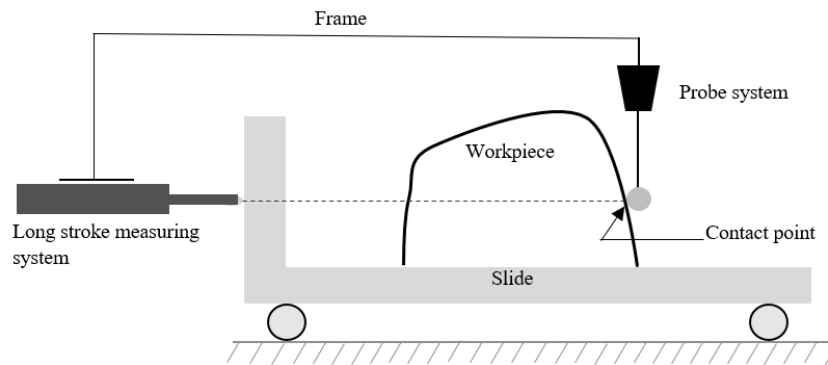
Figure 2-4: Measuring principle that adheres to Abbe's principle of a coordinate measuring machine along a single measuring axis [53].

This setup was applied by Nouira *et al* [57] during the setup of a high precision profilometer and comparison of tactile and optical measurements. The measuring single point scanning probe was collinear to the differential laser beam that materializes the measuring Abbe z-axis. The horizontal x- and y-laser interferometer beams and the touching element of the tactile probe or the focus point of the optical confocal chromatic probe are designed to be in the same x-y plane and on Abbe axes (both Abbe x-axis and Abbe y-axis). During displacements, the probe is always aligned with the Abbe axes

because the measuring probe and the x and y laser interferometers are fixed on the same Invar metrology frame.

The design for the novel concept discussed in this study is in line with the ultra-precision CMM by Rujil [53]. The measuring system and the probe are mounted to a common metrology frame and translated at the same time. With a single mirror attached to the manipulation system that translates along the x and y-axis.

2024

2.3 Separation of machine structure and metrology system

Two basic principles that needs to be considered to improve the performance of the metrology frames; the first one is the separation of the metrology loop from the structural loop, and the elimination of or accounting for Abbe offset errors [48] [58]. The Abbe error is discussed in the previous section 2.2. The separation of the metrology loop from the structural loop can also be referred to as dissociated metrological structure (DMT).

In principle the DMT is achieved when the performance of the metrology is not impacted by the behavior of the structural frame. Vissiere *et al* [59] presented a metrology loop with associated dissociated architecture (see Figure 2-5) of a conventional cylindricity-measuring machine. The metrology loop and the structural loop are separated with isostatic linkages that allow deformation to be prevented in the components of the metrology loop. According to Vissiere *et al* [59] the dissociated principle allows components of the metrology loop to be employed for the position information only. Thus, it is relieved of any other function, in particular the support function, and can be optimized. The aim for the dissociation is to prevent the measurement sensor(s) from deflecting with the machine due to thermal deformations, dynamic and static loads. The principle provides an opportunity to optimize and enhance the designs [49] [53]. The metrological linkages can communicate the probe position information in a much more repeatable way than any mechanical linkage since the metrological linkages are not sensitive to loads.

Bryan [60] presented an applied DMT with the design and the construction of an ultra-precision 2.134 m (84 inches) diamond turning machine, see Figure 2-6. The design

presented the machine mounted on an 80 tons granite base 6.4 x 4.6 x 1.5 m^3. With an independently supported granite metrology base which isolates the machine measuring systems, laser interferometers, and straightedges from the distortion of the machine base caused by changes in position of the slides.
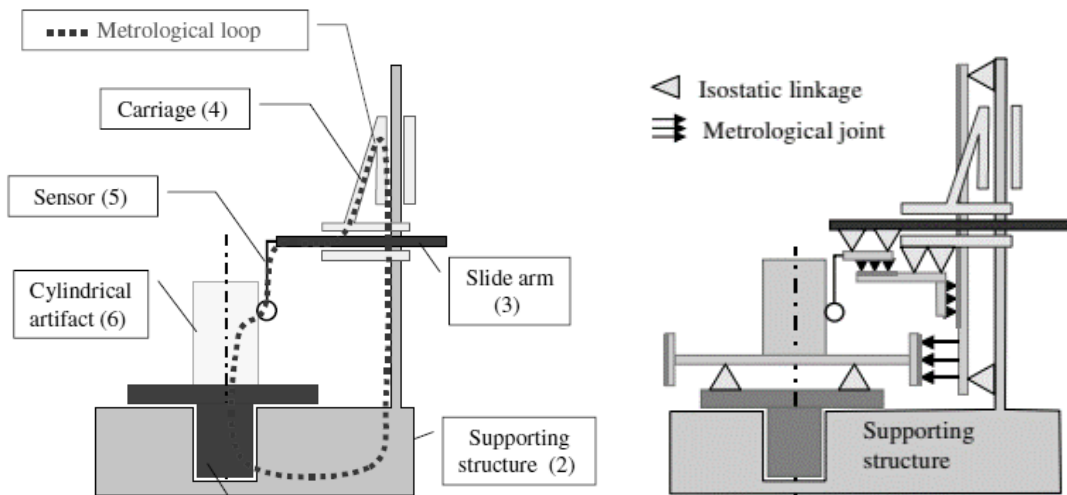
Figure 2-5: The metrology loop and the dissociated metrological structure (DMT) [59].
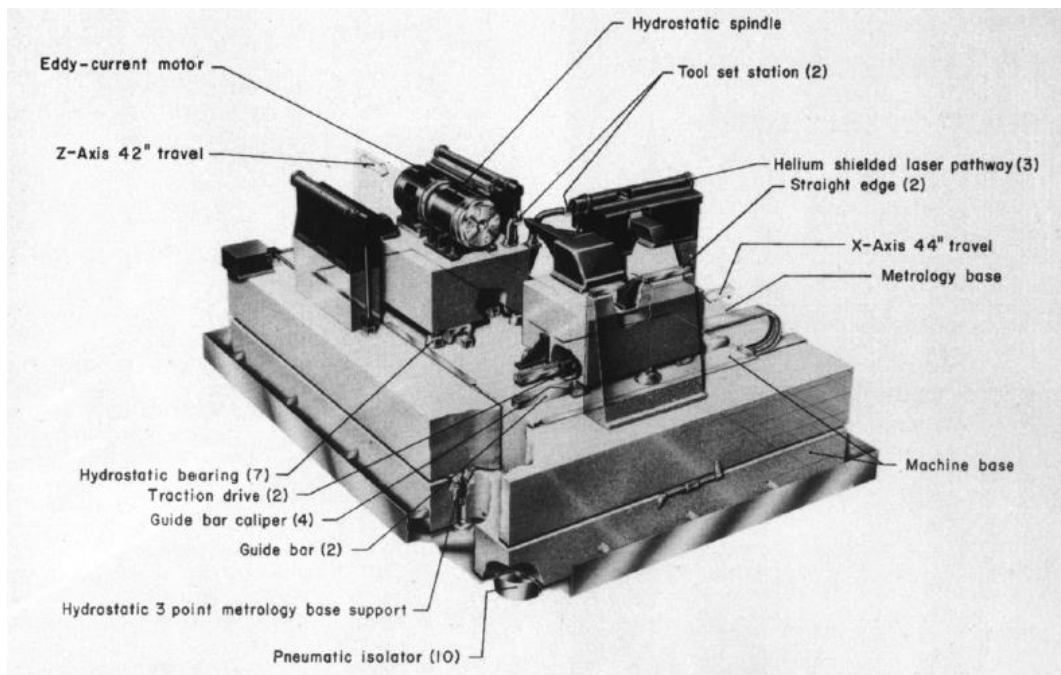
Figure 2-6: The ultra-precision 2,134 m diamond turning machine [60].

The metrology frame and the mirror table of Isara 400 CMM design are dissociated from the structural loop by air bearings. The mirror table is guided by air bearings in a 'floating table configuration which moves only in x and y-direction over a granite base plate. While the metrology frame moves in z-direction, also guided by air bearings against a vertical granite surface. Figure 2-7 presents and an overview of the complete machine and is a 3D metrology frame for the ISARA 400 showing some positioning of the air bearings.
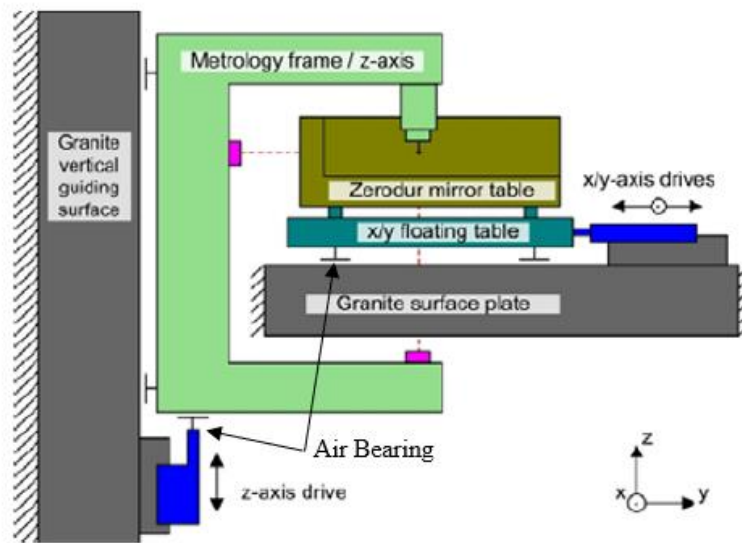
Figure 2-7: The overview of ISARA 400 dissociation arrangement [49].

Considering all the facts, the ultimate reason for the dissociation is to seperate the components with long term stability in-between the calibrations and those components which only have to be stable during a single machine task [48]. Also, to improve the positioning accuracy of the machine [53].

The study acknowledges the importance of dissolution, however, due to cost constrain the metrology frame of the conceptual design discuss in this study is not dissociated from the structural frame. It is highly recommended for future designs to have dissociation fully implemented to improve the performance of the machine.

2.4   Error sources

CMMs are subject to various error sources, emerging from the manufacturing processes, assembly stages and operations conditions. These errors are the results of distortion by force and heat, control system errors and actuators errors, calibration, and even mathematical models [29] [61]. In principle, when measuring equipment such as CMM is working in an ideal situation, it is expected that the probe tip coincides with the workpiece at the specific point. But, due to the errors of the machine, the probe tip coincides with the workpiece at a different point. Therefore, the difference between the two points requires an establishment of error compensation. CMM errors are usually classified into two main streams: static errors and dynamic errors.

2.4.1   Static errors

Static errors are mechanical errors related to the structural frame of the machine and they vary in time [62]. These errors are alleged to be the most contributing sources to the accuracy of the machine [23]. According to Rugbani [29], high static accuracy is a basic requirement for any micro-measuring machine. When considering the mechanical accuracy of CMMs, there are three primary sources of static errors including geometric errors, vibration and mechanical stability errors and thermally induced errors. However, this study will discuss the main contributors and that include the geometric errors and thermal induce errors.

2.4.1.1   Geometric errors

The quality process of the manufacturing process of the components and the adjustment during the assembly of parts induce geometric errors [34] [61] [63]. The error sources can be categorized into two; the first is the position dependent error due to manufacturing and assembly processes. The second one is the position dependent errors which are relevant during the movement of the machine [64].

According to Khan and Chen [65], the experimental evaluation indicates that geometric errors contribute approximately 70% of the total errors of the machine. Therefore, since it accounts for a large proportion of machine tool error, the compensation of the geometric

errors of the machine tool is important to improve the machining accuracy of the machine tool [66].

Generally, and according to Hermann [67], Figure 2-8 is the typical representation of the measuring loop of a coordinate measuring machine. However, depending on the configuration of the machine all measuring motions are performed by the probe or by the table, or divided between the two.
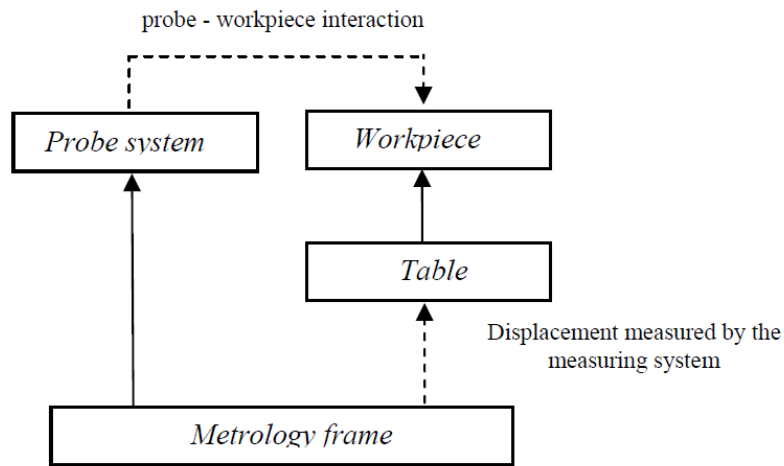
Figure 2-8: Measuring loop of the coordinate measuring machine [67].

The linear guideways of the precision machinery are expected to travel along a straight line and stop at a predefined position. However, in practice the actual path deviates from straight line due to the geometric errors of the guideways and it results also in angular errors.

The geometric errors for linear guideways include straightness and rotation errors, and their relative orientation is subjected to squareness errors. As mentioned by Pan *et al* [18], Xuan *et al* [68] and Liu *et al* [69] the linear guideways consist of 6 DOF, since they are susceptible to moving in any direction. In other words, they may have micro-movements in either direction because of imperfect manufacture. Given the example of the *x*-axis; the three translation errors are described as linear positioning error $\delta_x(x),$ horizontal straightness error $\delta_y(x)$, and vertical straightness error $\delta_z(x)$; the angular errors may

include the roll angular error $\varepsilon_x(x)$, pitch angular error $\varepsilon_y(x)$, and yaw angular error $\varepsilon_z(x)$. Figure 2-9 presents the possible translations and the error locations.
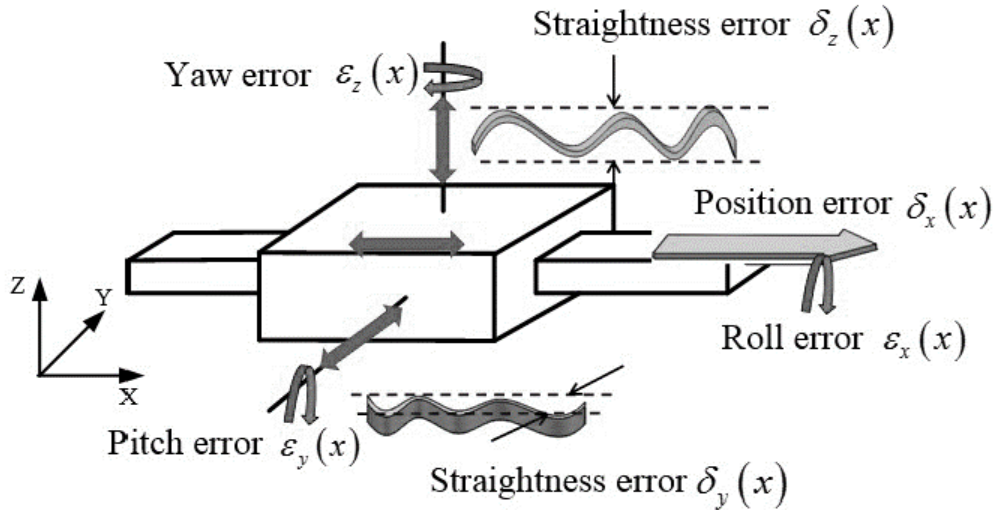
Figure 2-9: A typical example of 6 DOF errors of the x-axis [68].

$$x = \delta_x(x), \delta_y(x), \delta_z(x), \varepsilon_x(x), \varepsilon_y(x), \varepsilon_z(x)$$

$$y = \delta_x(y), \delta_y(y), \delta_z(y), \varepsilon_x(y), \varepsilon_y(y), \varepsilon_z(y)$$

$$z = \delta_x(z), \delta_y(z), \delta_z(z), \varepsilon_x(z), \varepsilon_y(z), \varepsilon_z(z)$$

There are two approaches to enhance accuracy. One is error avoidance, i.e., improving processing techniques, which is effective but costs plenty of resources. The other is error compensation, which is conducted by obtaining the original errors of machine tools by some measuring method [18]. As an economical and efficient method, error compensation has attracted the attention of many researchers.

The procedure to map the geometric errors is almost the same as the one, which is described by Loh *et al* [70], Hermann [67], and Guiqiang *et al* [71]. In reference to Figure

2-9, the geometric error of a moving body is given by the linear error $\delta_j(i)$ and the angular error $\varepsilon_j(i)$, where the subscript j is the error direction, and i inside the parenthesis is the position coordinate, see equation (2) and equation (3). The resultant error motion of a carriage is a combination of rotational and translational errors [72]. With a 4 X 4 homogeneous transformation matrix (HTM), the fundamental operations of translation and rotation can be represented in a single matrix with reference to the origin of the original coordinate frame [73]. The HTMs of rotational $\vec{\varepsilon}(i)$ and translational $\vec{\delta}(i)$ can be given as:

$$\vec{\delta}(i) = \begin{bmatrix} 1 & 0 & 0 & \delta_x(i) \\ 0 & 1 & 0 & \delta_y(i) \\ 0 & 0 & 1 & \delta_z(i) \\ 0 & 0 & 0 & 1 \end{bmatrix} \tag{2}$$

$$\vec{\varepsilon}(i) = \begin{bmatrix} 1 & -\varepsilon_z(i) & \varepsilon_y(i) & 0 \\ \varepsilon_z(i) & 1 & -\varepsilon_x(i) & 0 \\ \varepsilon_y(i) & \varepsilon_x(i) & 1 & 0 \\ 0 & 0 & 0 & 1 \end{bmatrix} \tag{3}$$

The combination of rotational $\vec{\varepsilon}(i)$ and translational $\vec{\delta}(i)$ errors would provide a resultant HTM describing the error, $E(i)$ in position of the nominated axis with respect to its ideal position, see equation (4 - 6).

$$E_j(i) = \vec{\varepsilon}(i) \cdot \vec{\delta}(i) \tag{4}$$

$$E_j(i) = \begin{bmatrix} 1 & -\varepsilon_z(i) & \varepsilon_y(i) & 0 \\ \varepsilon_z(i) & 1 & -\varepsilon_x(i) & 0 \\ \varepsilon_y(i) & \varepsilon_x(i) & 1 & 0 \\ 0 & 0 & 0 & 1 \end{bmatrix} \cdot \begin{bmatrix} 1 & 0 & 0 & \delta_x(i) \\ 0 & 1 & 0 & \delta_y(i) \\ 0 & 0 & 1 & \delta_z(i) \\ 0 & 0 & 0 & 1 \end{bmatrix} \tag{5}$$

$$E_j(i) = \begin{bmatrix} 1 & -\varepsilon_z(i) & \varepsilon_y(i) & \delta_x(i) \\ \varepsilon_z(i) & 1 & -\varepsilon_x(i) & \delta_y(i) \\ \varepsilon_y(i) & \varepsilon_x(i) & 1 & \delta_z(i) \\ 0 & 0 & 0 & 1 \end{bmatrix} \tag{6}$$

The transformation matrix error of the probe in reference to the global coordinate frame is given by equation (7).

$$E_j(p) = E_j(x) \cdot E_j(y) \cdot E_j(z) \tag{7}$$

Where, $E_j(p)$ is the transformation matrix error of the probe, $E_j(x)$, $E_j(y)$, and $E_j(z)$, are the transformation matrices of x, y, and z axis.

However, for this study the mirror out-of-squareness is evaluated as the primary error function of the machine. Where the geometric error is recommended when analysing the errors influencing the mirror out-of-squareness, hence not included in this study.

2.4.1.2 Thermal Induced Errors

When improving the positioning accuracy and machine performance the thermal-induced errors consideration becomes significant [52]. According to Chen *et al* [74], Dos Santos *et al* [75] and Weng *et al* [76] the thermal-induced displacement variations of machine tools are a vital problem that may be responsible for 40% - 70% of the geometric inaccuracy of the machine tool. This is the results of temperature changes in the machine structure, influenced by the heat generated by the machine, environmental temperature changes, and radiant external heat sources [77].

The induced thermal errors can be classified in two main categories; the first category is a uniform difference between the temperature of the measuring standard and the workpiece. The CMM is calibrated under specific temperature conditions, and any deviation from these conditions can lead to dimensional inaccuracies. The second category refers to the temperature gradients introduced in the machine's components due

to uneven heating and cooling of the machine elements that causes components to expand or contract unevenly, introducing measurement errors. They depend on the machine structure, the properties of the material being used to manufacture the machine, the generated temperature distribution, and the induced environmental temperature [34].

As mentioned by Yang *et al* [78] thermal-induced problems are more complicated to model than geometric problems since the temperature field varies according to the operation at hand and the environmental conditions. According to Chen *et al* [79], effective thermal error compensation relies on the accurate prediction of the time-variant thermal errors during machining.

To achieve high accuracy of machine tools, it is important to find effective methods for reducing thermal errors [74] [80]. Several techniques have been developed and implemented with the compensation schemes of thermal errors in machine tools [81]. Yang *et al* [82] performed a thermal-induced error prediction and the compensation on the spindle system of a box-type precision CNC coordinate boring machine. The thermal error modelling and compensation equations were proposed. Then thermal balance experiments were performed by using the five-point method. The time series models were established for spindle axial thermal elongation and radial thermal yaw and pitch errors based on the experiments. After that, thermal drifts were translated into coordinate offsets and established the final compensation mathematical equations in three directions. Finally, the error compensation was carried out. The results show that the machine precision can be improved efficiently.

Chen *et al* [74] focused on developing a compensation module for reducing the thermal error model analysis and robust modelling to control the thermally induced positioning error of a CNC milling machine. To create the thermal model, the locations of four thermal sensors were appropriately selected to establish the thermal displacement prediction model based on the initial measurements with the use of four sensors. Following that the proposed compensation system was developed and implemented in a three-axis milling machine. The feasibility of the compensation system was validated through the application of milling operation. The results show that the displacement variations on the x and y-axes and the position error at the tool centre were controlled

within 20 µm when the compensation system was activated. The feasibility of the compensation system was successfully demonstrated in application on the milling operation.

Do Santos *et al* [75] established a methodology to verify the use of physical models to simulate the generation of heat by friction through the finite element method is robust and accurate when compared with the results obtained experimentally. It was possible to validate the finite element model of the entire machine for several different duty cycles. The results of the simulations showed that the methodology is an effective tool to determine and predict the thermal displacement of the machine by correlating the reading of temperatures at strategic points with the displacement at the tooltip, hence reducing the effort and analysis time to solve thermal problems in machine tools.

Weng *et al* [76] applying the theory of heat transfer, finite element method and multi-body thermal error modelling method, presented a temperature structure multi-step calculation method to evaluate the influences of external heat source on volumetric thermal deviations of a machine tool. A series of simulations and validating experiments were carried out to verify the effects of different external heat sources on the machine tool. In this study by Putz *et al* [80] a methodology is presented to experimentally determine thermal machining errors of the machine tool, and workpiece in the total thermal error during a machining process. The workpiece was subsequently measured, and both the machine's internal and additional built-in measuring sensors were used to quantify displacement errors.

The other method is the data-driven model, generally the thermal model can be practically established based on the collected parameters of the system by means of the different methods, including the statistics model, exponential function, multiple regression, non-linear multiple regression, neural networks, expert system, and fuzzy theory. In this study, the multiple linear regression analysis is employed to describe the correlation between axial deformation of the metrology loop and temperatures.

2.4.1.3 Thermal behaviour

According to Ruijl [53], generally the thermal error compensation models applied in machine tools and CMMs are based on simple linear expansion and bending of the metrology loop. The temperature of the loop components is measured with the workpiece. Theoretically heat is transmitted from one point to another in a structure through, heat conduction, heat convection, and heat radiation. Conduction is the transfer from higher to lower temperatures mainly by means of a solid medium and can be expressed in equation (8).

$$Q_{conduction} = kA\frac{dX}{dT}$$

(8)

where Q is heat conduction, k is the conduction factor of the medium, A is the area of contact surface, dX is the distance between the ends, and dT is the temperature difference between the ends. The heat convection is delivered naturally from one side to another by affecting the volume and density of the media, which can be described by the following equation (9).

$$Q_{convection} = hA\Delta T$$

(9)

where Q is heat convection, h is convection factor, A is sectional area, and ΔT is temperature difference between the ends. Lastly, heat radiation is delivered through electromagnetic wave, independent on any media, which can be described by the following equation (10).

$$Q_{irradiation} = \sigma A(T_1^4 - T_2^4)$$

(10)

Where σ represents the Stefan-Boltzmann constant, A is the radiating surface area, and T_1 and T_2 are the temperatures at two radiating surfaces. Figure 2-10 is a typical example of the thermal effects on a machine.
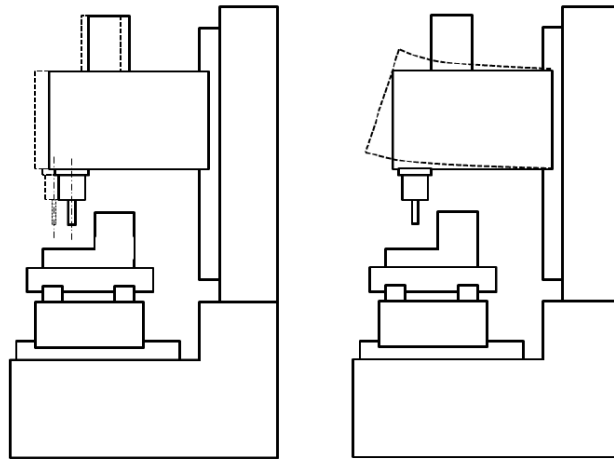
Figure 2-10: Possible effects of thermal-induced errors of the machine tool [74].

The thermal behavior of a CMM depends on its geometry and the materials used. A homogeneous temperature difference ΔT, causes a machine component to expand, according to equation (11).

$$\Delta l = \alpha \times l \times \Delta T = Q \ \times \frac{l}{A} \times \frac{\alpha}{\lambda} \tag{11}$$

This expression describes the sensitivity for temperature variations of a machine component. It depends on the heat flow Q, the geometry in terms of l/A, where A is the cross section for conduction and on the quotient of the material properties λ.

2.4.2 Dynamic errors

The accuracy of the CMM machine especially during the operation is influenced by the dynamic errors [83] [84]. These errors occur during the operation of the machine with the main variables being the speed of the machine, the acceleration, and the applied forces [29] [83] [84]. They are caused by the dynamic deformation and displacement of low-stiffness parts of the machine such as bearings, linear guideways, and joints which can lead to friction, wear, and backlash occurrence [85]. The structure and the material

properties of the machine contribute significantly towards the improvement of these types of errors [84]. They tend to have a strong impact on high-speed machines [23].

The increasing demands on accuracy and increasing manufacturing variety raise the demand for fast automated inspection of manufactured parts [86]. Due to the demand for shorter cycle times of measurement tasks, CMMs are increasingly required to be used at high measuring velocity, and in such conditions, dynamic errors will certainly influence the measurement accuracy and constitute a barrier to the reduction of measuring cycle time [87]. The accuracy of these fast measurements is limited by the positioning accuracy of the measuring machine. Manufacturing accuracy and limited stiffness of bearings and guideways constitute limitations for the machine's positioning accuracy [86] [88].

According to Weekers [61] when the elastic system is loaded statically, the system should be kept in an equilibrium state, to prevent the imbalance of the internal forces and moments in the deformed configuration with the external forces; and can cause vibrations. The natural vibration with the lowest frequency plays the most important role since it is the upper limit for the dynamics of a machine tool.

There have been various techniques to reduce the effects of dynamic errors in the coordinate machines. According to Weeker [61] and Chensong [84], the first condition to resolve dynamic errors is to reduce the number of degrees of freedom between the carriage and the driving mechanism. This can be achieved by improving the design of the kinematic drives by minimizing unnecessary or excessive movements [84]. The second option is error compensation which is said to be much more complicated than static error compensation. According to Jiang *et al* [89], the accuracy of dynamic measurement error prediction has a significant influence on the precision and stability of the sensors. However, Yuan *et al* [90] mentioned that dynamic error compensation techniques of CMM are still under study, the major problem is a lack of suitable models, which would be able to correctly and simplify the related dynamic errors with the structural and operational parameters.

Yuan *et al* [90] proposed an error model of dynamic Abbe errors according to the relationship to Abbe offsets and movement directions. A model parameter measurement method is given based on measurements of internal and external dimensions.

Experimental results demonstrate the effectiveness of the model. A dynamic Abbe error compensation method that is easy to use is proposed for CMM end-users referred to as probe tip radius correction. Echerfaoui *et al* [87] presented an experimental investigation of dynamic errors in CMMs. A structured experimental design and improved statistical analysis tools are combined to evaluate the measurement parameter's effects at high measuring velocities. Carried out on a bridge-type CMM, these parameters were combined and used to investigate the variation of several dynamic error attributes. A laser interferometer system was used to assess error components under different dynamic conditions. Based on these results, the contributions of each parameter in the variation of the dynamic error attributes are estimated revealing many options to consider for building an efficient prediction model for error compensation. A neural network-based prediction model suggests a promising performance. Echerfaoui *et al* [87] propose an active control system including a model-based compensation system for dynamic errors to increase acceleration and velocity. A novel optical sensor permitting the direct measurement of the actual tool-centre-point position was used for system identification of the required dynamic model. The position of a LED point source was detected with high subpixel precision by replicating the spot several times on the camera chip and averaging over the centre of gravities of all spots. A model for the largest dynamic error component of a small multi-axis measuring machine was derived and the sensor was used to identify the model parameters. A model-based feedforward and feedback control system that reduced the dynamic tracking error was designed. This control system allows machine motions with both high accuracy and large velocity. The achieved performance was evaluated using tool-centre-point tracking error measurements obtained with the novel optical sensor.

There has been various evaluation of identifying a suitable dynamic error model for the CMM machines. However, for the purpose of this novel design a follow up study is recommended to evaluate the effects of dynamic errors. Also, to study the best suitable model for the dynamic errors.

2.5 Calibration

Karun [91] mentioned that since the introduction of the first CMMs, there has been a consistent desire to evaluate the performance of the machine. The demand for high product quality has become necessary and thus the improvement and the measurement accuracy and calibration of the CMMs have become an important area of investigation [91]. According to Ruijl [53], to achieve a sufficient uncertainty, especially in the sub-micron range, the machine needs to be calibrated and compensated.

CMMs are susceptible to errors which degrade the accuracy over time, and hence the calibration must be done consistently [91]. The need for calibration is justified by the mechanical imperfections of the guideways, which cause kinematic errors in the motion of a slider, offset with the result that the position of the stylus tip of the probe is spatially shifted from the nominal position [92].

Various techniques can be used to perform the calibration of the CMM machines. These techniques include the inspection and calibration using various artefacts such as Ball Plate, Ball Bar, Gauge Block and Square Master [91]. There are other methods for large-size CMMs such as laser interferometer, and coordinate comparison between two CMMs. According to Dai [93] calibration artefacts are a conventional method of calibration that has been used successfully for acceptance tests, calibration, and the verification of micro-CMMs.

Other calibration methods include the parametric method, which employs matrices to transform an array of 6-DoF errors at the point of measurement to those at the point of interest [94]. The parametric method includes an integrated geometric model and the product of the exponential model [95]. The second method is the use of standard specimens. The third one is the self-calibration method, which is also known as the reversal method. According to Kim *et al* [94], there have been several applications of the reversal methods for the calibration of orthogonality. Estler [96] defines slide straightness error/out-of-squareness as an error observed by the indicator when it is either stationary and reading against a perfect straightedge supported on a moving slide or moved by the slide along a perfect straightedge which is stationary. Several techniques have been

developed for the measurement of straightness errors including gauging against a taut wire, laser straightness interferometers, alignment telescopes, fluid reference surfaces, and, of course, mechanical straightedges [96].

Other calibration method includes the new design by Chanthawong *et al* [97] where CMM performance verification by using temporal coherence of optical frequency comb is studied. The mode-locked fibre laser was stabilized to the Rb clock (frequency standard). The system with a combination of fibre and mirror was developed to increase the repetition-frequency of a mode-locked fibre laser by selecting every 50th mode of the optical frequency comb. The 2-hour stability shows that the modified optical comb is good enough as a standard for a CMM. The absolute length is determined from half pulse interval distance of the modified pulse laser and the performance of CMM were determined from interference fringes. The measurement system is based on a fibre-type interferometer; it offers a more convenient system for CMM performance verification.

However, this study considers the use of standard specimens such as the block gauges. Also, the mirror calibration is performed using the prediction techniques of the special triangle.

2.6   Measurement uncertainties

The manufactured parts are susceptible to geometrical errors; thus, they have to be assessed against dimensional tolerances to prove their conformance with specifications [98]. This is because according to the Guide to the Expression of Uncertainty in Measurement (GUM) [99] when presenting the results of a physical measurement, it is required to include the expression of conformance or uncertainty of the results as an indicator of the quality of the result obtained to prove the reliability. If the uncertainty is not presented the measurement cannot be conclusive. Therefore, measurement uncertainty is a crucial parameter for making the right decisions, and not considering this parameter can, therefore, sometimes lead to inappropriate decisions [100].

Determining the uncertainty associated with the specific measurements or coordinates obtained from the CMM when measuring a particular object or workpiece a complex task,

given the diversity of influences [100]. Measurement uncertainty analysis takes into account not only the inherent uncertainties of the CMM but also external influences that may affect the accuracy of the measured coordinates. Several factors need to be considered when verifying the uncertainty in the measurement. According to Cheng *et al* [21] and Heibelmann *et al* [101], these factors include the machine effects such as guideways, and the probe assembly, and the properties of the workpiece such as surface roughness and the form deviation. Other contributing factors include the operator, environment, and the method of measurement.

Different authors have proposed various methods of uncertainty measurement. Welhem *et al* [102] presented a technique developed to model and estimate task-specific uncertainty for coordinate measuring machines using contacting probes. Heibelmann *et al* [101] reported on the advancements of Virtual Coordinate Measuring Machines (VCMM) to suit present-day needs in industrial applications. The VCMM utilizes numerical simulations to determine the task-specific measurement uncertainty by incorporating broad knowledge about the contributions of contributing factors, including those that are not machine specific. According to Štrbac *et al*, [103] Monte Carlo simulation is believed to be the best method for numerical evaluation of measurement uncertainty. Štrbac developed a model for the evaluation of uncertainty in measuring flatness, based on the repeatability of the sampled coordinate of a point. The proposed model was verified on the standard for flatness - optical glass. This method was employed by Ceja [104] to evaluate the influence of the PDFs of input quantities on the output quantities of a measurement model when the measurements obtained with an optical measuring machine are presented.

GUM Supplement 1 [105] [106] explains that the propagation of distributions includes the complication of the probability distributions of the input quantities, which can be accomplished in three ways: a) analytical integration, b) numerical integration or c) numerical simulation using Monte Carlo methods. The GUM Supplement 1 provides basic guidelines for using the Monte Carlo simulation for the propagation of distributions in metrology. It is presented as a fast and robust alternative method for cases where the GUM approach fails. This method provides reliable results for a wider range of measurement models as compared to the GUM approach.

2.7   Kinematic modelling

Kinematic modelling is the science of motion that does not study mass and moments of inertia. It is concerned with the geometrical and time-based properties of motion [107]. In robotics, kinematic modelling is employed to establish the relationship between the coordinates of the end effector and the joints of the manipulator [108]. A thorough computation of the kinematics modelling is required to determine the position and the angle of the end effector at every instance of the motion [109]. It is the initial principle when developing the study and the design of the robotic manipulator. Two methods can be employed depending on the situation at hand: forward kinematics and inverse kinematics problems [108] [109]. Forward kinematics is a method employed to ascertain the position of the end effector given the parameters of the joints of the manipulator [109]. Figure 2-11 is a typical example of forward kinematics. Solving forward kinematics problems is straight forward and there is no complexity in deriving the equation. This kinematics applies to manipulators with members attached in series with revolute or prismatic joints [26].

Figure 2-12 is a given example of inverse kinematics, unlike forward kinematics it requires the position and the angle of the end effector to determine the parameters for the joint(s) of the manipulator [109]. According to Barika and Berka [110], the joint angles are derived from changes in the position of the en   Qd effector. The solution to the inverse kinematics problem is generally complex to resolve [27]. The technique refers to the process of obtaining joint angles and other variables from the known position of the end effector [27].
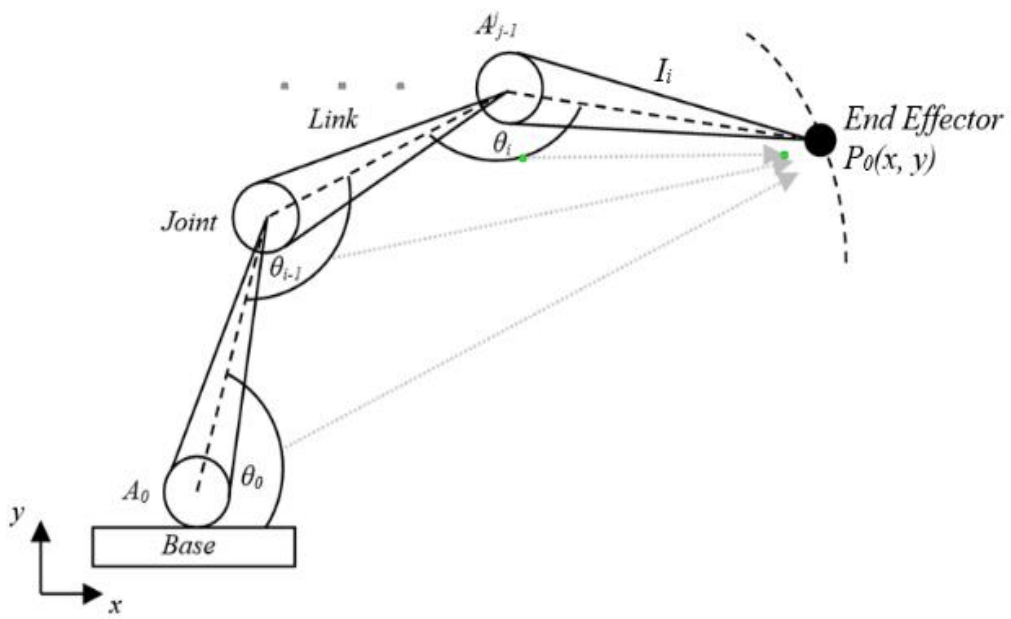
Figure 2-11: The principle of forward kinematics [110].
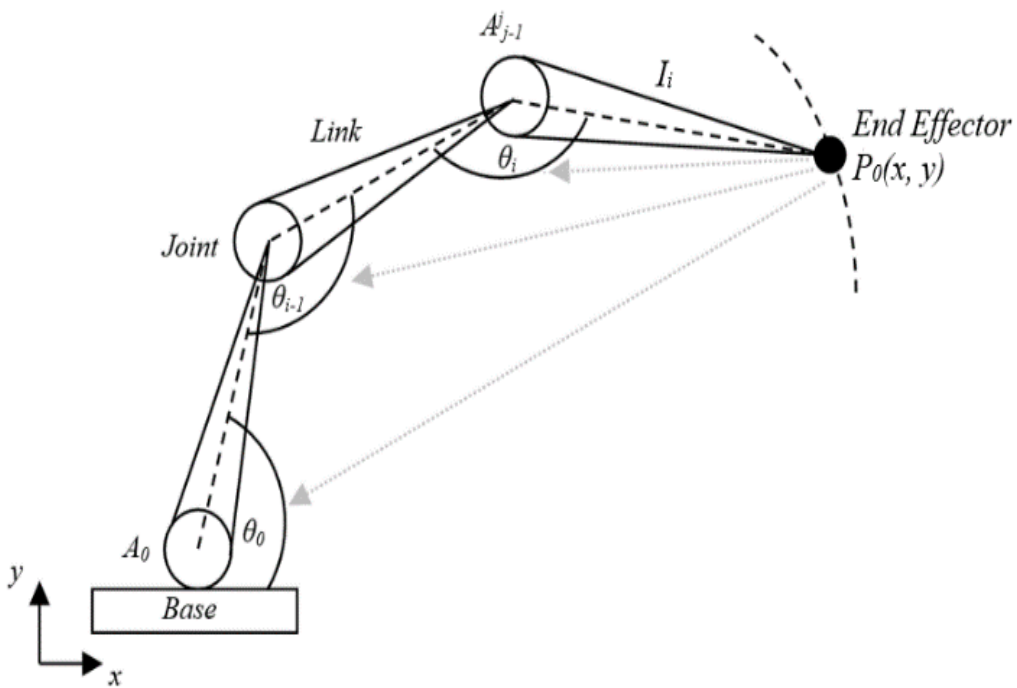
Figure 2-12: The principle of inverse kinematics [110].

Where, A_0 and A^j_{j-1} present the joints of the manipulator, θ_0, θ_{i-1}, and θ_{0i} are the angle for the links. I_i presents the link/ members of the manipulator. P_0 is the coordinates of the end effector.

According to Kucuk and Bingul [17], robot manipulators are constructed with rigid members that are connected with various joints depending on the design of the machine to allow desired motion [16] [107]. The degrees of freedom (DoF) of the joints vary from one or more depending on the type of joint required for the design. Some situations requires motor to be attached to the joints for the overall motion of the mechanism and to control and perform a given task [16]. According to Kwawasaki [107], a joint that is moved by the activation of the motor attached is an active joint, and a non-actuated joint is called a passive joint. The joints of the manipulator are said to be the most important part of the mechanism that needs to be considered during the kinematic modelling.
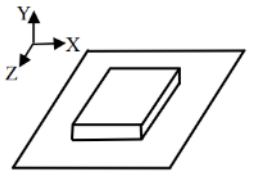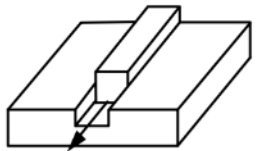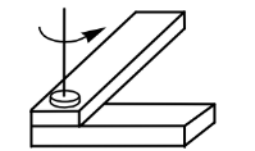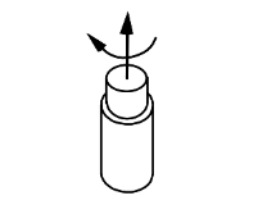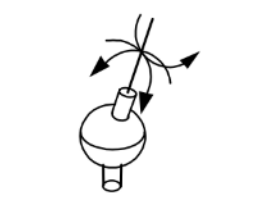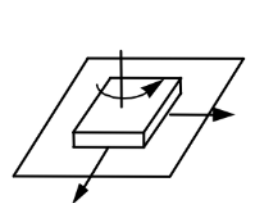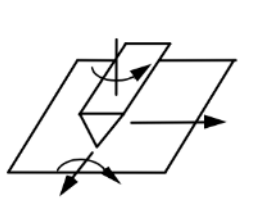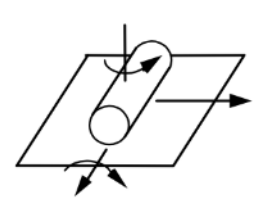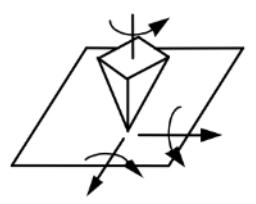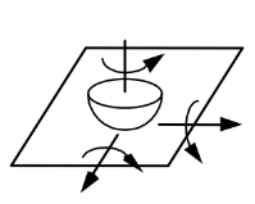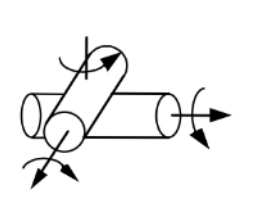
Figure 2-13: Kinematic joint types with several DoF indicated [111].

This study employs forward kinematics to derive the solution to the position kinematic model of the measuring probe in the global coordinate system. The study finds the

independent solution for each axis in the coordinate system. The joints applied to the novel design include the prismatic joints, for the manipulation of the *x, y,* and *z*-axis. Both the position and the distance measuring equations of the probe are derived.

Chapter 3:

Design of the Novel CMM

3. Design of the novel CMM

3.1 Introduction

This chapter discusses the design and construction of the novel CMM with a single distance measuring sensor including the machine structure, the metrology system, and the manipulation system. Further discussion will be provided on the frame suspension, displacement sensor, mirror table and mirror. Finally, the major advantages and disadvantages will be discussed.

3.2 Novel CMM design description

The proposed design presented in this study suggests a possible modification to the Ultra-Precision CMM metrology system by Ruijl [53]. The modification comprises the removal of two displacement sensors and the repositioning of the remaining sensor and mirror without impacting the Abbe principle, see Figure 3-1.

(a)   (b)
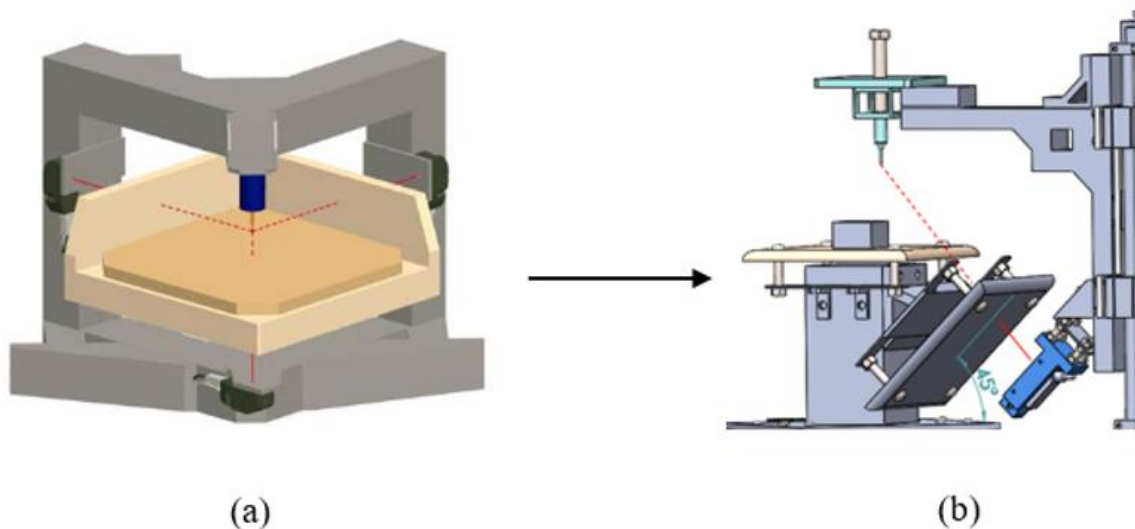
Figure 3-1: The modification of the metrology systems, (a) is the existing ISARA 400 metrology system, and (b) is the proposed metrology system discussed in this study.

Figure 3-2 is the schematic of the proposed novel CMM with overall volume of 900 x 550 x 160 mm^3 (see machine drawings in Appendix A). The machine structure is established as the backbone of the machine; hence it integrates the metrology frame and the manipulation system. The structure is predominantly manufactured from extruded aluminium to increase and maintain its robust structure, and to minimize unintended movement between machine components. This rigid structure is necessary to reduce the weight of moving parts and dynamic errors. The metrology system and manipulation system are the main subsystems of the machine.
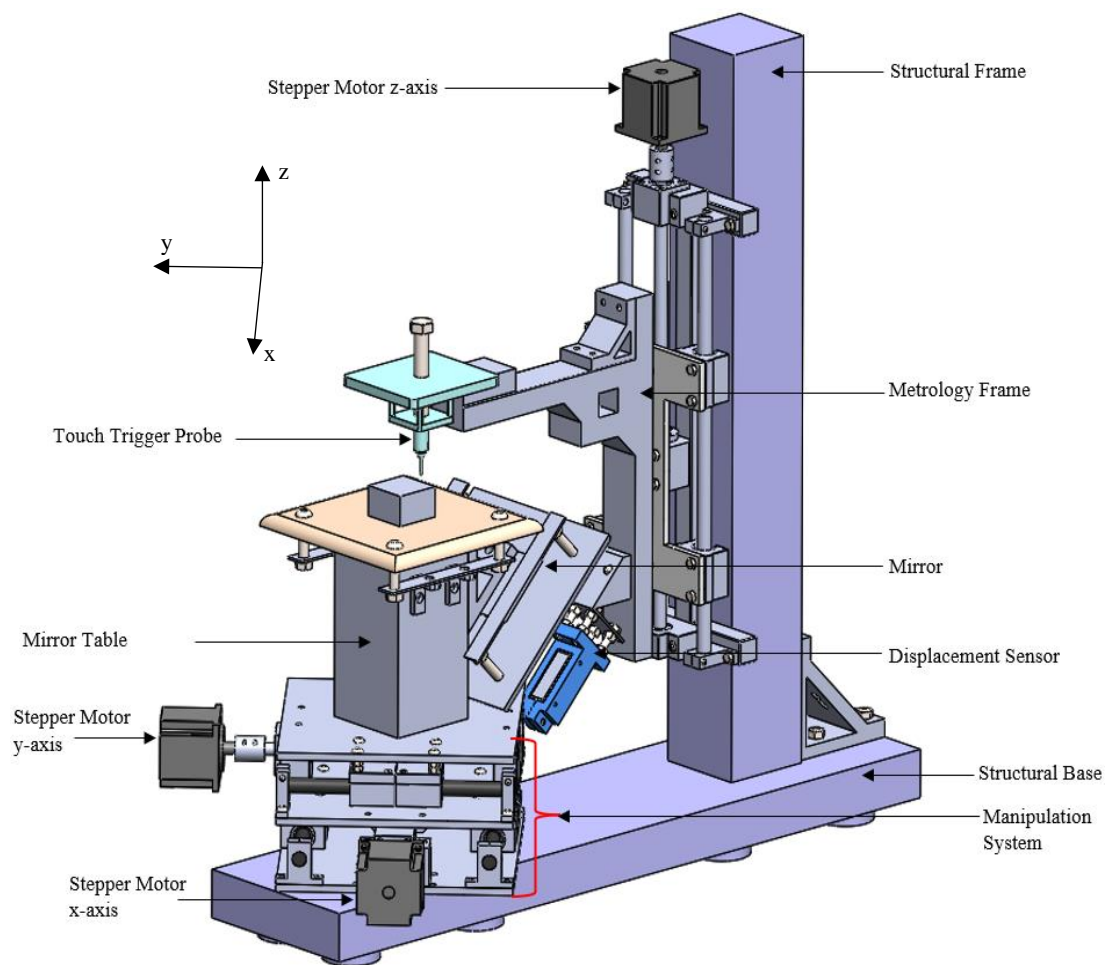
Figure 3-2: Novel CMM design.
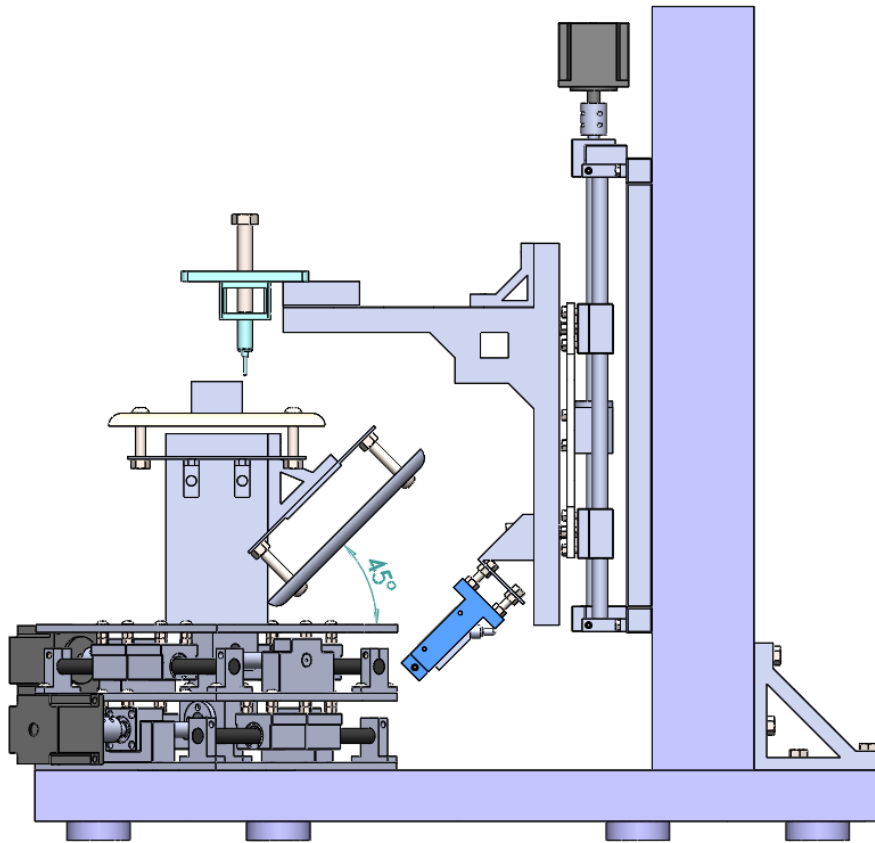
Figure 3-3: Novel CMM side view.
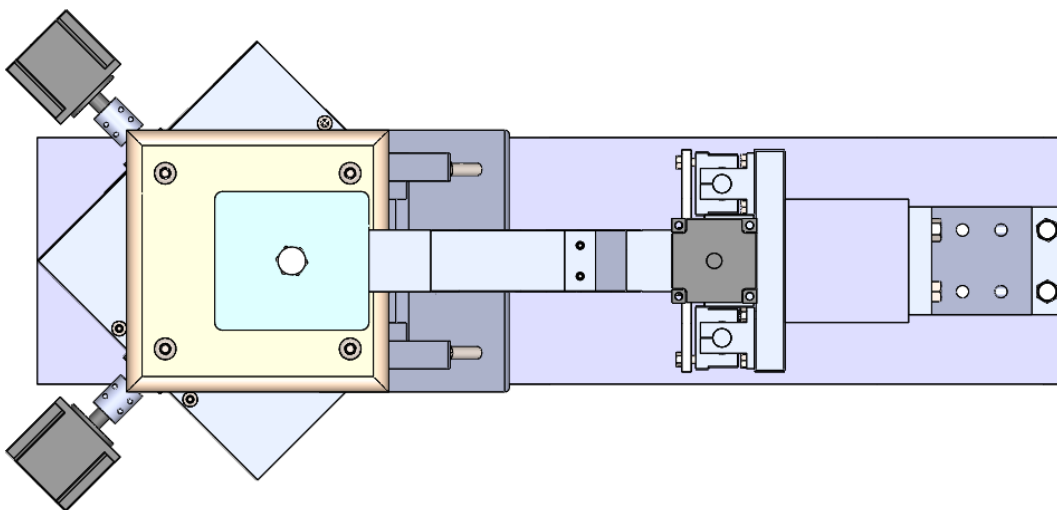
Figure 3-4: Novel CMM top view.

3.3   Metrology system

Figure 3-5 presents the schematics of the metrology system as the combination of the mirror table and the metrology frame. The design suggests a workpiece is supported by the mirror table and is translated to the x and y-axis by the manipulation system. The mirror is positioned at 45$^\text{o}$ to the vertical axis of the mirror table, and to each plane surface of the coordinate system. The metrology frame is a cantilever with a vertical member and a horizontal member. The displacement sensor is mounted at 45$^\text{o}$ at the lower end of the vertical member of the metrology frame while the probe is fixed at the cantilever end of the horizontal end. The functional line of the displacement sensor is always fixed to the tip of the probe. This configuration suggests Abbe's fundamental requirements in all translations of the machine in a global coordinate system. The mirror is perpendicular and always intersects the laser beam at a gap distance between the displacement sensor and the probe. The distance between the displacement sensor and the mirror changes with the change in the actuation of the joints.
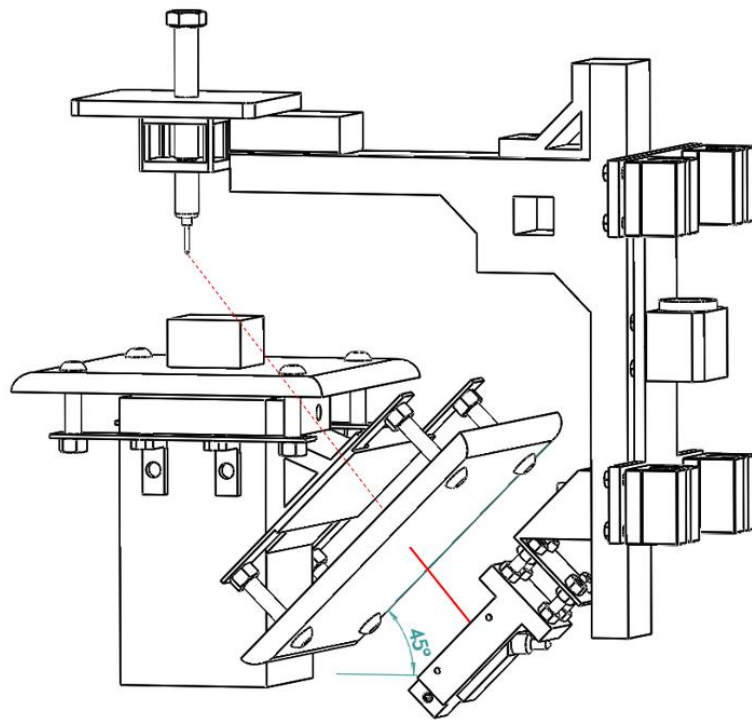
Figure 3-5: Metrology system.

The measurements in x, y, and z directions of the proposed design are obtained by the computation of the functional line components presented by a_x, a_y, and a_z, (see Figure 3-6). The formulation of the components is presented by the kinematic model in chapter 4. Any perpendicularly deviation of the function line and the mirror and the misalignment of the probe will affect the measurement of the components.
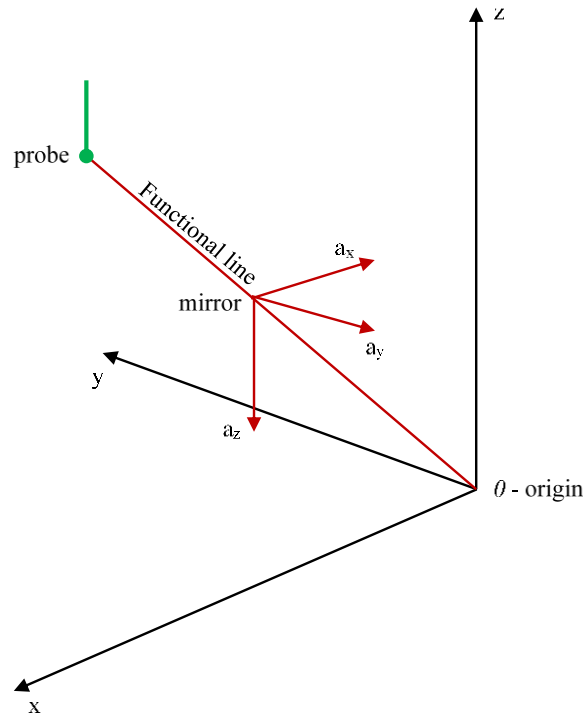
Figure 3-6: 3-D Measurements with a single sensor.

3.3.1 Metrology frame

The metrology frame is kinematically mounted with a prismatic joint to the structural frame to translate the probe and the displacement sensor in vertical axis (z-axis). Due to cost constraints the frame is manufactured from a standard t-slot aluminum extrusion. However, this study recommends a metrology frame and mirror table manufactured from Zerodur (α < 0.01 to 0.05·10-6 1/K, λ = 1.64 W/m·K, ρ = 2500 kg/m^3, cp = 820 J/kg·K) and Super Invar (α < 0.8·10-6 1/K, λ = 11 W/m·K, ρ = 8000 kg/m^3, cp = 515 J/kg·K) materials. These are proposed by Ruij [53] to reduce the thermal expansion to several nanometer and thus the compensation is redundant. The frame is designed to maintain the

mutual position and alignment of the probe and the displacement sensor with high stability. Hence it is designed to be very stiff, to prevent deformations due to acceleration forces. Since Abbe's principle is theoretically fulfilled, the metrology frame will only transform the translational position information along the coordinate axes.
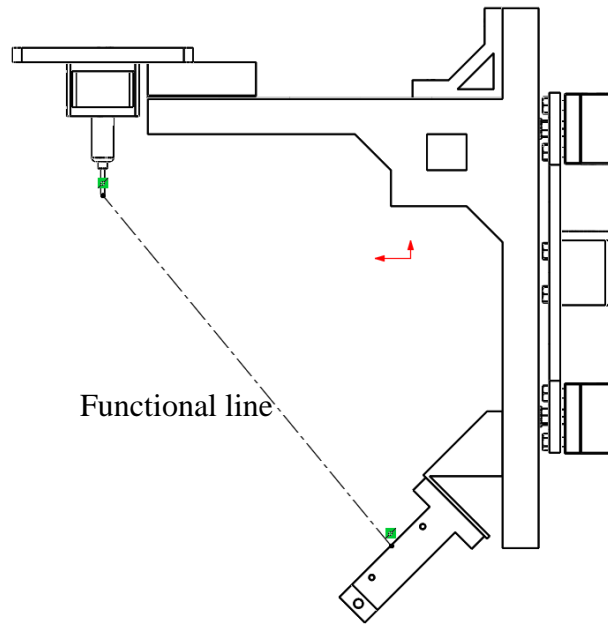
Figure 3-7: A typical metrology frame.

An ideal alignment of the functional line to the probe is theoretically assumed to be collinear with the ruby centre of the probe. However, due to machine assembling error processes misalignment is acknowledged, hence the development of a model to determine the deviation to is proposed, even though it will be difficult to set up and verify the alignment. Figure 3-8 presents the ruby of the probe with the functional line interception point p at the surface of the sphere and further continues as radius r to the centre of the ruby 0. This situation assumes θ as the measurement of latitude and φ as the measurement of longitude at 45$^\text{o}$ respectively. The misalignment of the functional line to the centre of the probe is evident when the surface coordinate system directions. The distance between the two points will be the error. Since it will be difficult to set up and verify This study considers this error as an area for investigated, however, it will not be discussed in this study.
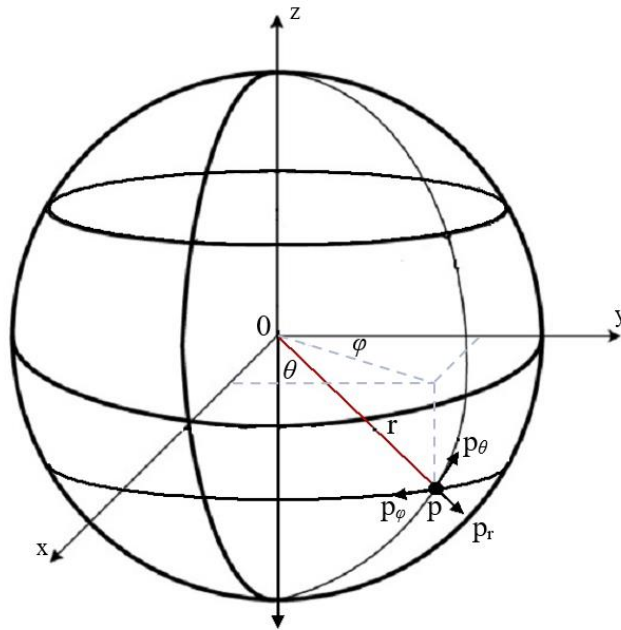
Figure 3-8: The coordinates of the functional line on the ruby of the probe.

The linear slide for the metrology frame and the manipulation systems is an assemble unit of linear bearings with aluminum housing sliding on 12 mm chrome rods. The National Electrical Manufacturers Association (NEMA) 23 stepper motors coupled to the lead screw with ball screw to provide actuation with specific positioning. Figure 3-9 present the parts used to assemble the linear guideway. See the technical information about these parts in Appendix B.
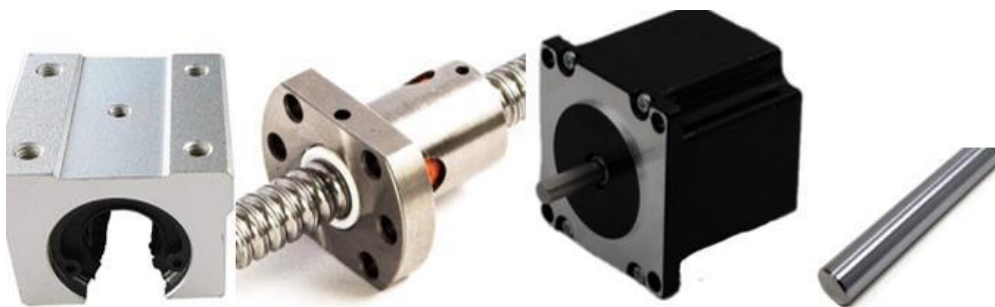
Figure 3-9: Equipment used to assemble the linear slides include (a) Linear bearings, (b) Ball screw, (c) Stepper motor, and (d) Linear chromed steel rod.

Due to budget limitations, ILD1320-100 from Micro-Epsilon (ME) displacement sensor with a repeatability of 10 μm was employed. The operation of the sensor is based on the principle of optical triangulation, that is, a visible, modulated point of light is projected onto the target surface. The diffuse part of the reflection of this point of light is displayed depending on distance on a position-resolving element by a receiver optic which is arranged to the optical axis of the laser beam in a defined angle. A signal processor in the sensor calculates the distance of the point of light on the measuring object to the sensor by means of the output signal of the elements. The distance value is linearized and output by means of the analog or RS422 interface. The technical data, connection possibilities, pin assignment, and the indicator elements at the sensor are given in Appendix C. The ILD1320 DAQ tool V3.5.7 was used to read the distance between the displacement sensor and the mirror. Figure 3-12 is the typical display of the DAQ.
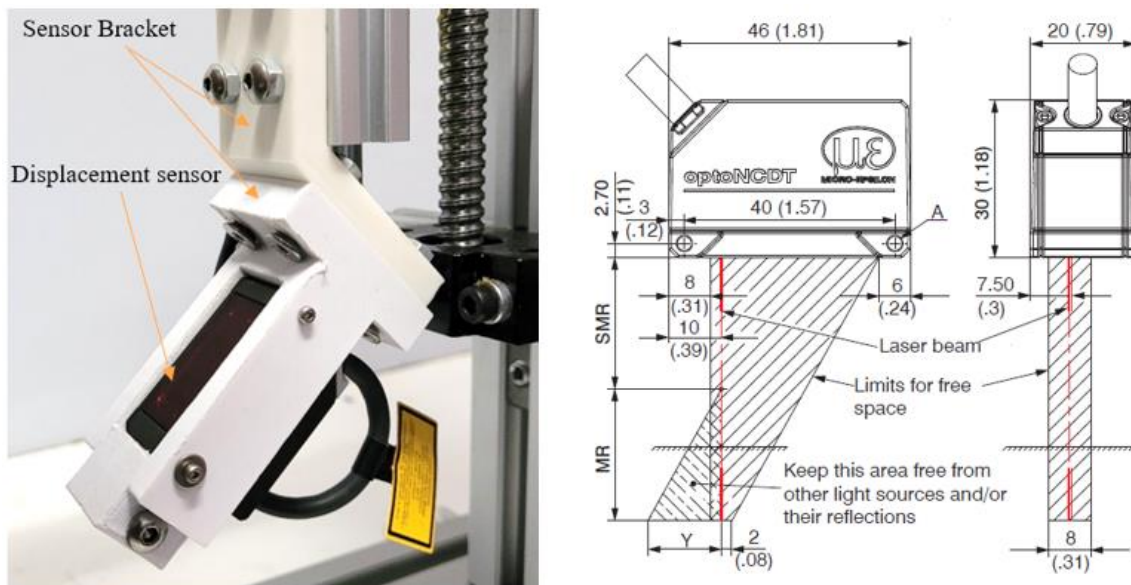
Figure 3-10: ILD1320-100 displacement sensor from Micro-Epsilon.

The displacement sensor is mounted on a specially designed bracket, see Figure 3-11. It is designed taking into consideration the alignment requirements of the laser beam, misalignment may occur due to the errors during the manufacturing and assembly of the parts. The bracket is mounted on the metrology frame with fine threaded bolts carrying

each part to help in minimizing the misalignment of pitch, roll and yaw angles of the measuring axes.
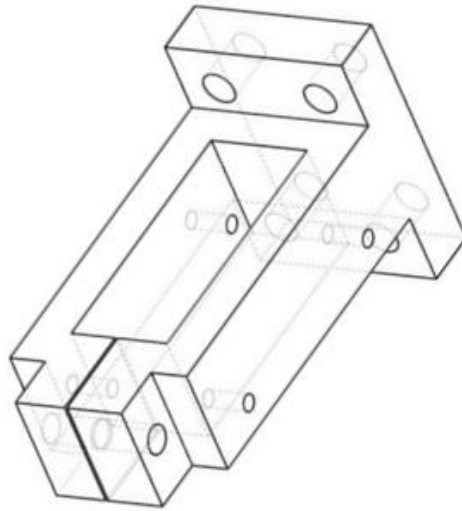
Figure 3-11: Displacement sensor mounting bracket.
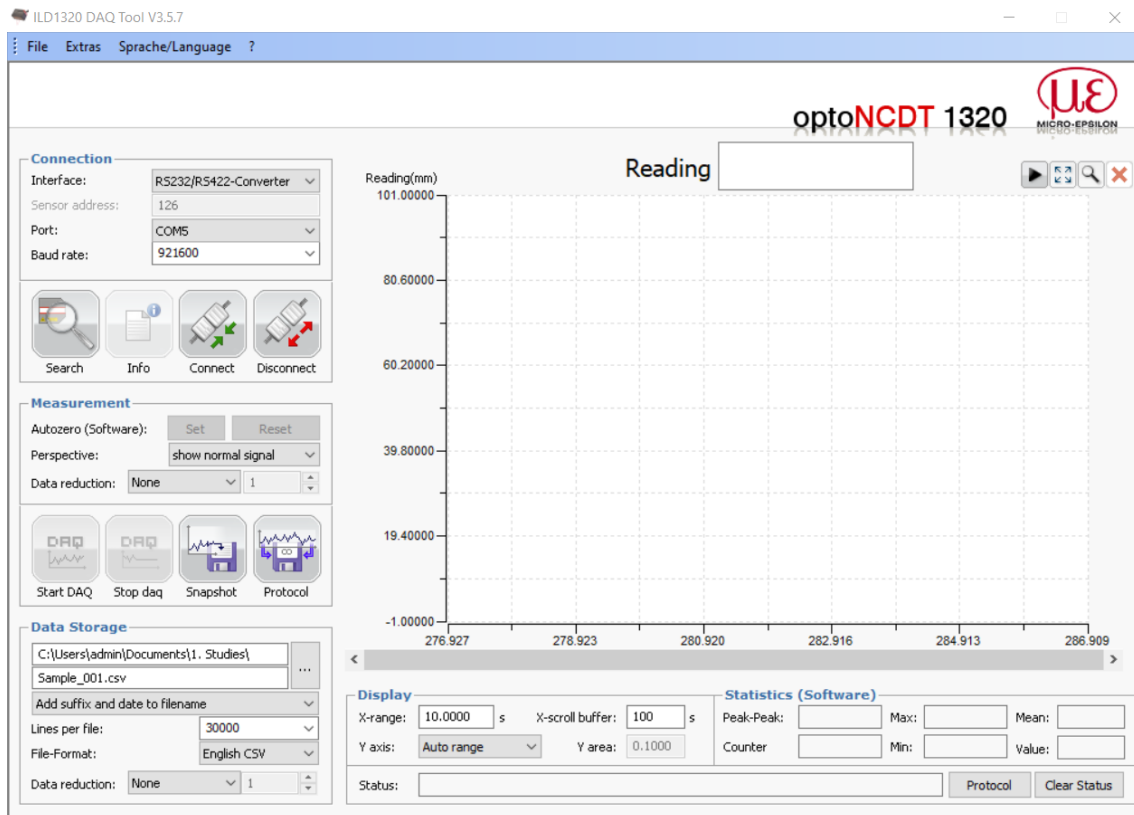
Figure 3-12: Displacement sensor results display.

A Renishaw TP20 manual indexable probe was used (see Appendix D: Technical details of Renishaw TP20 probe). The TP20 probe provides unidirectional repeatability of ±0.35 μm. The probe was mounted on a specially designed and manufactured bracket, taking into consideration the alignment requirements and quick-release mechanism. Figure 3-13 present the probe bracket mounted on the metrology frame.
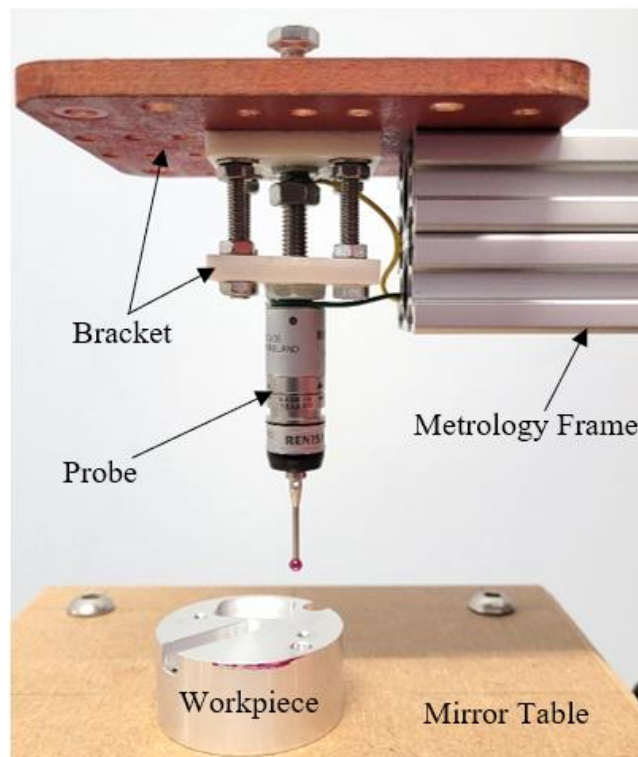
Figure 3-13: Bracket mounting the touch trigger probe.

3.3.2 The control system

This study uses a universal g-code platform (GRBL firmware) to enable the motion control of the stepper motors. Figure 3-14 is the typical integrated configuration of the hardware. The connection is made via the USB interface, which transmits both G-code commands to the controller and the information about the current axis positions back to GRBL. Then GRBL uses this information to control the 3D model to move parallel to the real axes. The control system enables the user to manipulate the probe to a required

position within the workspace. Since the machine relies on a single laser distance reading, it can move in only one coordinate direction at a time. Consequently, the control system permits movements solely along the three perpendicular directions: x, y, and z.

The stepper motor converts a pulsing electrical current, controlled by a stepper motor driver, into a discrete rotation movement. Then the probe will approach the workpiece with a gradual decrease in speed. This is achieved by dividing the travel distance until the probe contacts the workpiece, and a signal will command the motor (s) to stop. The determination of the probe positioning will continuously require the acquisition of the distance between the mirror and the displacement sensor and the kinematic model. In principle, the position of the probe (coordinates of the probe) is identified after every movement by solving a kinematic model. This is supported by understanding the direction of the translation. The position coordinates of the probe are received and used to calculate the size of the distance travelled by the probe (e.g., dimensions of the workpiece). x_0
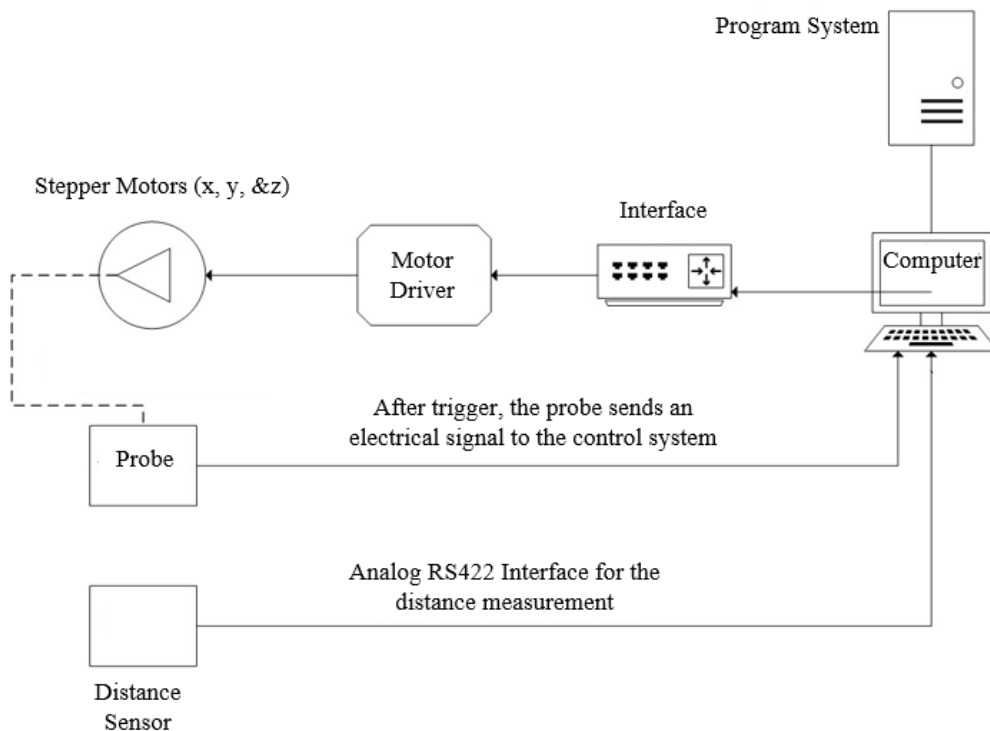
Figure 3-14: Control System [112].

3.3.3 Mirror table

The function of the mirror table assembly is to support the workpieces and secure the mirror. The mirror table is designed to be stable in between the calibrations and to fulfil the long-term stability demands. The design of the mirror table has three parts; the first part is the table support, which is fixed to the manipulation system, and it supports the table and the mirror. The table support is manufactured from 80 x 80 mm t-slot aluminium extrusion to provide stiffness. Both the table and the mirror were manufactured from medium-density fibreboard (MDF) wood. The MDF is a dense, flat, smooth, stiff, has no knots, and is easily machined wood type material. It consists of fine particles that contains no voids and delivers sharp edges with no tear out. It is most economic, and the surface is suitable for the laser beam. The table and the mirror are both spring-loaded and independently fixed to the main table.
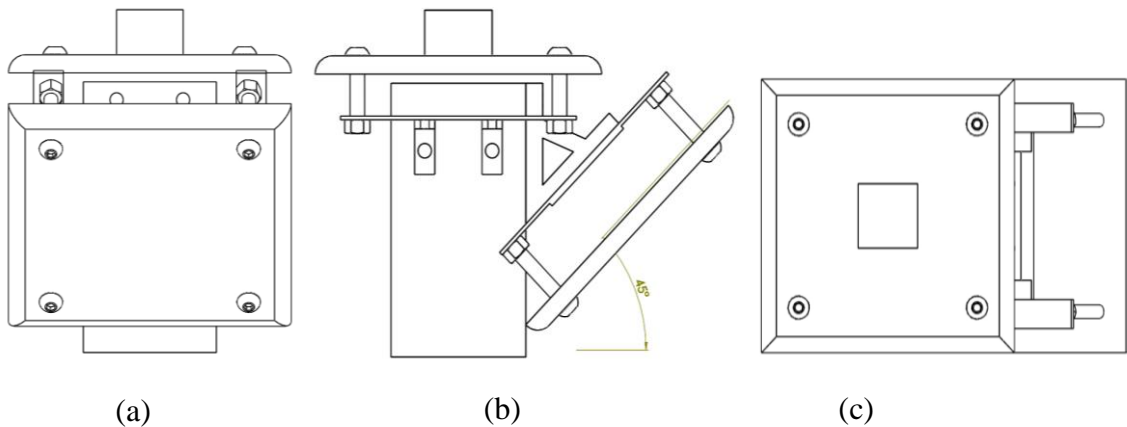
Figure 3-15: The mirror table showing (a) the front view, (b) the side view, and (c) the top view of the mirror table.

According to Ruijl [53], the mirror table is a very important part of the metrology system since it can introduce geometric measuring errors. The mirror table must fulfil long-term stability demands in between the calibrations. These geometric errors are introduced to the flatness deviation and out-of-squareness of the mirror. Therefore, a calibration model is required for the mirror to fulfil the accuracy demands.

3.4   Manipulation system

Figure 3-17 presents the traditional stacked structure manipulation system. The manipulation system is used to translate the mirror table in both x and y direction. The bottom stage translates the mirror table in x-axis direction while the top stage translates in the y-axis directions. The x-directional stage is fixed to the structural base such that the y-stage can be translated in the x-directions along the x-guideways.

Figure 3-6 present the measurement with the staked manipulation system, where the line of measurement remains in collinear with the line of the displacement sensor. Meaning the Abbe principle is met. However, individually, x, y dimension in the horizontal plane both have the first-order measurement errors resulting from the first-order error arm as the one-dimensional measurement system. The Abby offsets distances H_x and H_y between the rolling elements of x and y stages and the line of measurement is greater, hence the straightness of the rail and the roundness of balls will impact the accuracy significantly. Error compensation techniques such the geometric error modeling in Chapter 6 is suggested to reduce the impact of them for the two-dimensional measurement systems which have stable structures. Figure 2-2 and Figure 2-3 depict the possible error.
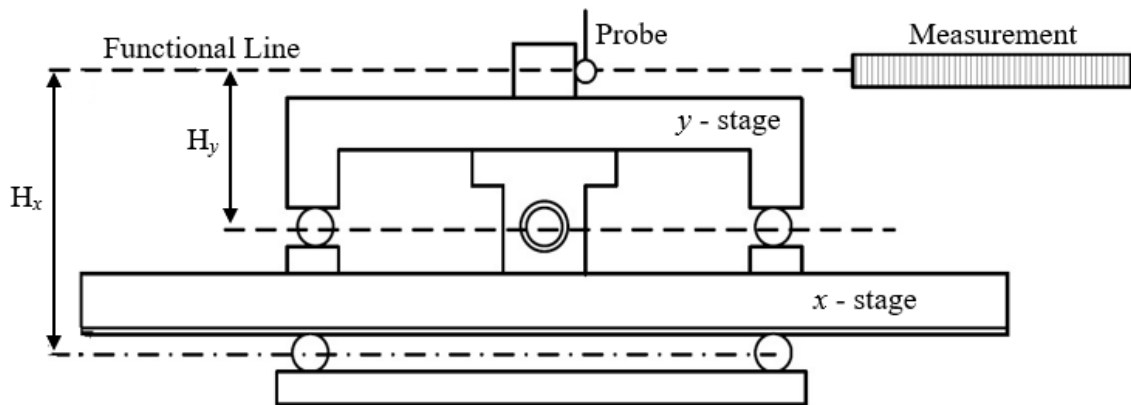
Figure 3-16: 2-D measurement staked manipulation system.

Considering the staked stage for the novel design, both *x* and *y* linear stages are identical, with 6 mm think aluminum plate fixed on the linear bearings sliding on 12 mm diameter

chrome rod. NEMA 23 stepper motors are used to provide discrete positioning in the travel stroke of 50 mm. A mirror table is fitted at the center of the manipulations system.
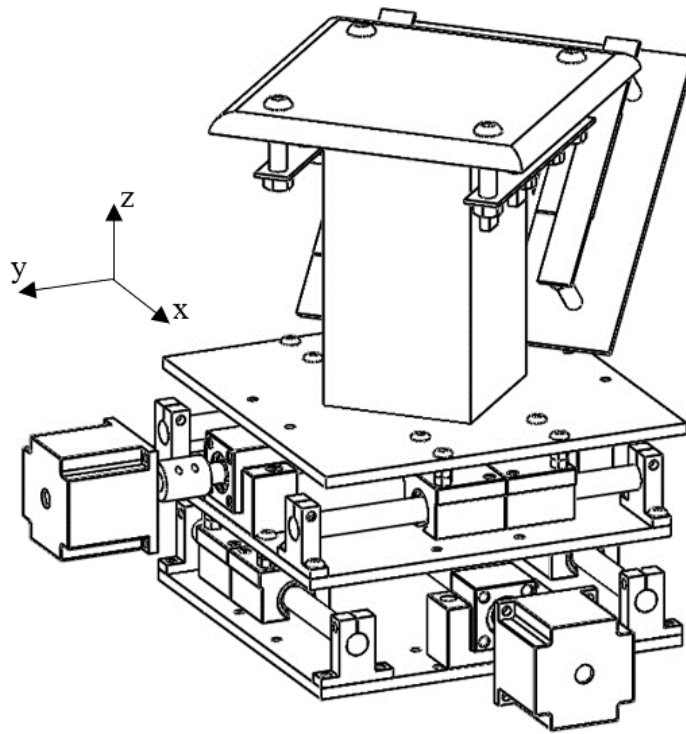
Figure 3-17: The mirror table suspended on the manipulation system.

In view of the drawbacks of the staked stage a coplanar stage structure two-dimensional measurement system is proposed when redesigning for the commercial purposes. With the coplanar stages, the oriented surface of the x, y two-dimensional movement rail is coincident with the measurement surface of working table. The first-order measurement errors due to not coinciding can be eliminated based on this "coplanar" orientation. The measured parts are fixed on the surface of working table in the measurement.

3.5   Model design of the machine

Figure 3-18 shows the complete design of a novel CMM with a maximum workspace volume of 40 x 40 x 20 mm³. The overall dimensions of the machine are given in

Appendix A. The machine is subject to more developments regarding the structure, metrology systems, drive mechanism, and control system to a more accurate system to minimize possible deformation. The purpose of this prototype and the reason for the choice of the material and components used was to validate and introduce a novel design. However, a more sophisticated design with high accuracy is considered. Considering the outcomes of the design and the kinematic model suggest the effectiveness of the system.
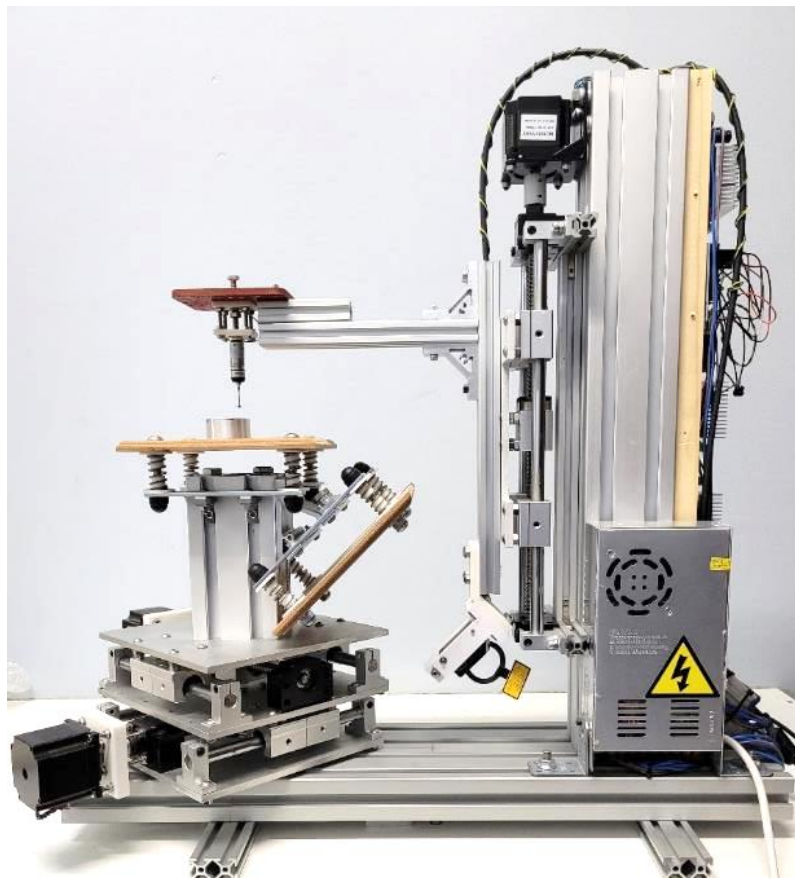
Figure 3-18: Novel CMM Design

3.6   Advantages of the novel design

The main advantages and the improvement over current existing technology include:

- The decrease in the number of distance sensors.

- The machine can measure 3D objects using only one displacement sensor instead of three.

- Abbe's error is theoretically eliminated because the functional line of the displacement sensor is always fixed o the tip of the probe.

- The metrology frame and structural frame are separated, and the motors are not mounted on the metrology frame.

3.7 Disadvantages

- The aim of the design was more to prove the kinematic modelling and the error modelling proposed in this study for one displacement sensor.

- Thus, the construction of the machine can further be improved to meet high occurrence and repeatability or and for commercial purposes.

- The construction of the machine and the material selection is to be considered to minimise the geometric and thermal errors.

- The functional line of the displacement sensor cannot be proven to be at the centre of the probe tip. Therefore, the alignment procedure is to be developed as well as the error compensation model.

- The stacking of the manipulation system is to be redesigned; the coplanar stage is highly recommended.

Chapter 4:

Kinematic modelling of the novel CMM

4. Kinematic modelling of the novel CMM

4.1 Coordinate system

Figure 4-1 is the novel design discussed in this study with the representation of the global coordinate system. The laser beam and associated components are employed to derive the kinematic modelling and error modelling discussed in this chapter. Detailed coordinate systems x-y plane and x-z plane are given in Figure 4-3 and Figure 4-2.
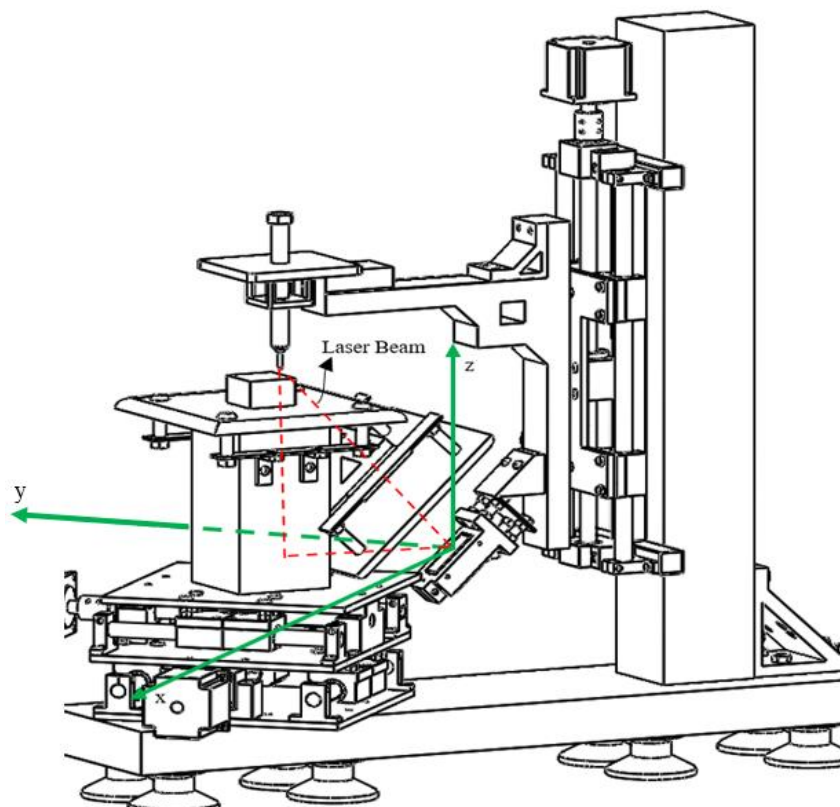
Figure 4-1: The presentation of the novel CMM coordinate system.

Figure 4-2: The presentation of the metrology frame translation in x and y-axis.

Figure 4-3: The presentation of the metrology frame translation in z-axis.

4.2 Kinematic model with Denavit–Hartenberg (DH) convention

A manipulator is composed of prismatic joints, where x and y axis are stagged together to a traditional x-y stage on the base of the structural frame, and the z-axis with the end-effector that is fixed separately on the vertical member of the structural frame, see Figure 4-4 and Figure 4-5. Calculating the position and orientation of the end-effector a forward kinematics is employed. According to Kucuk and Bingul [113] to have forward kinematics for a robot mechanism in a systematic manner, one should use a suitable kinematics model. In this study a Denavit-Hartenberg method is used with four parameters to describing the robot kinematics. Figure 4-6 shows the coordinate frame assignment for the manipulator.
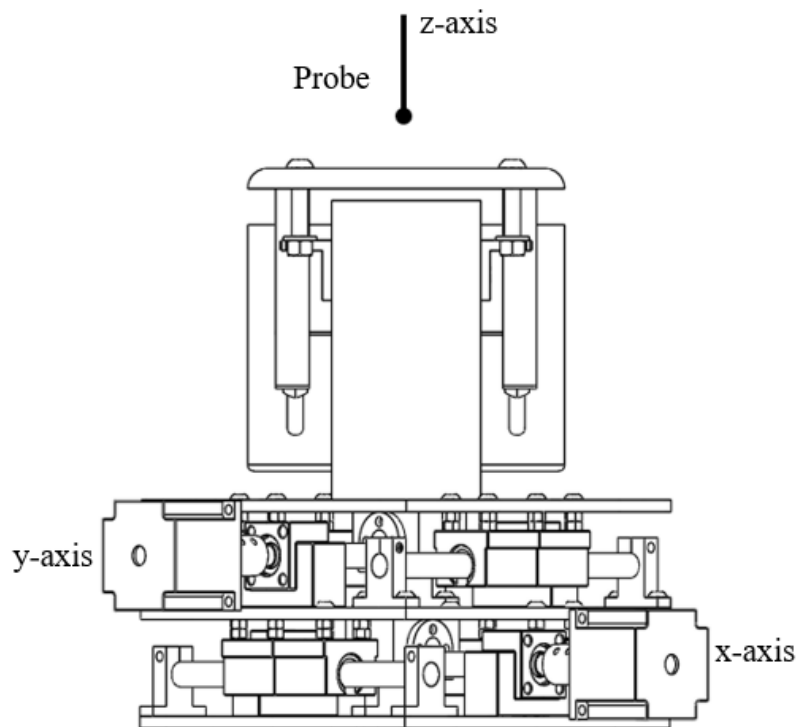
Figure 4-4: Side view of the x-y manipulation system with the mirror table.
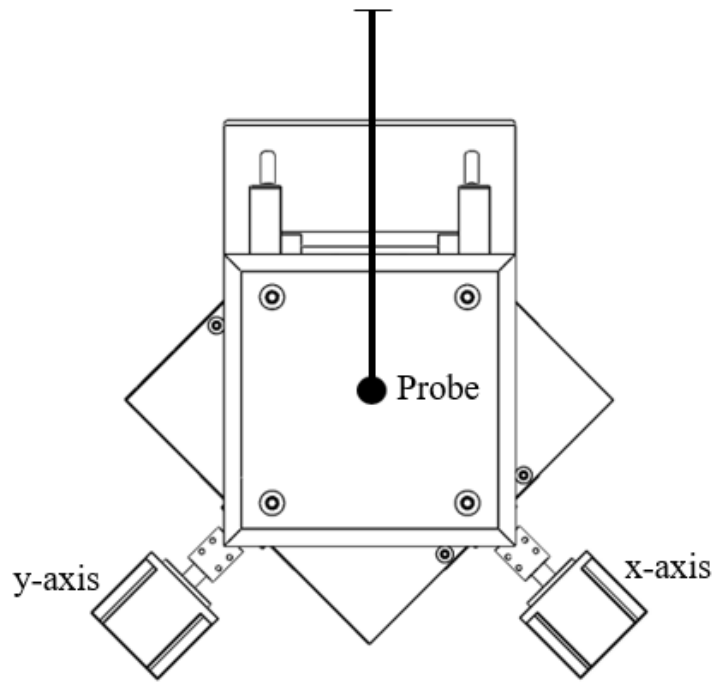
Figure 4-5: Top view of the x-y stage manipulation system with mirror table.
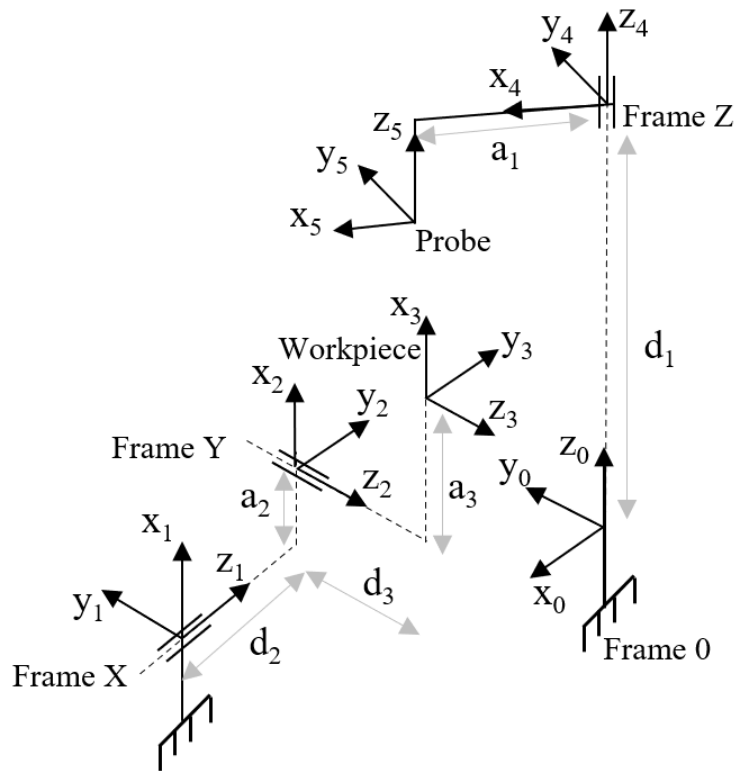
Figure 4-6: The demonstration of three-link Cartesian robot.

Where frame 0 to frame 3, present the x, y and z axis, and the probe, respectively. The distance from z_{n-1} to z_n measured along x_{n-1} is assigned as a_{n-1}, the angle between z_{n-1} and z_n measured along x_{n-1} is assigned as α_n, the distance from x_{n-1} to x_n measured along z_n is assigned as d_n and the angle between x_{n-1} to x_n measured about z_n is assigned as θ_{n-1}. The parameter r_n is the translation distance of the prismatic joint. From the assignment of DH frames, one can then determine the DH parameters. Table 4-1 presents the DH parameters corresponding to the above assignment of frames.

Table 4-1: DH parameters for the cartesian manipulator.

Frames	a_i	α_i	d_i	θ_i
0-4	0	0	d_1	45^0
4-5	a_1	0	0	0
1-2	a_2	90^0	d_2	0
2-3	a_3	0	d_3	0

Therefore, the general transformation matrix $^{n-1}_nT$ for a single link can be obtained by equation (12).

$$^{n-1}_nT = \begin{bmatrix} \cos\theta_i & -\sin\theta_i\cos\alpha_i & \sin\theta_i\cos\alpha_i & a_i\cos\theta_i \\ \sin\theta_i & \cos\theta_i\cos\alpha_i & -\cos\theta_i\sin\alpha_i & a_i\sin\theta_i \\ 0 & \sin\alpha_i & \cos\alpha_i & d_i \\ 0 & 0 & 0 & 1 \end{bmatrix} \qquad (12)$$

Therefore, the transformation matrix for each frame can be presented by equation (13 – 15).

$$
{}^0_4T = \begin{bmatrix} \dfrac{\sqrt{2}}{2} & -\dfrac{\sqrt{2}}{2} & \dfrac{\sqrt{2}}{2} & 0 \\ \dfrac{\sqrt{2}}{2} & \dfrac{\sqrt{2}}{2} & 0 & 0 \\ 0 & 0 & 1 & d_1 \\ 0 & 0 & 0 & 1 \end{bmatrix} \tag{13}
$$

$$
{}^1_2T = \begin{bmatrix} 1 & 0 & 0 & 0 \\ 0 & 0 & -1 & 0 \\ 0 & 1 & 0 & d_2 \\ 0 & 0 & 0 & 1 \end{bmatrix} \tag{14}
$$

$$
{}^2_3T = \begin{bmatrix} 1 & 0 & 0 & 0 \\ 0 & 1 & 0 & 0 \\ 0 & 0 & 1 & d_3 \\ 0 & 0 & 0 & 1 \end{bmatrix} \tag{15}
$$

The forward kinematics of the end-effector with respect to the base frame is determined by multiplying all the ${}^0_3T$ matrices to formulate equation (16).

$$
{}^0_5T = {}^0_4T \cdot {}^1_2T \cdot {}^2_3T = \begin{bmatrix} \dfrac{\sqrt{2}}{2} & -\dfrac{\sqrt{2}}{2} & \dfrac{\sqrt{2}}{2} & 0 \\ 0 & 0 & -1 & -d_1 \\ \dfrac{\sqrt{2}}{2} & \dfrac{\sqrt{2}}{2} & 0 & (d_2 + d_3) \\ 0 & 0 & 0 & 1 \end{bmatrix} \tag{16}
$$

4.3 Probe position formulation

The probe position is identified after every movement by solving the kinematic model of the machine, knowing the direction of the movement, and the distance between the displacement sensor and the mirror. The model discussed in this study demonstrates the relationship between the joints of the coordinates and the probe position and the orientation. The change in the probe position is defined with respect to the reference

coordinate system. Assume that the laser beam is theoretically fixed to the tip of the probe in all directions (x, y, and z). Thus, the equations below are presented with respect to the change in distance between the displacement sensor and the mirror.

In reference to Figure 4-2 and Figure 4-3 the origin of the coordinate system is where the measurement of the displacement sensor is equal to zero and is presented by a_0 (x_0, y_0, z_0). The translated original positions are presented by a_x (x_i, y_0, z_0), a_y (x_0, y_i, z_0) and a_z (x_0, y_0, z_i) respectively. The initial probe position is demonstrated by P_0 (x_0, y_0, z_0) and when translated to x, y and z is given as P_x (x_i, y_0, z_0), P_y (x_0, y_i, z_0) and P_z (x_0, y_0, z_i). L_0 is a laser beam measurement between the displacement sensor and the mirror and is presented by L_{0x}, L_{0y} and L_{0z} when the machine is translated in x, y or z-axis. L_2, L_{2x}, L_{2y} and L_{2z} are the hypotenuse components of the laser beam measurement when in zero position and translated. L_1, L_{1x}, L_{1y} and L_{1z} are the extended distances at various translations of the laser beam from the mirror to the probe, with the horizontal components of L_3, L_{3x}, L_{3y} and L_{3z} when probing in different directions. The point of contact by the laser beam to the mirror is presented by b_0, b_x, b_y and b_z and the other points such as c_0, c_x, g_0, g_x, k_0, k_x, e_x, f_y and i_z are the points of intersection concerning the specified vector. Theoretically, the probe angles and the position of the mirror are set at 45° to all the sides of the coordinate system. The z-plane and x-y plane angles of the laser beam measurement and the mirror are presented by φ and Θ, and β and α respectively.

4.3.1   Modelling of the probe position(s) in the x-axis

The position of the probe and the distance between two positions in x-axis are formulated in reference to Figure 4-2. Where the position in x-axis is described by P_x (x_1, y_0, z_0), and the distance between two probe positions in x-axis is Δx. From the global coordinate system x_1 can be formulated as expressed in equation (17) and equation (18).

$$x_1 = x_0 + \Delta x$$
(17)

$$x_0 = (L_{2x} + L_{3x}) \sin \theta$$
(18)

Δx is the distance between P_0 and P_x and is given by equation (19). To find Δx triangle $b_1 \overset{\wedge}{a_0} c_0$ and the translated triangle $b_x \overset{\wedge}{a_x} c_x$ are employed to determine the distance $b_1 b_x$ which is equal to the component of $P_0 P_x$.

$$b_1 b_x = \frac{b_1 e_x}{\sin \alpha}$$

$$b_1 b_x = \frac{b_1 c_0 - b_x c_x}{\sin \alpha}$$

$$b_1 b_x = \frac{L_2 \cos \theta - L_{2x} \cos \theta}{\sin \alpha}$$

Therefore, $P_0 P_x$ (Δx) can be calculated as follows.

$$P_0 P_x = \Delta x = \frac{L_2 \cos \theta - L_{2x} \cos \theta}{\sin \alpha \cdot \cos \theta}$$

$$\Delta x = \frac{L_2 - L_{2x}}{\sin \alpha} \tag{19}$$

Therefore, equation (17) is transformed to equation (20).

$$x_1 = (L_{2x} + L_{3x}) \sin \theta + \frac{L_2 - L_{2x}}{\sin \alpha} \tag{20}$$

4.3.2 Modelling of the probe position(s) in the y-axis

The position of the probe and the distance measurements in y-axis is formulated in reference to Figure 4-2. The y-axis coordinates are described by position P_x (x_0, y_1, z_0), and the d difference between two points in y-axis will give the distance. From the global coordinate system y_1 can be formulated as expressed in equation (21) and equation (22).

$$y_1 = y_0 + \Delta y \tag{21}$$

$$y_0 = (L_{2y} + L_{3y}) \cos \theta \tag{22}$$

Δy is the distance between P_0 and P_y, and is given by equation (23), triangle $b_1 \hat{a}_0 g_0$ and the translated triangle $b_y \hat{a}_y c_y$ are used to determine the distance $b_1 b_y$ which is equal to the component of $P_0 P_y$.

$$b_1 b_y = \frac{b_1 f_y}{\cos \alpha}$$

$$b_1 b_y = \frac{b_1 g_0 - b_y g_y}{\cos \alpha}$$

$$b_1 b_y = \frac{L_2 \sin \theta - L_{2y} \sin \theta}{\cos \alpha}$$

Since $b_1 b_y$ is equal to the component of $P_0 P_x$ therefore, Δy expression is concluded by equation (19).

$$P_0 P_y = \Delta y = \frac{L_2 \sin \theta - L_{2y} \sin \theta}{\cos \alpha \cdot \sin \theta} = \frac{L_2 - L_{2y}}{\cos \alpha}$$

$$\Delta y = \frac{L_2 - L_{2y}}{\cos \alpha} \tag{23}$$

Therefore, equation (21) can be expressed by equation (24).

$$y_1 = \left(L_{2y} + L_{3y} \right) \cos \theta + \frac{L_2 - L_{2y}}{\cos \alpha} \tag{24}$$

4.3.3   Modelling of the probe position(s) in z-axis

The position of the probe and the distance between two positions in z-axis is formulated in reference to Figure 4-3. The z-axis coordinates are described by position P_1 (x_0, y_0, z_1), and the difference between two points suggest the distance. From the global coordinate system z_1 can be formulated as expressed in equation (25) and equation (26).

$$z_1 = z_0 + \Delta z \tag{25}$$

$$z_0 = (L_0 + L_1) \sin \varphi \tag{26}$$

Δz is the distance between P_0 and P_z, and is given by equation (27), to find Δz, triangle $b_0 \hat{a}_0 k_0$ and the translated triangle $b_z \hat{a}_z k_z$ are used to determine the distance $b_0 b_z$ which is equal to the component of $P_0 P_z$.

$$b_0 b_z = \frac{b_0 i_z}{\sin \beta}$$

$$b_0 b_z = \frac{b_0 k_0 - b_z k_z}{\sin \beta}$$

$$b_0 b_z = \frac{L_0 \cos \varphi - L_{0z} \cos \varphi}{\sin \beta}$$

Since $b_0 b_z$ is equal to the component of $P_0 P_z$ therefore, Δz can be expressed in equation (23).

$$P_0 P_z = \Delta z = \frac{L_0 \cos \varphi - L_{0z} \cos \varphi}{\sin \beta \cdot \cos \varphi}$$

$$\Delta z = \frac{L_0 - L_{0z}}{\sin \beta} \tag{27}$$

Therefore, equation (25) can be expressed as equation 28.

$$z_1 = (L_0 + L_1) \sin \varphi + \frac{L_0 - L_{0z}}{\sin \beta} \tag{28}$$

4.3.4 Expression with respect to the laser measurement (L0)

Equations (20), (24) and (28) can be represented with respect to the laser beam measurements (L_0), see equation (29), (30), and (31). Also, equations (19), (23), and (27) are represented by equations (32), (33), and (34) respectively.

$$x_1 = \left(\frac{L_{0x}}{\sin \varphi} + \left((L_{0x} + L_{1x}) \cos \varphi - \frac{L_{0x}}{\cos \varphi} \right) \right) \sin \theta + \frac{L_0 - L_{0x}}{\sin \alpha \cdot \cos \varphi} \tag{29}$$

69

$$y_1 = \left(\frac{L_{0y}}{\sin\varphi} + \left((L_{0y} + L_{1y})\cos\varphi - \frac{L_{0y}}{\cos\varphi}\right)\right)\cos\theta + \frac{L_0 - L_{0y}}{\cos\alpha \cdot \cos\varphi} \tag{30}$$

$$z_1 = (L_0 + L_1)\sin\varphi + \frac{L_0 - L_{0z}}{\sin\beta} \tag{31}$$

$$\Delta x = \frac{L_0 - L_{0x}}{\sin\alpha \cdot \cos\varphi} \tag{32}$$

$$\Delta y = \frac{L_0 - L_{0y}}{\sin\alpha \cdot \cos\varphi} \tag{33}$$

$$\Delta z = \frac{L_0 - L_{0z}}{\sin\beta} \tag{34}$$

Substituting from equation (16) the parameters d_1, d_2, and d_3 can be represented by x, y and z to formulate equation (35)

$$_5^0T = \begin{bmatrix} \dfrac{\sqrt{2}}{2} & -\dfrac{\sqrt{2}}{2} & \dfrac{\sqrt{2}}{2} & 0 \\ 0 & 0 & -1 & -z \\ \dfrac{\sqrt{2}}{2} & \dfrac{\sqrt{2}}{2} & 0 & (x+y) \\ 0 & 0 & 0 & 1 \end{bmatrix} \tag{35}$$

4.4　Measurement procedure

During the measurements, when the probe contacts the workpiece, a signal is sent to the computer control system commanding the motor(s) to stop. The position P_i (x_i, y_i, z_i) in the space can be found by solving the forward kinematic modelling described in section 4. Based on the developed model the input parameters required for kinematic modelling include the distance between the displacement sensor and the mirror, the position of angles of the mirror and the sensor measurement and knowing the direction of the translation and the axis. The following steps summarize the steps of the measurement control model of the machine:

1. Decide on the desired measurement of the workpiece.

2. Manipulate the system to make the first contact at position P_0 (x_0, y_0, z_0),

3. Record the distance L_0 between the distance sensor and the mirror.

4. Calculate the horizontal component if measuring on the x-y plane.

5. Move the probe along the workpiece in the desired direction to touch the second point P_i (x_i, y_i, z_i) and record laser measurement L_{0i} between the distance sensor and the mirror.

6. Use equations (29), (30) and (31) when calculating the position of the probe and (32), (33) and (34) when calculating the length of the workpiece.

7. Record the positions and the full dimension of the workpiece.

Figure 4-7 and Figure 4-8 present the path, the approach, and the retraction of the probe from the workpiece when measuring on x, y, and z-axis. The significance of the approach is considered at points 1-2, and 6-7 with approximately 1 mm   before touching the probe at a reduced speed of 15 mm/s. The retraction of the probe from the workpiece is presented by points 3-4 and 9-8. The black arrows present the direction of the probe as it approaches and retract from the workpiece.
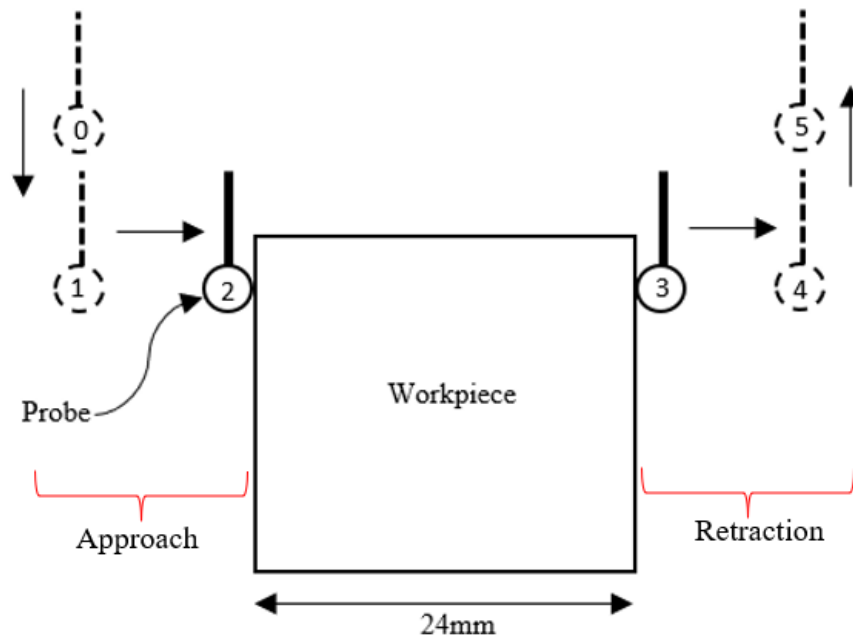
Figure 4-7: The approach and retraction of the probe when measuring in x-y plane
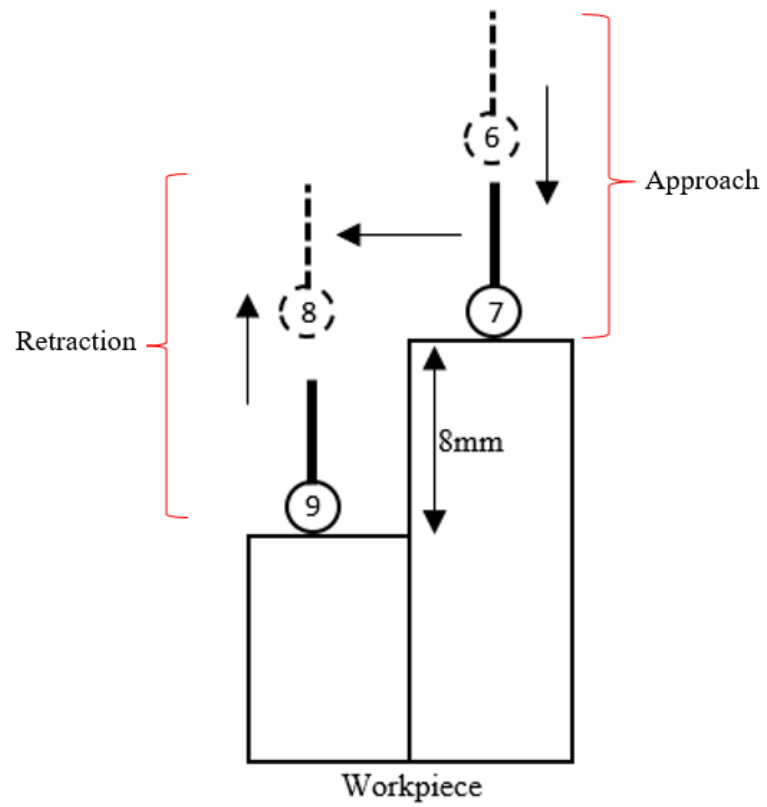
Figure 4-8: The approach and retraction of the probe when measuring in z plane

Chapter 5:

Kinematic model for Out of squareness of the mirror.

5. Kinematic model for Out of squareness of the mirror.

5.1 Introduction

Although the novel CMM adheres to Abbe's principle in the x, y, and z-axis, with unique key design considerations, there are obvious geometric errors that need to be calibrated. These errors would have been due to the manufacturing process of the machine with deviations from the ideal positioning. Thus, this study considered the calibration of the mirror out-of-squareness. The design assumes the displacement sensor to be accurately positioned at 45° of the coordinate systems, and the mirror as an adjustable component for the calibrations. Figure 5-1 demonstrates the translation and the direction of the axis, the optical triangle of the laser beam, and the mirror axis.
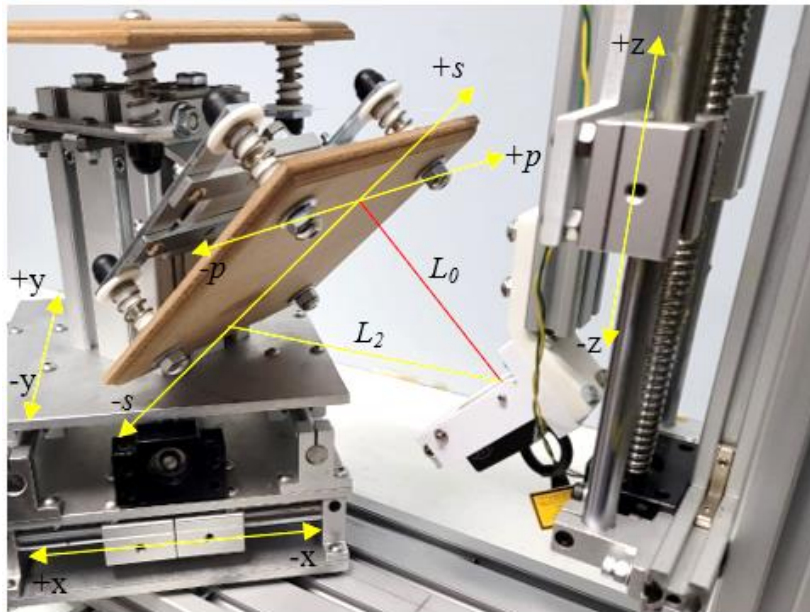
Figure 5-1: Demonstration of the coordinate system of the mirror p-s with the laser beam components

As recommended by Ruijl and Eijk [48], the calibration procedure discussed in this study is performed with standard machine tasks to prevent additional uncertainties that can be

introduced due to the deformation of the mirror table while it is being attached to the manipulation system. Also, the displacement sensor system is used for the calibration measurements.

5.2   Calibration with special triangle technique

The calibration method is based on the fundamentals of trigonometric special triangles of 45º presented in Figure 5-2. This technique is suggested by the nature of the optical triangles formed by the mirror and the laser beam of the displacement sensor.
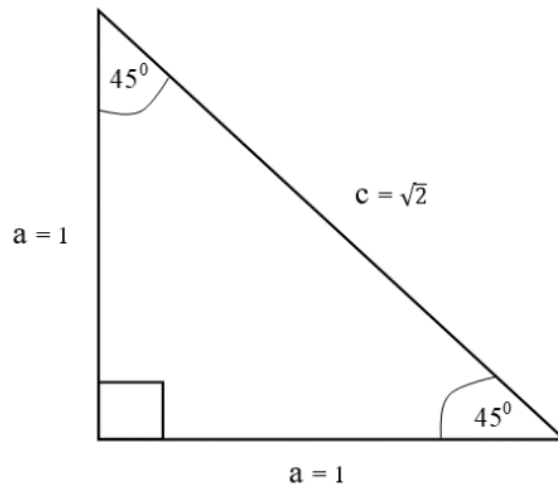
Figure 5-2: Special triangle of 45º

The special triangle is defined as a triangle with two 45º and one 90º. It is an isosceles right-angle triangle hence the length of the 2 sides is always equal. The consequence of having equal lengths is because of the two sides with equal angles. Since it is a right-angled triangle, Pythagoras' Theorem can be used to find the hypotenuse, so that the ratios of the length of sides are expressed as $1:1:\sqrt{2}$.

5.3   The fundamentals of the out-of-squareness calibration

Based on the fundamentals of the special angle and since the laser beam and the mirror are theoretically orthogonal, the optical triangles can be expressed as the components of the special angle. Figure 5-3 and Figure 5-4 presents the optical triangles with components, laser beam and mirror. The change of either side due to machine translation

suggests the new equal values on the equal sides of the triangle. Therefore, knowing the initial value of the laser beam measurement L_0 and the travel distance by laser pointers across the mirror T_{ti}, the value of the new laser beam measurement L_{0i} can be predicted. For the calibration, the theoretical value can be compared with the measured value, and the difference in the two values suggests the out-of-squareness of the mirror.
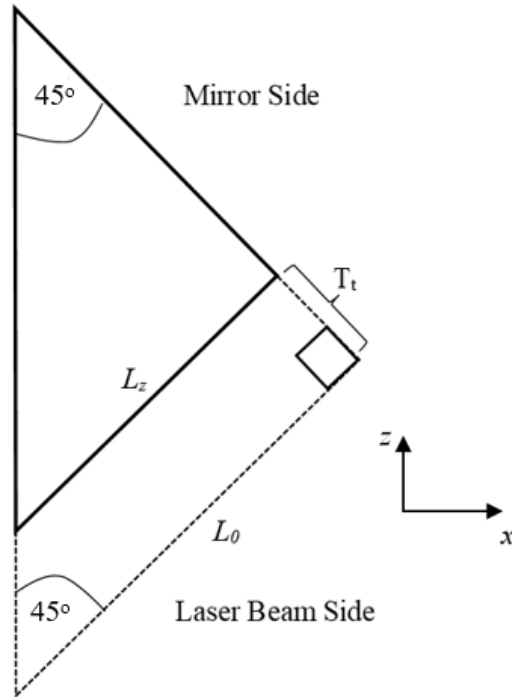
Figure 5-3: Optical triangle formed by the mirror and the displacement in the x-z plane.
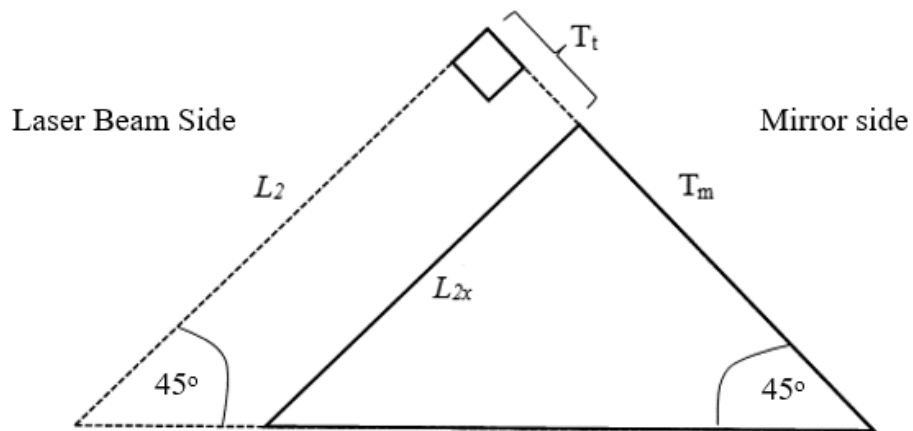
Figure 5-4: Optical triangle formed by the mirror and the displacement in the x-y plane.

5.4 Prediction of the new laser displacement after translation in x and y axis

Figure 5-5 presents the ideal translation of the mirror and the change of the laser distance component in the x-y plane. Where T_{mi} is the distance travelled by the machine/mirror in x and y directions respectively, T_{ti} is the difference between the displacement sensor measurement L_2 and the new laser measurement L_{2i}. The suffix i present the translation in x or y axis.
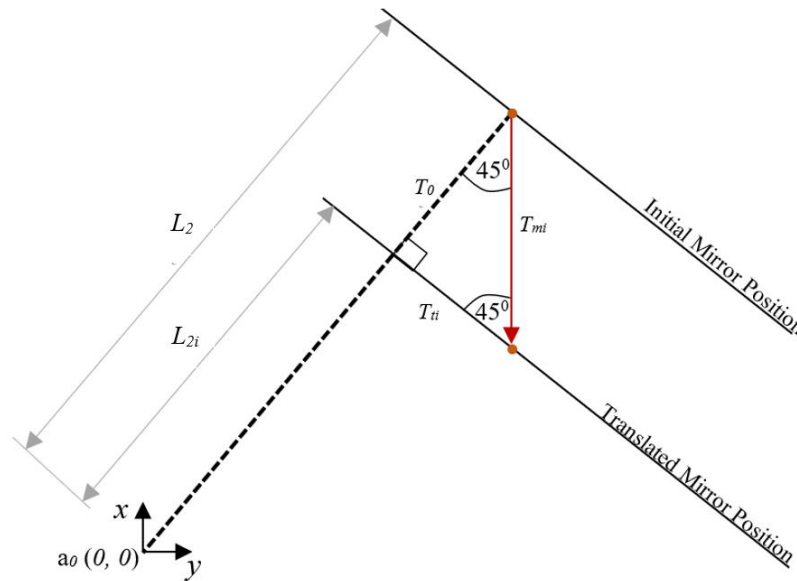
Figure 5-5: Optical triangle formed by the relationship between the mirror and displacement sensor in the x-y plane of the machine.

Therefore, based on the special triangle description discussed in section 5.2 of this chapter, equation (36), (37) and (38) can be formed in reference to Figure 5-5 to estimate the new positioning distance in the x and y directions.

$$L_{2i} = L_2 - T_{ti} \tag{36}$$

$$T_{ti} = T_{mi} \cdot cos\emptyset$$

$$L_{2i} = L_2 - (T_{mi} \cdot cos\emptyset)$$

$$L_{2i} = L_2 - (T_{mi} \cdot cos45^0)$$

$$L_{2i} = \left(\frac{L_0}{cos45} - (T_{mi} \cdot cos45^0) \right)$$

$$L_{0i} = \left(\frac{L_0}{cos45} - (T_{mi} \cdot cos45^0) \right) \times cos45^0 \qquad (37)$$

$$L_{0z} = \left(L_0 - (T_{mi} \cdot cos45^0) \right) \qquad (38)$$

Therefore, equations (37) and (38) can be used to estimate the new value of the measurement between the laser beam and the mirror.

5.5 Out-of-squareness error modelling

Figure 5-6 demonstrates the possibilities of out-of-squareness, here the mirror deviates from the theoretical position b_1 b_0'. The error possibilities can either be at an acute angle $b_1 b_{+i}$ or an obtuse angle $b_1 b_{-i}$. Due to the out-of-squareness in x and y axis the theoretical position b_0 of laser beam on the mirror changes to $b_0 b_{+i}$ or $b_0 b_{-i}$.
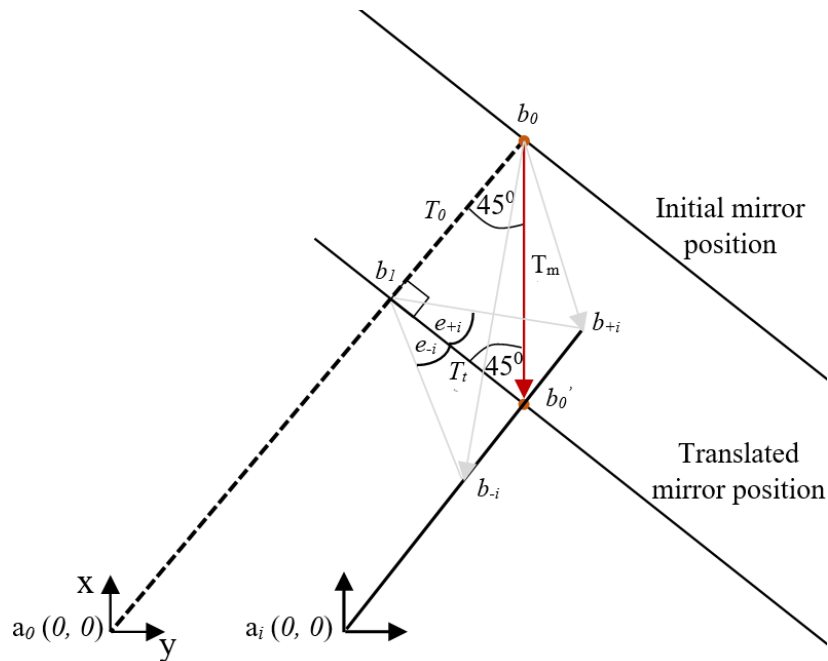
Figure 5-6: Out-of-squareness possibilities in *x* and *y* axis.

Therefore, the difference between the theoretical position $a_i b_0'$ and $a_i b_{-i}$ or $a_i b_{+i}$ suggests out-of-squareness of the mirror which can be presented by the error angles e_{-i} or e_{+i} respectively. See equation (39) and (40).

$$b_{-i}\, b_{0i}' = a_i b_0' - a_i b_{-i} \tag{39}$$

$$b_0' b_{+i} = a_i b_0' + a_i b_{-i} \tag{40}$$

Where $a_i b_0'$, is the ideal hypotenuse component of the imaginary laser distance L_{0i} and $a_i b_{-i}$ and $a_i b_{+i}$ are the measured hypotenuse component values. Therefore, assuming the laser beam is at 45° for both theoretical and for actual calculations, equation (39) and equation (40) can be expanded as follows.

$$b_{-i}\, b_0' = \left(\frac{L_0}{cos\varphi} + T_{mi}cos\alpha\right) - \frac{L_{0i}}{cos\varphi}$$

$$b_0' b_{+i} = \left(\frac{L_0}{cos\varphi} - T_{mi}cos\alpha\right) + \frac{L_{0i}}{cos\varphi}$$

The error angle of the mirror e_{-i} and e_{+i} can be calculated as follows:

$$e_{-i} = tan^{-1}\left(\frac{b_{-i}\, b_0'}{T_{mi} \times cos\alpha}\right)$$

$$e_{-i} = tan^{-1}\left(\frac{\left(\frac{L_0}{cos\varphi} + T_{mi}cos\alpha\right) - \frac{L_{0i}}{cos\varphi}}{T_{mi} \times cos\alpha}\right)$$

$$e_{+i} = tan^{-1}\left(\frac{b_{+i}\, b_0'}{T_{mi} \times cos\alpha}\right)$$

$$e_{+i} = tan^{-1}\left(\frac{\left(\frac{L_0}{cos\varphi} + T_{mi}cos\alpha\right) + \frac{L_{0i}}{cos\varphi}}{T_{mi} \times cos\alpha}\right)$$

The formula for the out-of-squareness error can be summarised as follows depending on the machine translation, where e_x, e_y and e_z are the respective error angles when the machine is translated in respective axis, see equation (41), (42), and (43).

$$e_x = tan^{-1}\left(\frac{L_0}{T_{mx} \times cos\alpha \times cos\varphi} \pm 1 \pm \frac{L_{0_x}}{T_{mx} \times cos\alpha \times cos\varphi}\right) \quad (41)$$

$$e_y = tan^{-1}\left(\frac{L_0}{T_{my} \times cos\alpha \times cos\varphi} \pm 1 \pm \frac{L_{0_y}}{T_{my} \times cos\alpha \times cos\varphi}\right) \quad (42)$$

$$e_z = tan^{-1}\left(\frac{L_0}{T_{mz} \times cos\beta} \pm 1 - \frac{L_{0_z}}{T_{mz} \times cos\beta}\right) \quad (43)$$

5.6 Calibration procedure

The calibration is performed in all directions of measurement. Assume Figure 5-6 presents the movement of the machine during the calibration method.

1. Position the probe at position P_0 (x_o, y_o, z_o) and record L_0.
2. During the calibration in the x-y plane; calculate L_2 (the hypotenuse of L_0).
3. Determine the translation distance of each axis.
4. Predetermine the new laser beam distance using equation (37) for the x and y-axis, and equation (38) for the z-axis.
5. Move the machine to the desired position based on the defined travel distance.
6. Compare the predetermined positioning distance and the actual reading.
7. If not comparable adjust the mirror mechanically using the four fine threaded Allen cap screws and repeat the process.

Chapter 6:

Mirror out-of-squareness experimental evaluation and calibration

6. Mirror out-of-squareness experimental evaluation and calibration

6.1 Introduction

During the assembly process of the machine the mirror is susceptible to rotation from s – r plane hence the calibration. Figure 6-1 demonstrate an example of possible rotation to s'-r' plane. Thus, this section of the study discusses the calibration of the mirror using the self-calibration method. The displacement sensor is employed to determine the rotation of the mirror. The as found position of the mirror is established, and the mirror is mechanically adjusted. Then the final position of the mirror is presented. A Monte Carlo simulation is conducted to realise the uncertainty of the mirror.
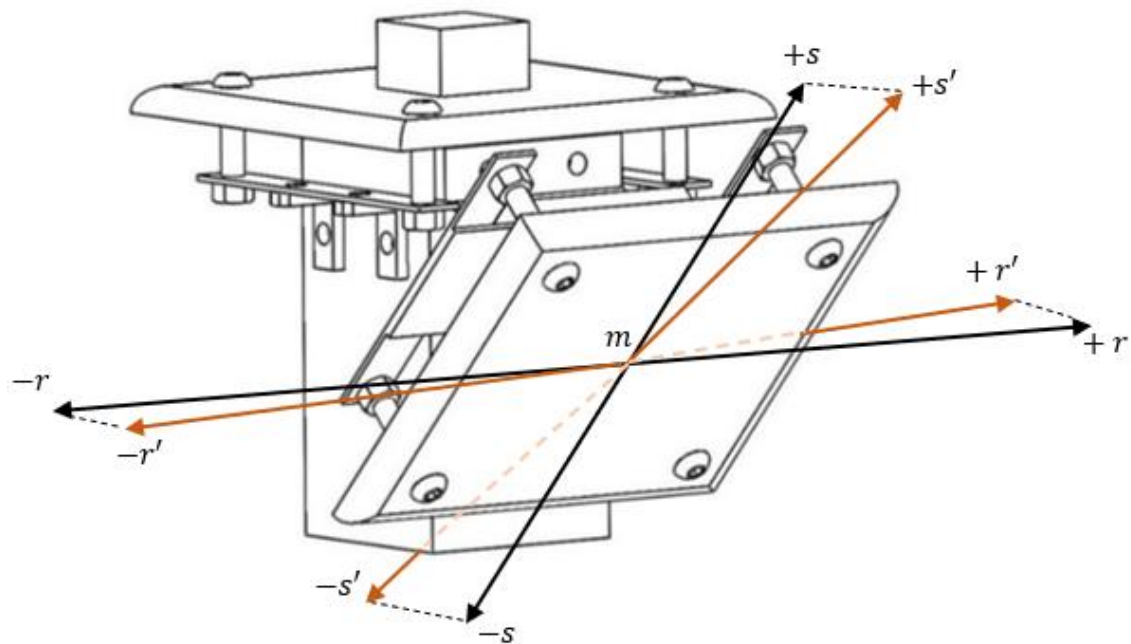
Figure 6-1: The rotation of the mirror about s-r plane

Figure 6-2 present the laser pointer projected on the mirror as the red dots, and the travel path when the machine is translated in positive and negative translations (+x, +y, +z and

-x, -y, -z). Table 6-1 summarizes the relationship between the laser dot and the translations of the machine.
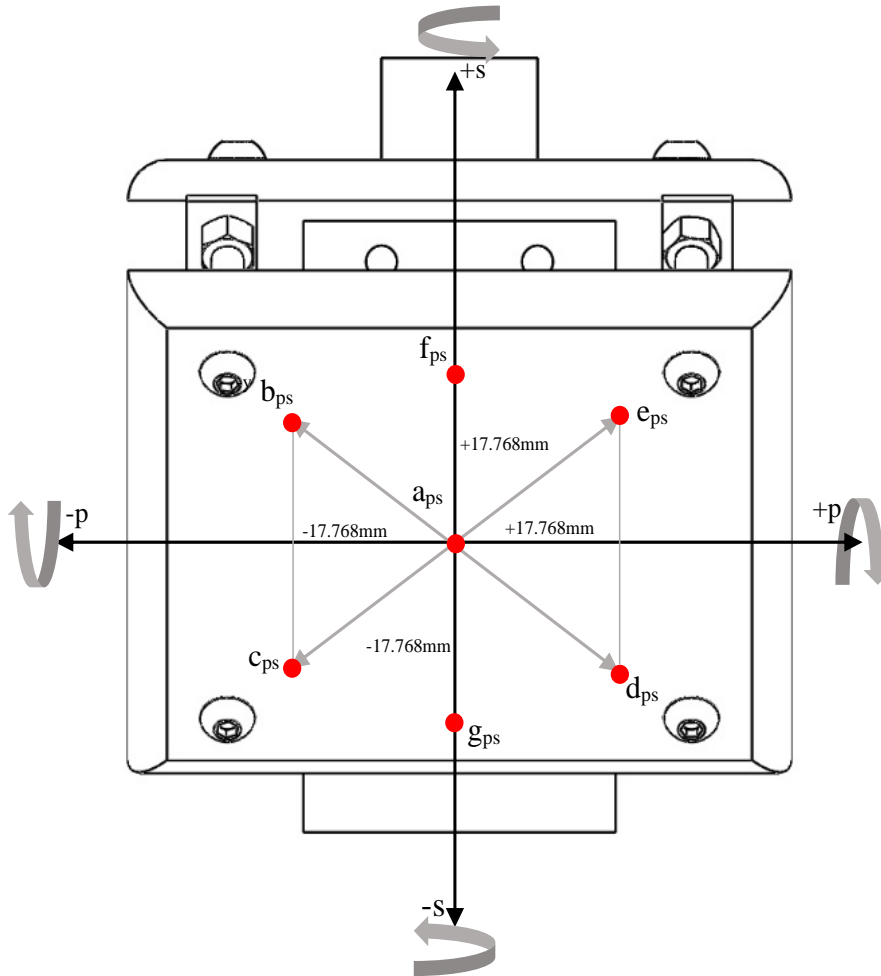
Figure 6-2: Displacement positions of the laser pointer

Table 6-1: Relationship between machine translation and
the displacement vector of the laser pointer,

Machine Translation	Displacement sensor laser pointer path
x	c_{ps} e_{ps}
Y	b_{ps} d_{ps}
Z	g_{ps} f_{ps}

6.2 Mirror calibration

To establish the as found position of the mirror the machine was translated by 50 mm through the paths describe in Table 6-1. The displacement sensor measurements were recorded including L_0, L_{0x}, L_{0y} and L_{0z}. Equation 37 and 38 were employed to predict the expected measurement of the displacement sensor L'_{0x}, L'_{0y} and L'_{0z}. The translation on each axis direction was repeated ten times, Table 6-2 shows the average results for each axis. Full measurements can be seen in Appendix E-1.

Table 6-2: The results before the calibration.

Machine Translation	Displacement sensor laser pointer path	Average measured value (L'_{0i}) (mm)	Average calculated value (L_{0i}) (mm)	Difference for adjustments mm
x	$c_{ps}\, e_{ps}$	66.393	66.549	0.156
Y	$b_{ps}\, d_{ps}$	66.329	66.501	0.172
Z	$g_{ps}\, f_{ps}$	61.311	61.543	0.232

The difference between the measured and calculated value suggested the adjustment of the mirror. The calibration was performed by adjusting the Allen cap screw securing the mirror to the table until the difference is reduced. The Allen caps were secured and the translation on each axis was repeated 10 time, see the samples in Appendix E-2. Table 6-3 present the results obtained after the calibration. Figure 6-3 shows the difference before and after the calibration.

Table 6-3: Calibration results.

Machine Translation	Displacement sensor laser pointer path	Average measured value (L'_{0i}) (mm)	Average calculated value (L_{0i}) (mm)	Difference for adjustments (mm)
x	$c_{ps}\, e_{ps}$	66.392	66.388	-0.004
Y	$b_{ps}\, d_{ps}$	66.328	66.329	0.001
Z	$g_{ps}\, f_{ps}$	66.309	66.311	0.002
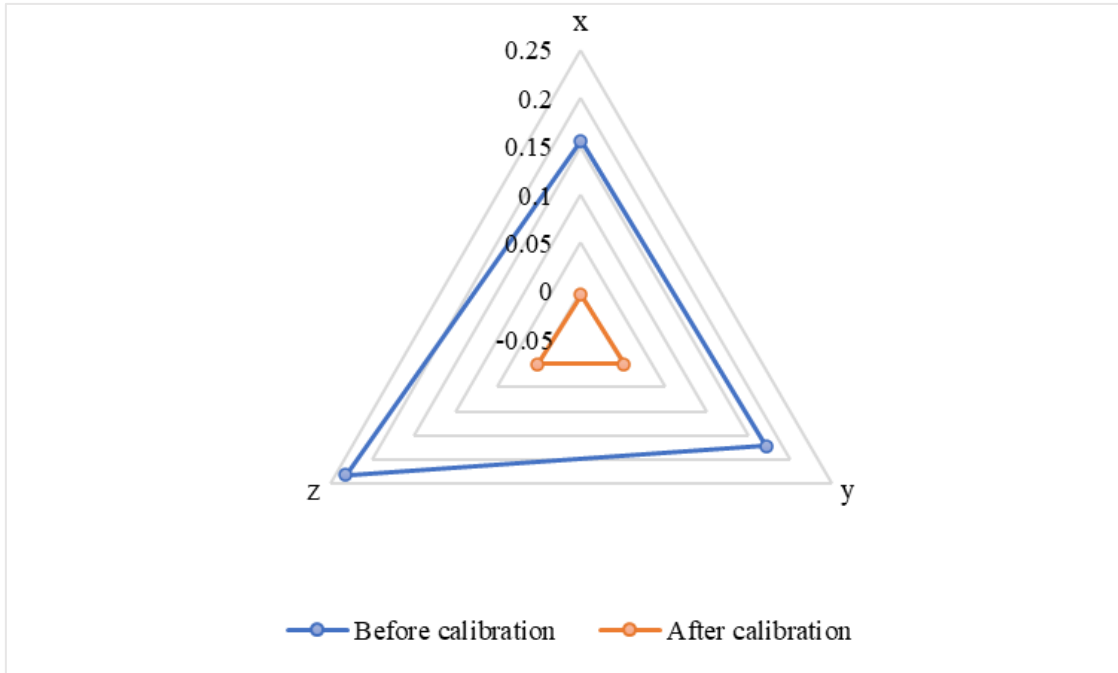
Figure 6-3: The calibration results before and after in mm.

The calibration results are used to compute the out-of-squareness error with equation 41, 42 and 43. The error results before and after the calibration are given in Figure 6-4 to Figure 6-7. The angle of the mirror was compensated with the established out-of-squareness error and the new angle (α_x, α_y, and β_y) are given in Table 6-4.
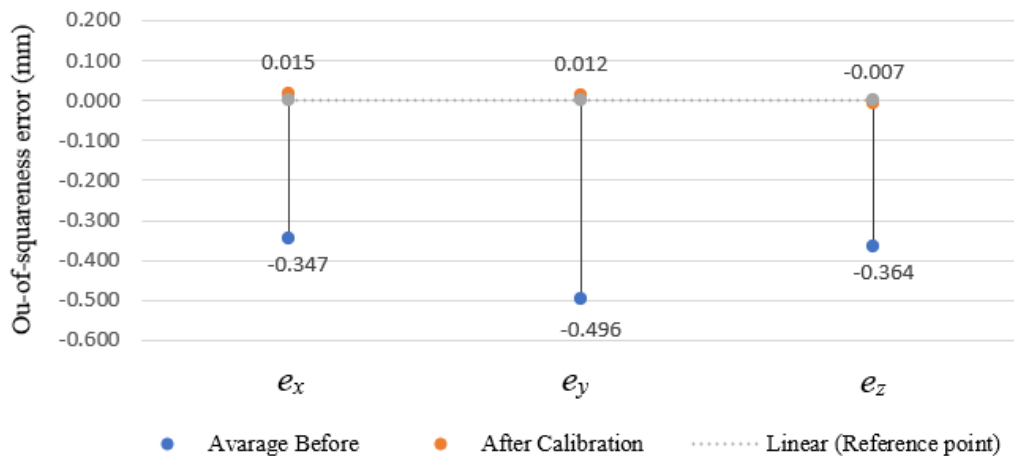
Figure 6-4: Mirror out-of-squareness error before and after the calibration.
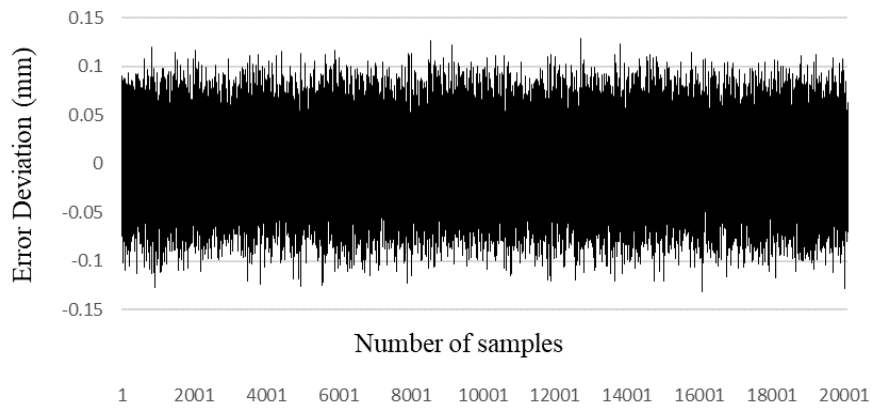
Figure 6-5: Error deviation in the x-axis
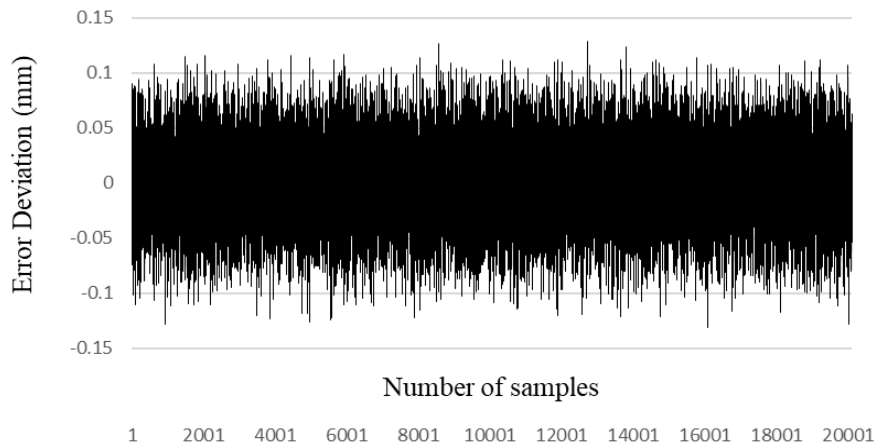
Figure 6-6: Error deviation in the y-axis
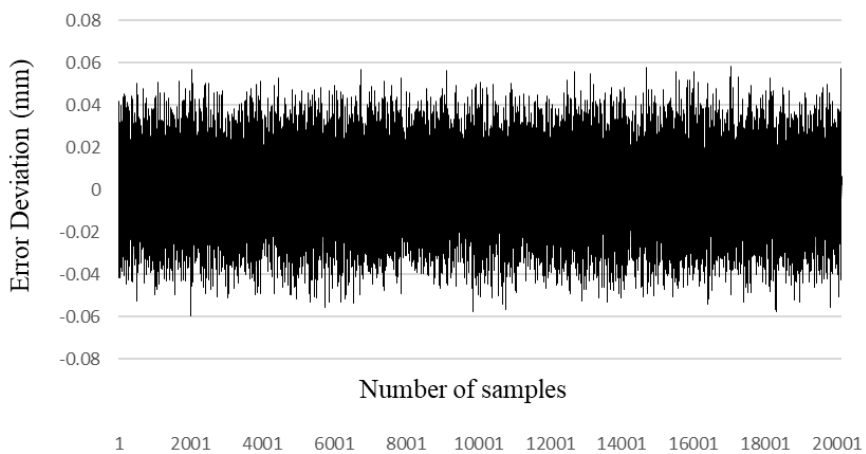
Figure 6-7: Error deviation in the z-axis

6.3 Measurement uncertainty with Monte Carlo simulation

The Monte Carlo simulation is employed as a preferred method to compute the measurement uncertainty following the calibration. Microsoft Excel RAND () function was used to generate random variables, running the Monte Carlo simulation with $M = 20$ 000 trials. Table 6-4. presents the input variables for the measurement equations 28, 29, and 30.

Table 6-4: Input variables with the associated mean value

Measurement function	Inputs Variables	Mean (μ) (mm)
Δx	L_0	91.394
	L_{0x}	66.388
	α_x	44.986
Δy	L_0	91.331
	L_{0y}	66.326
	α_y	44.987
Δz	L_0	96.662
	L_{0z}	61.311
	β_y	45.007

During the simulation, the number of trials (M) were determined using GUM Supplement 1 recommendation by following the general rule, see equation (44), to provide a reasonable representation of the expected result:

$$M > \frac{10^4}{1 - p} \tag{44}$$

Where $50p\%$ is the selected coverage probability. So, for example, when the chosen coverage probability is 50%, $p = 0.50$ and M should be at least higher than 20,000. In each run $M, (M = 1, ..., N)$, a random error value is generated. The probability density

function used in this study that best represents the real-valued random variables whose distributions are not known is a Gaussian distribution see equation (45). Each distribution has μ as the mean value and σ standard deviation.

$$g_i(\tau) = \left(\frac{1}{\sqrt{2\pi} \times u(i)} e^{\left(-\frac{(\tau-i)^2}{2u^2(i)} \right)} \right) \tag{45}$$

6.4   Uncertainty results

Figure 6-8 to Figure 6-10 show the histogram of the Monte Carlo Simulation results following the measurement of approximately 50 mm. Table 6-5 to Table 6-7 contains the statistical parameters corresponding to the histogram.
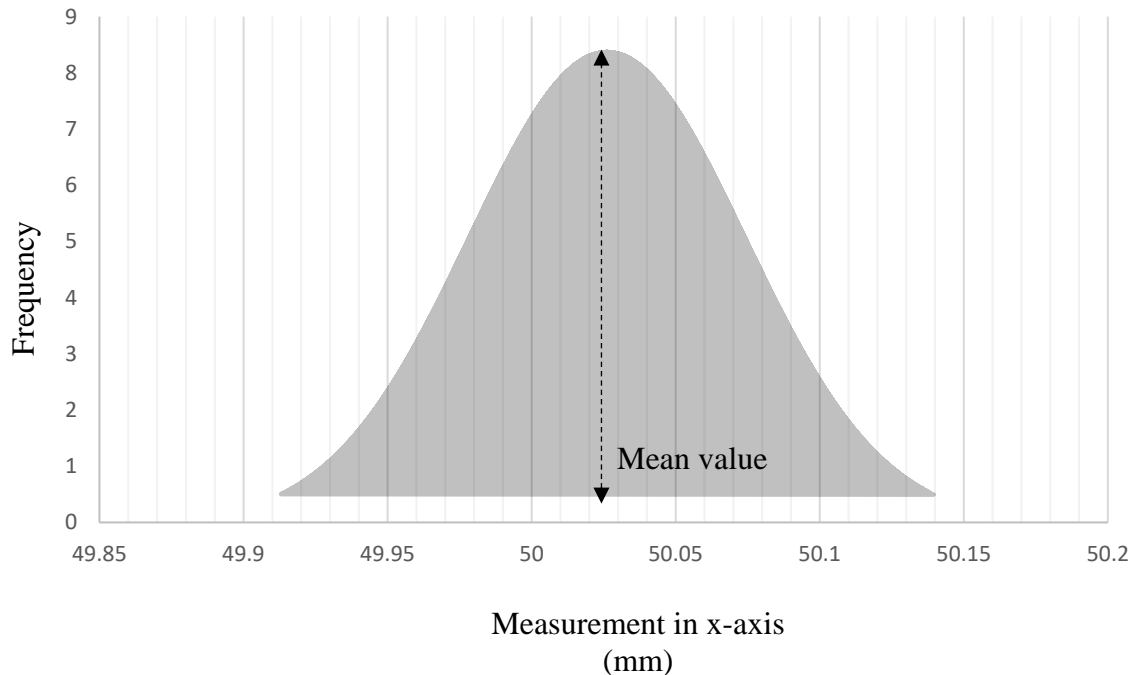
Figure 6-8: Monte Carlo simulation results of the mirror out-of-squareness when the machine is translated in the x-axis.

Table 6-5: Statistical parameters in the x-axis

Parameter (x-axis)	Value (mm)
Mean	50.026
Standard deviation	0.048
Low endpoint	49.913
High endpoint	50.140
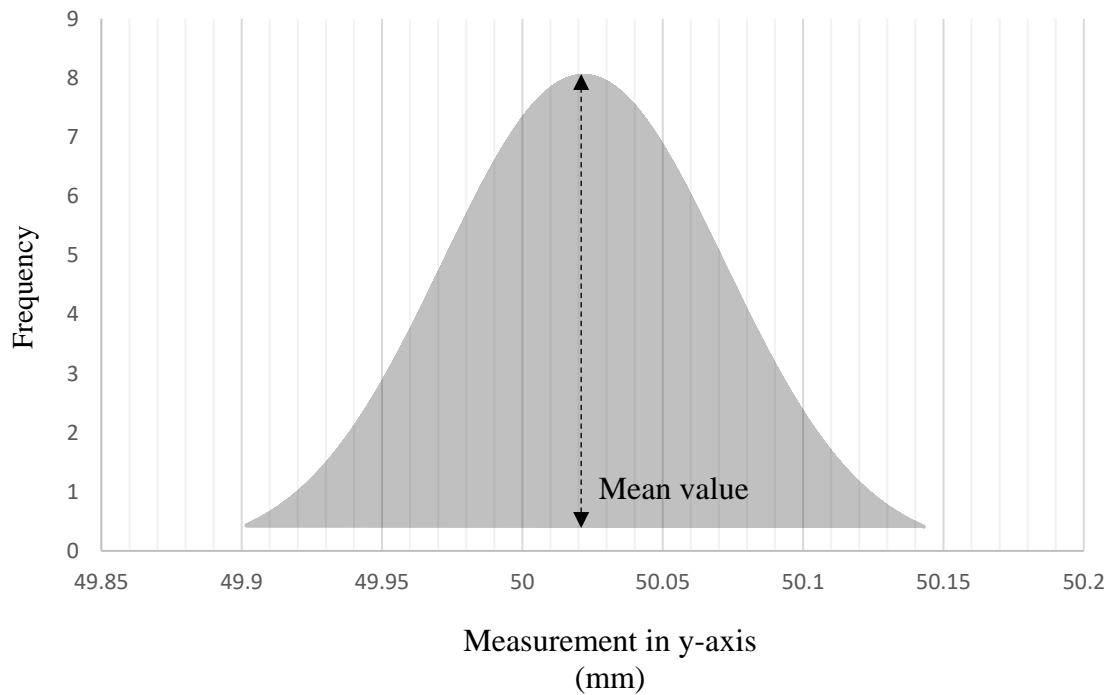
Figure 6-9: Monte Carlo simulation results of the mirror out-of-squareness when the machine is translated in the y-axis.

Table 6-6: Statistical parameters in the y-axis.

Parameter (y-axis)	Value (mm)
Mean	50.022
Standard deviation	0.050
Low endpoint	49.902
High endpoint	50.143
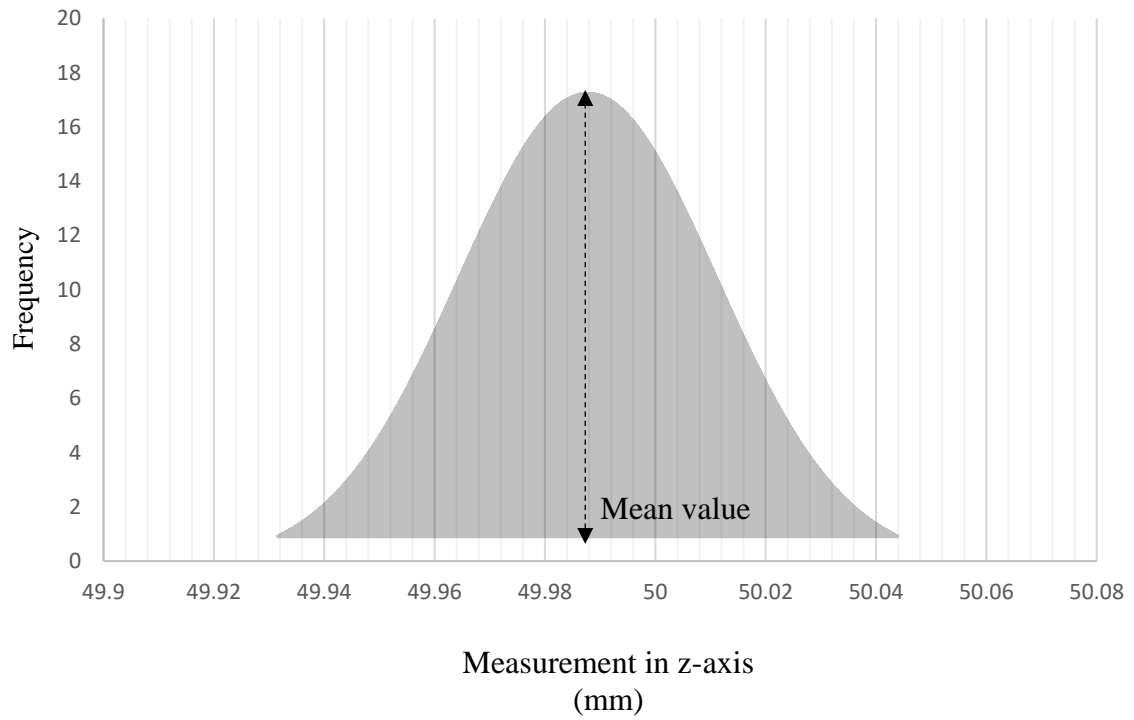
Figure 6-10: Monte Carlo simulation results of the mirror out-of-squareness when the machine is translated in the z-axis.

Table 6-7: Statistical parameters in the z-axis

Parameter (z-axis)	Value (mm)
Mean	49.988
Standard deviation	0.023
Low endpoint	49.932
High endpoint	50.044

Chapter 7:

Gauge block measurement

7. Gauge block measurements

7.1 Introduction

This chapter discusses the experimental evaluation of a novel coordinate measuring machine concept. The experiment includes the physical measurements of the workpiece from the x, y, and z-axis. The procedure for the measurements in all directions is discussed. The computation of a measurement from a sample is presented to demonstrate the use of kinematic modelling. The results are presented. Further, the repeatability of the measurement for each axis is presented. Figure 7-1 is the experimental setup.
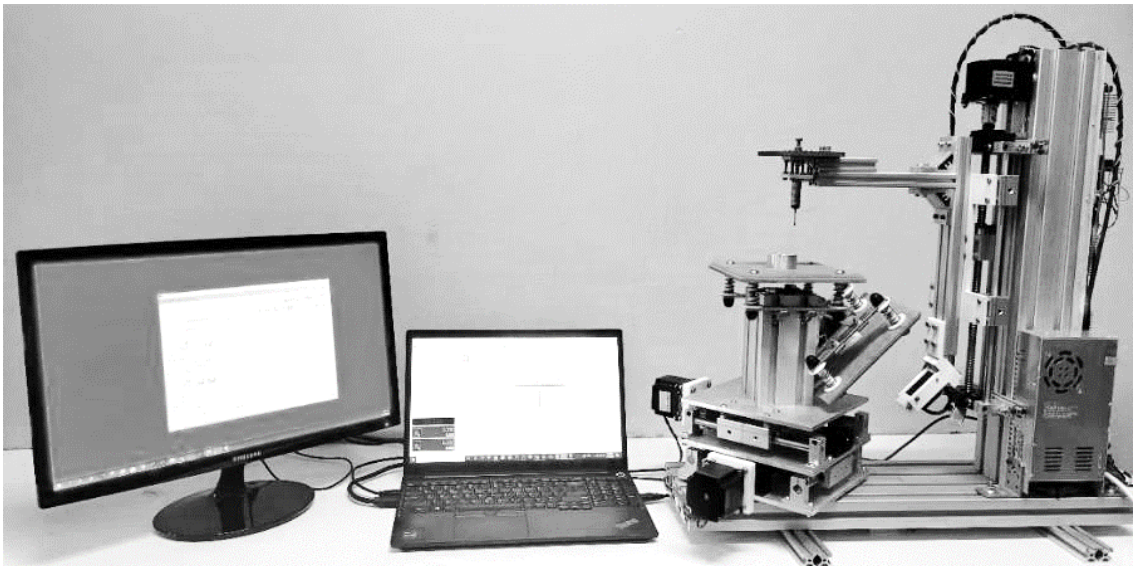
Figure 7-1: Experimental setup, computer control system.

7.2 Gauge block measurement

A novel CMM with one displacement sensor (Micro-Epsilon ILD1320-100) was calibrated with a 24 mm calibration/gauge block from Matrix-Pitter with Grade 1 measured in the x and y-axis, and an 8 mm step was measured on the z-axis. The machine used a TP20 touch-trigger probe 20 mm long with a 3 mm diameter ball. The kinematic model was employed to compute the measurements. The measurements were repeated

ten times to validate the repeatability. GRBL was used to control the machine in either direction. Where the ratio of the computer step size settings and the machine translation is 1:2.5 mm. The symbols presented below are described in section 4.3.

7.3   Measurements in x-axis

Figure 7-2 presents the measuring procedure from the x-axis showing the points of contact on the workpiece. Figure 7-3 and Figure 7-4 are physical demonstrations of the contact points when measuring in the x-axis P_{x0} (x_0, y_0, z_0) and P_{x1} (x_1, y_0, z_0) respectively. A careful preparation was performed before taking measurements, where the workpiece was manually aligned along to the x-axis, noting that a method for the misalignment presented by line P_i P_i is to be further established.
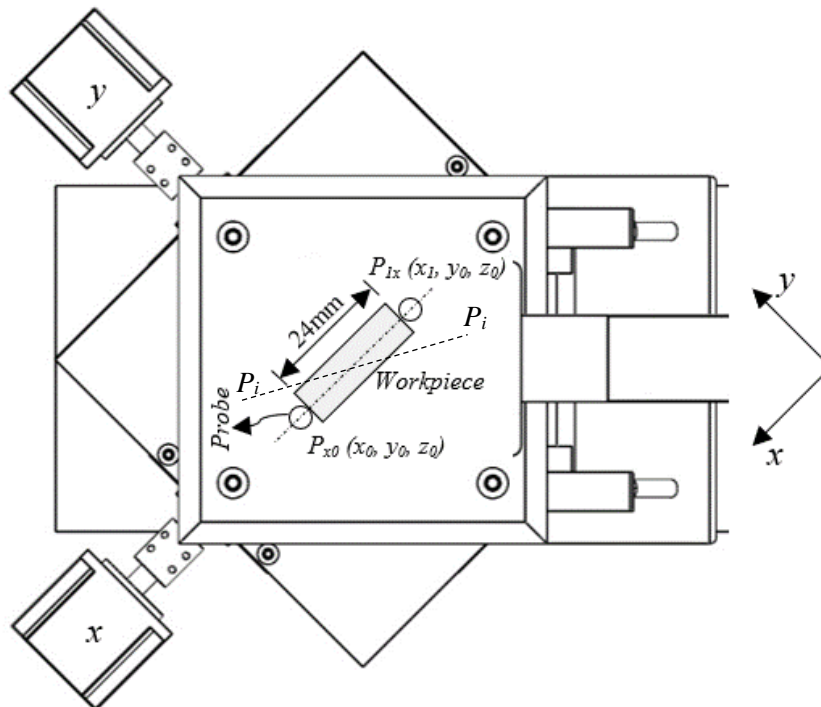
Figure 7-2: The demonstration of the measuring procedure in the x-axis.
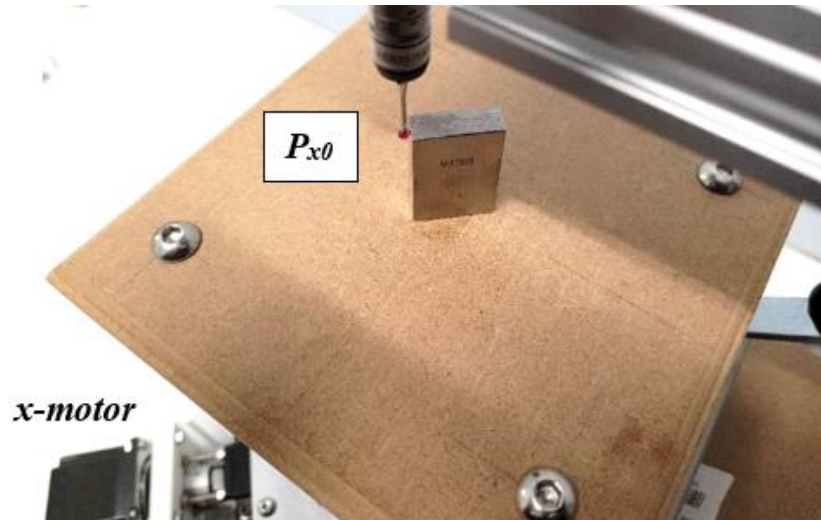
Figure 7-3: Initial position of the probe in contact at the x-axis; P_{x0} (x_0, y_0, z_0).
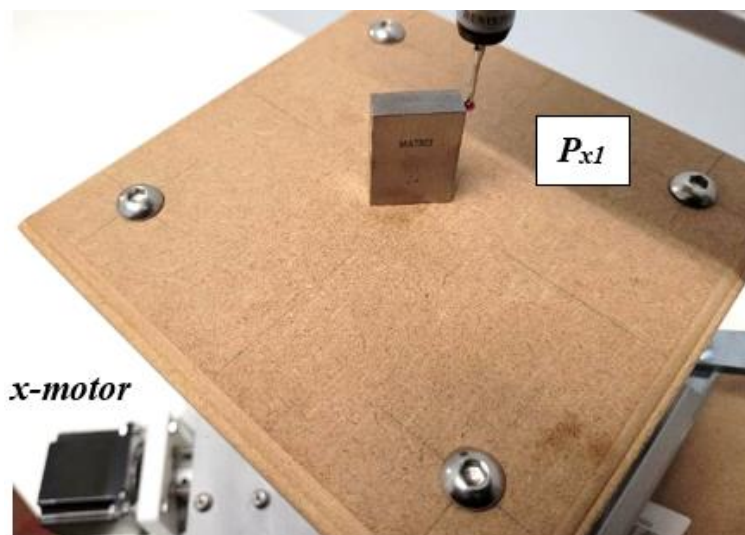
Figure 7-4: Second position of the probe contact in the x-axis: P_{x1} (x_1, y_0, z_0).

Equation 21 and equation 24 are employed respectively to calculate the probe position (P_{x0} and P_{x1}), and Δx size of the workpiece on the x-axis (see the calculation in Table 7-1).

Table 7-1: Calculation of the position and size of the workpiece in the x-axis

The probe position in the *x-axis* is calculated using equation 21

$$P_{x1} = \left(\frac{L_{0x}}{\sin\varphi} + \left((L_{0x} + L_{1x})\cos\varphi - \frac{L_{0x}}{\cos\varphi}\right)\right)\sin\theta + \frac{L_0 - L_{0x}}{\sin\alpha \cdot \cos\varphi}$$

$$P_{x1} = \left(\frac{75.723}{\sin 45} + \left(249.282 \times \cos 45 - \frac{75.723}{\cos 45}\right)\right)\sin 45 + \frac{62.215 - 75.723}{\sin 45.001 \cdot \cos 45}$$

$$P_{x1} = 128.991 \; mm$$

$$P_{x1}(128.991, 0, 0)$$

The displacement in the x-direction is calculated using equation 24

$$\Delta x = \frac{L_0 - L_{0x}}{\sin\alpha \cdot \cos\varphi} + S$$

$$\Delta x = \frac{62.219 - 75.733}{\sin 45.014 \cdot \cos 45} + 3$$

$$\Delta x = -27.016 + 3 = \mathbf{-24.016mm}$$

Table 7-2: The sampled measurements and results in the x-axis.

Samples no.	Sensor reading L_0 (mm)	α_x (°)	Sensor reading L_{0x} (mm)	Traveled distance d (mm)	Stylus diameter S (mm)	Measured distance Δx (mm)
1	62.215	45.001	75.723	-27.017	3.000	-24.017
2	62.209	45.001	75.732	-27.047	3.000	-24.047
3	62.226	45.001	75.737	-27.023	3.000	-24.023
4	62.225	45.001	75.735	-27.021	3.000	-24.021
5	62.222	45.001	75.729	-27.015	3.000	-24.015
6	62.213	45.001	75.726	-27.027	3.000	-24.027
7	62.224	45.001	75.729	-27.011	3.000	-24.011
8	62.225	45.001	75.742	-27.035	3.000	-24.035
9	62.219	45.001	75.739	-27.041	3.000	-24.041
10	62.217	45.001	75.737	-27.041	3.000	-24.041
Average	62.220	45.001	75.733	-27.028	3.000	-24.028
Standard Deviation	0.006	0.000	0.007	0.012	0.000	0.012

7.4 Measuring in the y-axis

In reference to Figure 4-7 positions, 2 and 3 are presented by P_{y0} (x_0, y_0, z_0) and P_{y1} (x_0, y_1, z_0) in Figure 7-6 respectively. Equation 22 and Equation 25 are employed to calculate the probe position (P_{y0} and P_{y1}), and Δy. See the calculation in Table 7-3.
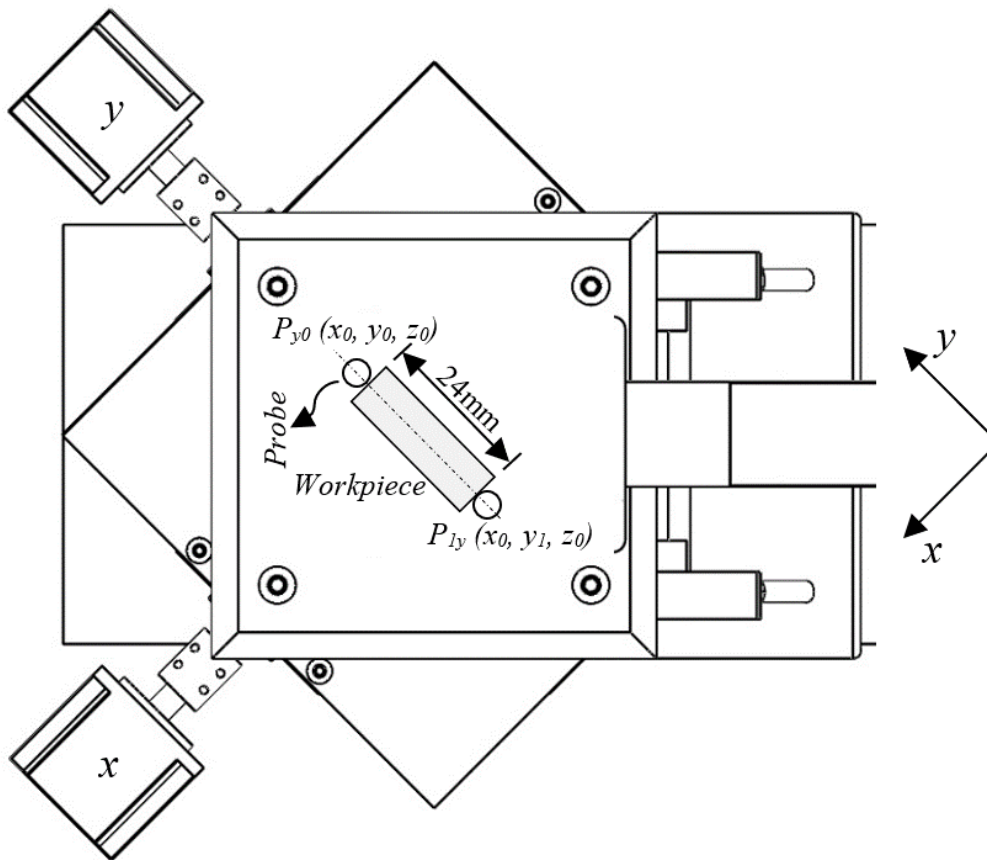
Figure 7-5: Demonstration of the measuring procedure in the y-axis.
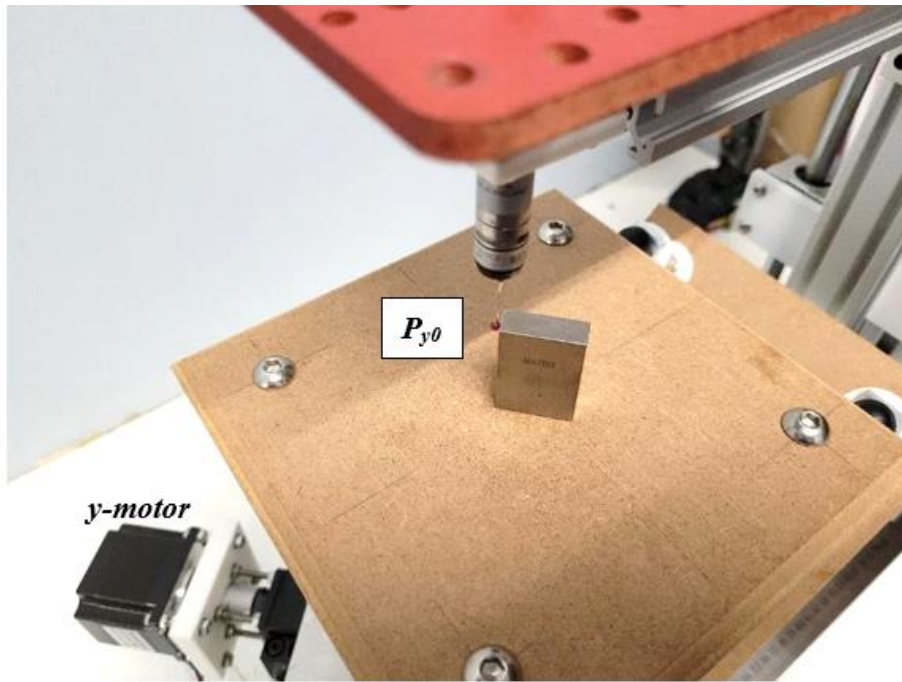
Figure 7-6: Initial position of the probe in contact at the y-axis: P_{y0} (x_0, y_0, z_0).
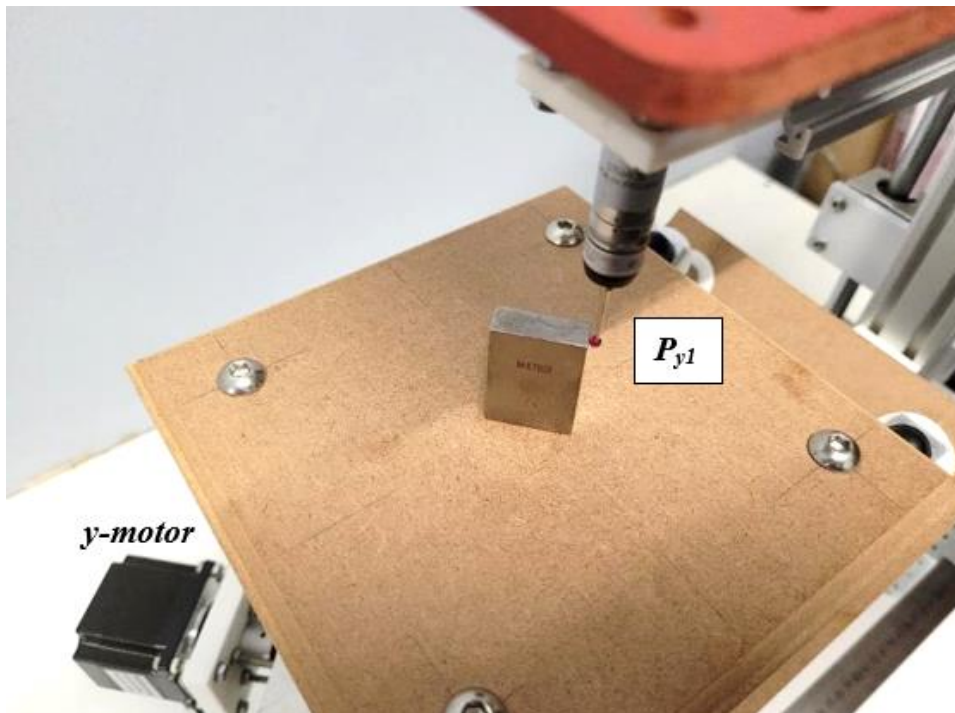
Figure 7-7: Second position of the probe in contact at the y-axis: P_{y1} (x_0, y_1, z_0).

Table 7-3: Calculation of the position and size of the workpiece in the y-axis.

The probe position in the y-*axis* is calculated using equation 22

$$P_{y1} = \left(\frac{L_{0y}}{sin\, \varphi} + \left((L_{0y} + L_{1y})cos\varphi - \frac{L_{0y}}{cos\varphi} \right) \right) sin\, \theta + \frac{L_0 - L_{0y}}{sin\, \alpha \cdot cos\varphi}$$

$$P_{y1} = \left(\frac{78.724}{sin\, 45} + \left(249.282 \times cos\varphi - \frac{78.724}{cos45} \right) \right) cos\, 45 + \frac{65.200 - 78.724}{sin\, 44.981 \cdot cos45}$$

$$P_{y1} = 130.192 \text{ mm}$$

$$P_{y1}(\ 128.991,\ 130.192, 0)$$

The displacement in the y-direction is calculated using equation 25

$$\Delta y = \frac{L_0 - L_{0y}}{sin\, \alpha \cdot cos\varphi}$$

$$\Delta y = \frac{65.200 - 78.724}{cos\, 44.981 \times cos45}$$

$$\Delta y = -27.039 \text{ mm} = -27.036 - 3 = 24.039 \text{ mm}$$

Note: To minus the diameter of the probe

Table 7-4: The sampled measurements and results in the y-axis.

Samples no.	Sensor reading L_0	α_y	Sensor reading L_{0y}	Traveled distance d	Stylus diameter S	Measured distance Δy
	(mm)	(°)	(mm)	(mm)	(mm)	(mm)
1	65.200	44.981	78.724	-27.030	3.000	-24.030
2	65.182	44.981	78.711	-27.040	3.000	-24.040
3	65.202	44.981	78.721	-27.020	3.000	-24.020
4	65.210	44.981	78.720	-27.002	3.000	-24.002
5	65.196	44.981	78.725	-27.040	3.000	-24.040
6	65.183	44.981	78.715	-27.046	3.000	-24.046
7	65.202	44.981	78.712	-27.002	3.000	-24.002
8	65.223	44.981	78.742	-27.020	3.000	-24.020
9	65.219	44.981	78.729	-27.002	3.000	-24.002
10	65.213	44.981	78.735	-27.026	3.000	-24.026
Average	65.203	44.981	78.723	-27.023	3.000	-24.023
Standard Deviation	0.013	0.000	0.009	0.016	0.000	0.012

7.5   Measuring in the z-axis

Points 7 and 9 in Figure 4-8 are represented in Figure 7-8 as P_{z0} (x_0, y_0, z_0) and P_{z1} (x_0, y_0, z_1) respectively. Equation 23 and equation 26 are employed respectively to calculate the probe position (P_{z0} and P_{z1}), and Δz the size of the workpiece in the y-axis (see the calculation in Table 7-3). Position 8 was established as the reference position for position 7, and the L_0 was calculated using equation 25.
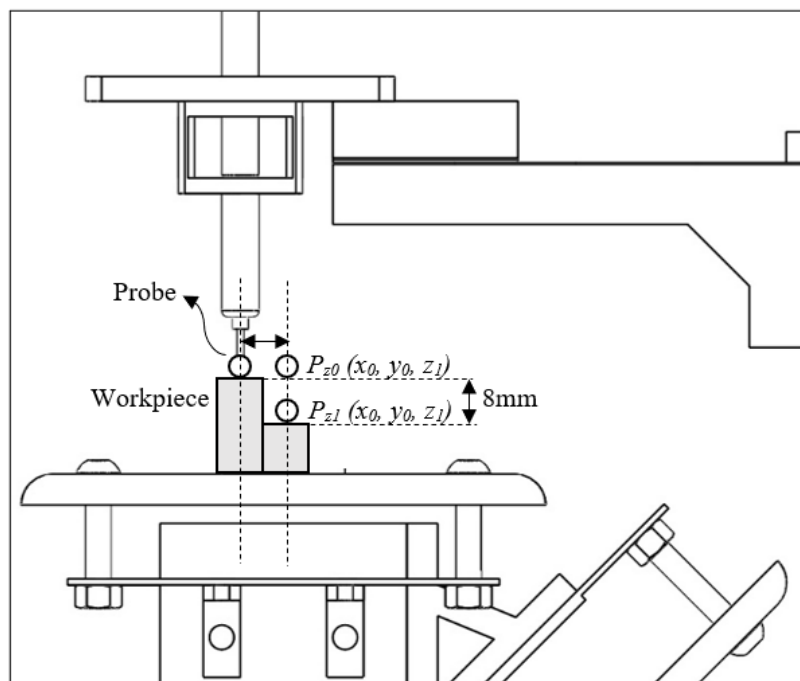
Figure 7-8: Demonstration of the measuring procedure in the z-axis.
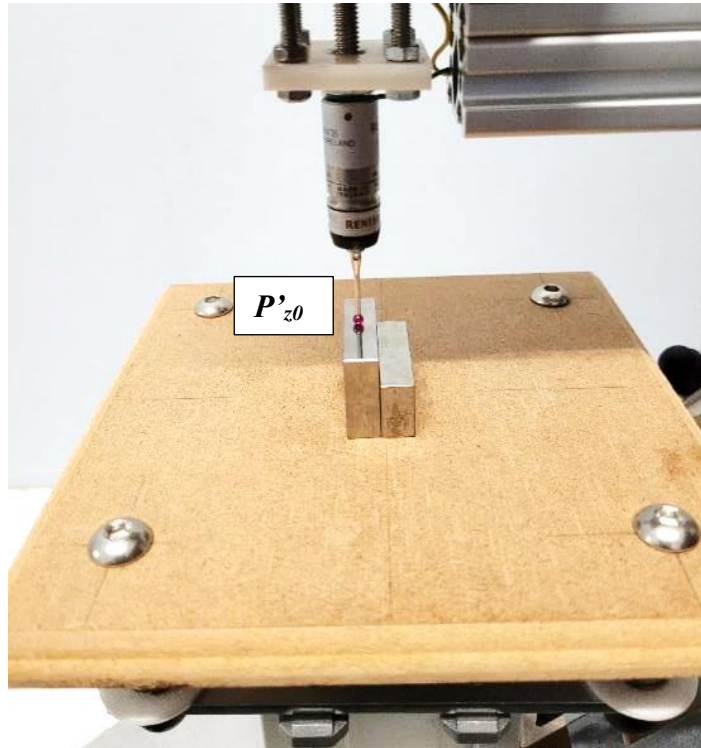
Figure 7-9: The prerequisite initial position of the probe in contact at the z-axis: P'_{z0} (x_0, y_0, z_0).
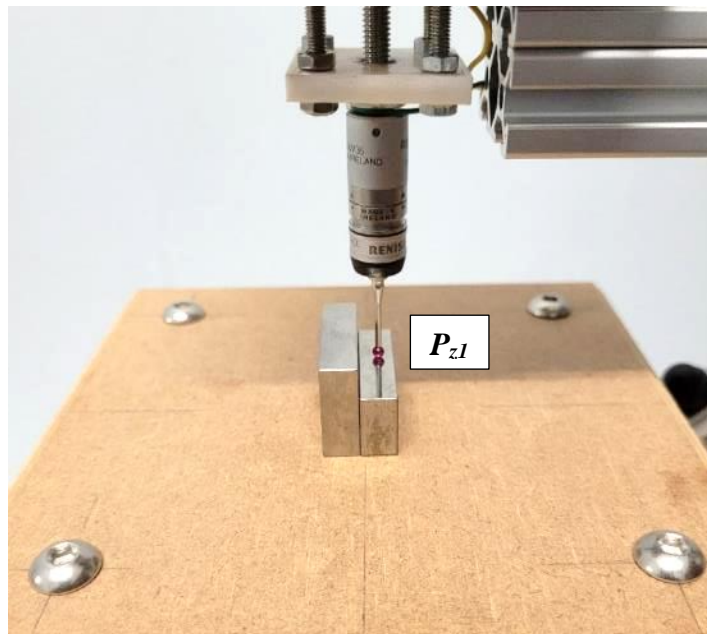
Figure 7-10: Second position of the probe in contact at the z-axis: P_{z1} (x_0, y_0, z_1).

Table 7-5: Calculation of the position and size of the workpiece in the z-axis

The probe position in the z-*axis* is calculated using equation 23

$$P_{z1} = (L_0 + L_1) \sin \varphi + \frac{L_0 - L_{1z}}{\sin \beta}$$

$$P_{z1} = 249.282 \sin 4\,5 + \frac{79.046 - 84.753}{\sin 4\,5.007}$$

$$P_{z1} = 168.199 \text{ mm}$$

$$P_{z1}(\ 128.991,\ 130.192\ ,168.199)$$

The displacement in the z-direction is calculated using equation 26

$$\Delta z = \frac{L_0 - L_{1z}}{\sin \beta}$$

$$\Delta z = \frac{79.046 - 84.753}{\sin 4\,5.007}$$

$$\Delta z = -8.069 \text{ mm}$$

Table 7-6: The sampled measurements and results in the z-axis.

Samples no.	Sensor reading L_0 (mm)	α_z (degrees)	Sensor reading L_{0z} (mm)	Measured distance Δz (mm)
1	79.046	45.007	84.753	-8.072
2	79.047	45.007	84.734	-8.043
3	79.049	45.007	84.732	-8.038
4	79.043	45.007	84.731	-8.045
5	79.052	45.007	84.732	-8.033
6	79.060	45.007	84.719	-8.004
7	79.048	45.007	84.750	-8.065
8	79.049	45.007	84.732	-8.038
9	79.044	45.007	84.733	-8.046
10	79.032	45.007	84.730	-8.059
Average	79.047	45.007	84.735	-8.044
Standard Deviation	0.007	0.000	0.009	0.018

7.6   Comparison Results with conventional CMM

The proposed novel CMM was further compared with the conventional DEA CMM to measure the width of the 6 mm slot and 40.9 mm diameter of a Halcon Gauge, see Figure 7-11.
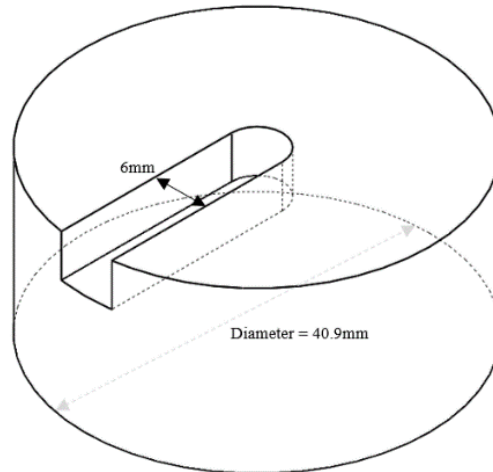
Figure 7-11: Drawing of Halcon Gauge.

The setup measurement for the novel CMM included placing the Halcon Gauge on the mirror table as presented in Figure 7-12.
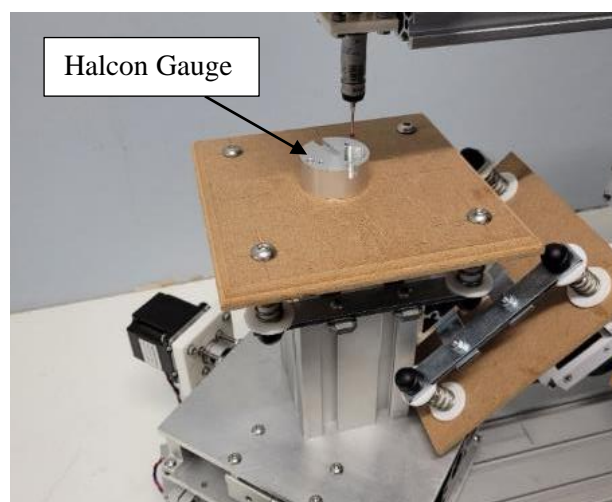
Figure 7-12: The Halcon Gauge for results comparison

The manipulation system was maneuvered to have the centre of the probe inside the slot and below the top surface of the Halcon Gauge. The probe was moved to be in contact of both the vertical opposite sides of the slot and the distance was calculated to determine the size of the slot. The amount of force applied during the contact was negligible to have displaced the workpiece. The diameter was also measured by probing the opposite sides of the workpiece and calculated the distance in between. The results are presented in Table 7-7.

The measurement setup with the conventional DEA CMM included placing the Halcon Gauge on the workspace, see Figure 7-13. The machine was manually moved with the joystick to have the probe in contact with the Halcon Gauge. The probe was placed in between the slot and contacted the vertical sides of the slot, and the distance was calculated. Also, with the measurements of the diameter the probe was caused to make contact of the opposite sides of the circumference of the Halcon Gauge. Table 7-7 presents the results obtained, Appendix F provides detailed drawings of the Halcon Gauge and the measurement results of DEA CMM.
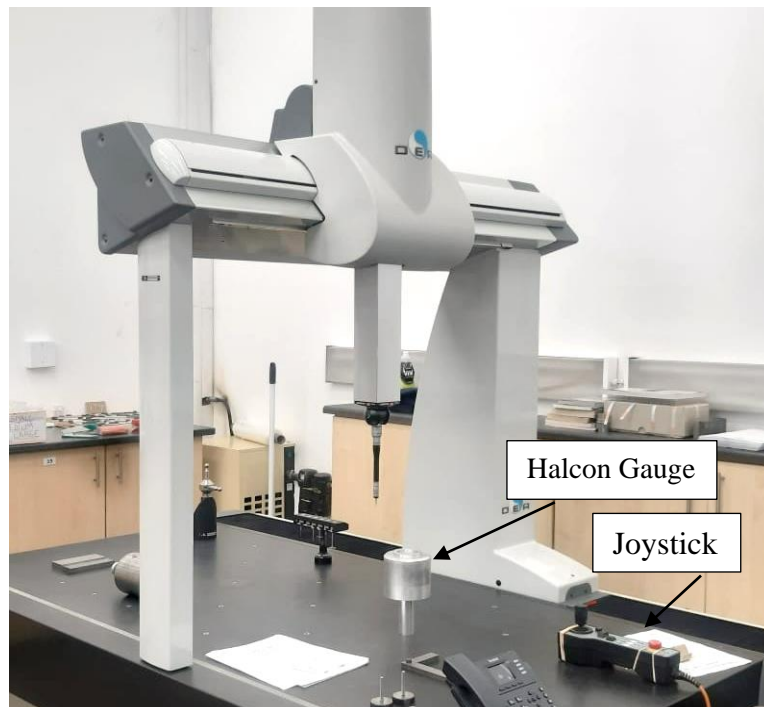
Figure 7-13: DEA CMM machine, for comparison of the results.

Table 7-7: Comparison results of the novel CMM and the DEA CMM.

Workpiece dimensions	Design sizes of the workpiece (*mm*)	Novel CMM Measured Sizes (*mm*)	DEA CMM Measured Sizes (*mm*)
Diameter	40.900	40.886	40.904
Slot Size	6.000	5.980	6.005

Chapter 8:

Conclusions and recommendations

8. Conclusions and recommendations

8.1 Conclusions

This thesis introduced a novel metrological approach aimed at providing a solution to the accuracy demand and precision requirements brought on by the current rapid development of MEMs. It presents an initiative to lower the cost of manufacturing the machine by reducing the number of measuring displacement sensors from three to one, whilst complying with the Abbe principle.

The study described the novelty of the workpiece supported by the mirror table which is translated into the x and y-axis by the manipulation system. The mirror is positioned at 45^0 to the vertical axis of the mirror table, and each plane surface of the coordinate system. The displacement sensor is mounted at 45° at the lower end of the vertical member of the metrology frame while the probe is fixed at the horizontal end. The functional line (laser beam) of the displacement sensor is always fixed to the tip of the probe. This configuration allows the alignment to be maintained and fulfil Abbe's fundamental requirements in all translations of the machine in a global coordinate system. The mirror is perpendicular and always intersects the laser beam at a gap distance between the displacement sensor and the probe.

The design of the novel CMM machine considers the conceptual bases of the ultra-precision CMM. The aim is to demonstrate a possible solution to achieve a small positioning or measure uncertainty at a low cost. The design applies Abbe's principle, mirror out-of-squareness and flatness, the geometric errors, as the fundamental basis to achieve high positioning accuracy. Also, the metrology frame and structural frame of the novel design is to be separated to allow for optimising the design. The metrology system contains the probe system and displacement sensor attached to the metrology frame. Using the displacement sensor, the position of the three-translation axis of the mirror table is measured.

To satisfy the Abbe principle, the metrology frame consists of the probe attached to the cantilever end of the frame and the displacement sensor attached to the lower end of the frame with a laser beam pointing directly to the ball of the probe. Both measuring systems are attached to a common metrology frame and translated at the same time. The probe position is identified after every movement by working out the kinematic model in a specified direction and knowing the distance between the displacement sensor and the mirror. The solution to the kinematics problem defines the coordinates of the probe.

GRLB was employed as the motion control system that allows the user to manipulate the translation of the axis to a certain position of π on the probe. The GRBL firmware was installed on an Arduino-Uno for input and output motion control. An ILD1320-100 Laser-optical displacement sensor from Micro-Epsilon was used to acquire the distance between the displacement sensor and the mirror.

The design assumed the displacement sensor as a fixed component and the mirror as an adjustable component. The calibration method is based on the fundamentals of trigonometric special triangles of 45° as presented. This technique was suggested by the nature of the optical triangles formed by the mirror and the laser beam of the displacement sensor. Change to either side due to machine translation suggests the new equal values on the equal sides of the triangle. Therefore, knowing the initial value of the laser beam measurement and the travel distance of the laser pointers across the mirror, the value of the new laser beam measurement can be predicted. Therefore, during the calibration, the theoretical value can be compared with the measured value, and the difference in the two values suggests the out-of-squareness of the mirror.

The mirror out-of-squareness results were verified numerically. The Monte Carlo method was employed to reproduce the results. A set of experiments was carried out to characterize the novel CMM and to practically confirm the validity of the proposed system model. The machine was employed to measure calibration/gauge block from Matrix-Pitter with Grade 1.

The experimental results show that the kinematic model is relevant in establishing the position of the probe in the global coordinate system. With a standard deviation of 0.012,

0.016, and 0.018 mm on the x, y, and z-axis, respectively. The novel design was further employed to measure a Halcon Gauge as presented. The results obtained were compared with the results obtained from Executive Engineering Company (see Appendix F), where the measurements were performed using a conventional bridge-type DEA CMM machine (see Figure 7-13).

8.2 Recommendations

To improve the novel design and the measuring performance, the study recommends the following to subjects to be addressed.

- Use a mirror remote interferometer and a mirror with accurate flatness.

- Design a manipulation system with high precision.

- Automate the calibration of the mirror.

- Develop a user-friendly interface for the measurement and movement system.

- Design a computer control system, e.g., using MATLAB, Python, etc.

- Enhance the stiffness and structure optimization.

- Improve the displacement sensor position to be 45º on all sides of the coordinate system.

- Change the structure to accommodate thermal error compensation.

- Conduct a comprehensive kinematics calibration model and error compensation study.

- Develop a comprehensive error modelling of the machine.

- Develop a dynamic error modelling.

- Determine the dynamic errors of the machine.

References

[1] British Standard ISO 5725-1:1994, Accuracy (trueness and precision) of measurement methods and results, New York: BSI, 1994.

[2] N. Raghavendra and L. Krishnamurthy, Engineering Metrology and Measurements, India: Oxford University Press 2013, 2013.

[3] D. Flank and J. Hannaford, Fundamental Good practice in Dimensional Metrology, Teddington: National Physical Laboratory, 2012.

[4] R. Leach, K. Leuven and M. Ferrucci, "Dimensional Metrology," *The International for production Engineering,* p. 1, 2020.

[5] V. R. Meyer, J. Pfohl and B. Winter, "Calibration, handling repeatability, and the Maximum," *Accred Qual Assur,* vol. 15, pp. 705-708, 2010.

[6] International Vocabulary of Metrology – 200:2012, JCGM, *Basic and General Concepts and Associated Terms (VIM),* 2008.

[7] International Vocabulary of Metrology – OIML V 2-200, *Basic and General Concepts and Associated Terms (VIM),* 2007.

[8] A. Chrysochoos and Y. Surrel, Basic elements of metrology and introduction to the various tehcniques, HAL, 2019.

[9] S. H. Ali, "Probing System Characteristics in Coordinate Metrology," *Measurement Science Review,* vol. 10, no. 4, pp. 120 - 129, 2018.

[10] CIM, "metrology-glossary," ECM global measurement solution, 25 February 2022. [Online]. Available: https://eastcoastmetrology.com/resources/metrology-glossary/. [Accessed 01 March 2022].

[11] B. Hess, "What-is-reverse-engineering," Astro Machine Works, 09 September 2019. [Online]. Available: https://astromachineworks.com/what-is-reverse-engineering/. [Accessed 01 March 2022].

[12] F. Yetai, S. Ping, C. Xiaohuai, H. Qiangxian and Y. Liandong, "The analysis and complementarity of abbe Principle application limited in coordinate measurement," in *Proceedings of the world congress on engineering, 2010, Vol 3*, London, U.K, 2010.

[13] R. Leach, Fundamental Principles of Engineering Nanometrology, San Diego, USA: William Andrew, 2014.

[14] J. R. Hocker and P. H. Pereira, Coordinate Measuring Machine and Systems, United States of America: Taylor & Francis Group, 2012.

[15] A. C. Majarena, J. Santolaria, D. Samper and J. J. Aguilar, "An Overview of Kinematic and Calibration Models Using Internal/External Sensors or Constraints to Improve the Behavior of Spatial Parallel Mechanisms," *sonsors,* vol. 10, pp. 10256 - 10297, 2010.

[16] K. J. Waldron and G. L. Kinzel, Kinematic Dynamics, and Design of Machinery, United States of America: john Wiley & Sons, Inc, 2004.

[17] S. Kucuk and Z. Bingul, "Robot Kinematic: Forward and Inverse Kinematics," *researchgate,* pp. 117 - 147, 2006.

[18] F. Pan, L. Nie, Y. Bai, X. Wang, K. Liu and X. Wu, "Error compensation for Coordinate Measuring Machine," in *IOP Conf. Series: Materials Science and Engineering 394 (2018) 032068*, 2018.

[19] S. H. Mian and A. Al-Ahmari, "New developments in coordinate measuring machines," *Int. J. Metrol. Qual,* vol. 5, no. 1, pp. 101p1 - 101p7, 2014.

[20] V. K. Seggelen, NanoCMM: a 3D Coordinate Measuring Machine with low moving mass for measuring small products in array with nanometer uncertainty, Eindhoven: Technishe University, 2007.

[21] Y. Cheng, Z. Wang, X. Chen, Y. Li, H. Li and H. Wang, "Evaluation and Optimization of Task-oriented Measurement Uncertainty for Coordinate Measuring Machines Based on Geometrical Product Specifications," *Applied Science,* vol. 9, no. 6, pp. 1 - 22, 2018.

[22] "The History of Coordinate Measuring Machines," CMMXYZ, 04 September 2020. [Online]. Available: https://blog.cmmxyz.com/blog/the-history-of-coordinate-measuring-machines. [Accessed 02 March 2021].

[23] W. E. Singhose and W. P. Seering, "The Effect of Input Shaping on Coordinate Measuring Machine Repeatability," in *IFToMM World Congress on the Theory of Machines and Mechanisms*, Massachusetts Institute of Technology, 1995.

[24] R. R. Nikam, "Coordinate measuring machine (CMM)," *International Journal of Mechanical and Industrial Technology,* vol. 6, no. 2, pp. 13 - 19, 2019.

[25] "Different types of CMM and how the are used," Winn machine, 16 February 2021. [Online]. Available: https://winnmachine.com/2021/02/16/different-types-of-cmm-and-how-they-are-used/. [Accessed 03 March 2022].

[26] M. R. Mantel, Coordinate Measuring Machine; A Modern Inspection Tool in Manufacturing, New Jersey Institute of Technology: Thease, Public Health, 1993.

[27] K. Dhoska, Measurement Methods with 3D Coordinate Measuring Machine ans Improve Characterization Setup for Detector Performance, Thesis,Tallinn University of Technology, 2016.

[28] S.-C. Toguem, A. Vissiere, M. Damak, C. Mehdi-Souzani, N. Anwer and H. Nouira, "Design of an ultra-high precision machine for form measurement," *CIRP Design,* vol. 84, pp. 942 - 947, 2019.

[29] A. M. Rugbani, The Design, Kinematics and Error Modelling of a Novel Micro-CMM Parallel Manipulator, Cape Town: Stellembosch University, 2014.

[30] T. Kiyoshi, H. Masahiko, E. Kazuhiro and O. Shigeo, "Development of Nano-CMM and Parallel-CMM CMM in the 21th Century," in *International Dimensional Metrology Workshop*, Tokyo, Japan, 1999.

[31] A. Rugbani and K. Schreve, "The use of parallel mechanism micro-CMM in micrometrology," in *4th Robotics and Mechatronics Conference of South Africa*, Pretoria, South Africa, 2011.

[32] A. Rugbani and K. Schreve, "The kinematics and error modelling of a novel micro-CMM," *The International Journal of Advanced Manufacturing Technology,* vol. 78, pp. 961-969, 2015.

[33] S. Hammad Mian and A. Al-Ahmari, "New developments in coordinate measuring machines for manufacturing industries," *International Journal of Metrology and Quality Engineering,* vol. 5, no. 1, p. 101, 2014.

[34] G. Hermann, "Geometric Error Correction in Coordinate Measurement," *Acta Polytechnica Hungarica,* vol. 4, no. 1, pp. 47 - 62, 2007.

[35] Q. Huang, K. Wu, C. Wang, R. Li, K. C. Fan and Y. Fei, "Development of an Abbe Error Free Micro Coordinate Measuring Machine," *Applied Science,* vol. 6, no. 97, pp. 1-12, 2016.

[36] P. Yang, T. Takamura, S. Takahashi, S. Takamasu, O. Sato, S. Osawa and T. Takatsuji, "Development of high-precision micro-coordinate measuring machine: Multi-probe measurement system for measuring yaw and straight motion error of XY linear stage," *elsevier,* vol. 35, no. 3, pp. 424-430, 2011.

[37] J. A. Kramar, "Nanometre resolution metrology with the molecular measurement machine," *Measurement Science and Technology,* vol. 16, no. 11, pp. 2121 - 2128, 2005.

[38] E. C. Bos, F. M. Delbressine, H. Haitjema and K. Leuven, "High-accuracy CMM metrology for micro systems," *reasechgate,* January 2004.

[39] R. Thalmann, F. Meli and A. Kung, "State of the art of tactile micro coordinate metrology," *Applied Science,* vol. 6, no. 150, pp. 1 - 13, 2016.

[40] S. Cao, U. Brand, T. Kleine-Besten, W. Hoffmann, H. Schwenke, S. Butefisch and S. Buttgenbach, "Recent developments in dimensional metrology for microsystem components," *Microsystem Technology,* vol. 8, no. 1, pp. 3 - 6, 2002.

[41] S. P. C. X. H. Q. a. Y. L. Fei Yetai, "The Analysis and Complementarity of Abbe Principle Application Limited in Coordinate Measurement," in *World Congress on Engineering 2010 Vol III*, London, UK, 2010.

[42] T. T. S. K. O. S. S. O. T. T. P.Yang, "Development of high-precision micro-coordinate measuring machine: Multi-probe measurement system for measuring yaw and straight motion error of XY linear stage," *elsevier,* vol. 35, no. 3, pp. 424-430, 2011.

[43] K. W. C. W. R. L. K.-C. F. a. Y. F. Q. Huang, "Development of an Abbe Error Free Micro Coordinate Measuring Machine," *Applied Science,* vol. 6, no. 97, pp. 1-12, 2016.

[44] F. Yetai, S. Ping, C. Xiaohuai, H. Qiangxian and Y. Liandong, "The Analysis and Complementarity of Abbe Principle Application Limited in Coordinate Measurement," in *World Congress on Engineering 2010 Vol III*, London, UK, 2010.

[45] a. W. W.E.Singhose, "The Effect of Input Shaping on Coordinate Measuring Machine Repeatability," in *IFToMM World Congress on the Theory of Machines and Mechanisms*, Massachusetts Institute of Technology, 1995.

[46] G. N. Peggs, A. J. Lewis and S. Oldfield, "Design for a Compact High-Accuracy CMM," *Annals of the CIRP,* vol. 48, no. 1, pp. 417 - 420, 1999.

[47] M. Vermeulen, High-precision 3D-Coordinate measuring machine: design and prototype-development, Eindhoven: Technische Universiteit Eindhoven, 1999.

[48] T. A. Ruijl and J. van Eijk, "A novel ultra precision CMM based on fundamental design principles," in *Proceedings of the ASPE topical meeting on Coordinate Measuring Machines*, Delft, 2003.

[49] I. Widdershoven, R. Donker and H. A. Spaan, "Realization and calibration of the "Isara 400" ultra-precision CMM," in *13th International Conference on Metrology and Properties of Engineering Surfaces*, Eindhoven, Netherlands, 2011.

[50] K. C. Fan, Y. T. Fei, X. F. Yu, Y. J. Chen, W. L. Weng, F. Chen and Y. S. Liu, "Development of a low-cost micro-CMM for 3-D micro/nano measurements," *Measurement science and technology,* vol. 17, no. 3, pp. 524 - 532, 2005.

[51] K.-C. Fan and W. Wang, "The Structure Design of a Micro-precision CMM with Abbé Principle," *ResearchGate,* pp. 297 - 300, 2007.

[52] J. Brayn, "International Status of Thermal Error Research," *CIRP Annals,* vol. 39, no. 2, pp. 645 - 656, 1990.

[53] T. Ruijl, Ultra Precision Coordinate measuring Machine: Design, calibration and error Compensation, Delft: Thesis, TU Delft, 2001.

[54] J. B. Brayn, "The Abbe Principle Revisited: An Updated Interpretation," *Precision Engineering,* vol. 1, no. 3, pp. 129-132, 1979.

[55] G. Ren, X. Qu and X. Chen, "Performance Evaluation and Compensation Method of Trigger Probes in Measurement Based on the Abbe Principle," *MDPI Sensors,* vol. 20, no. 2413, pp. 1 - 13, 2020.

[56] G. X. Zhang, "A Study on the Abbe Principle and Abbe Error," *CIRP Annals,* vol. 38, no. 1, pp. 525 - 528, 1989.

[57] H. Nouira, J. A. Salgado, N. El-Hayek, S. Ducourtieux, A. Delvallee and N. Anwer, "Setup of a high precision profilometer and comparison of tactile and optical measurement of standard," *Measurement Science and Technology,* vol. 25, no. 4, 2014.

[58] S. Moylan, D. Hong, B. N. Damazo, J. Soons and A. Donmez, "Development of a metrology frame to improve the positioning accuracy of Micro/Meso-scale Machine Tools," *International Journal of Mechatronics and Manufacturing Systems,* vol. 2, no. 5/6, pp. 600 - 619, 2009.

[59] A. Vissiere, H. Nouira, M. Damak, O. Gibaru and J. M. David, "Concept and architecture of a new apparatus for cylindrical form measurement with a nanometric level of accuracy," *Measurement Science and Technology,* vol. 23, no. 9, pp. 1 - 9, 2012.

[60] J. B. Bryan , "Design and contrcution of an ultraprecision 84 inch diamonf turning machine," *Precision engineering ,* vol. 1, no. 1, pp. 13 - 17, 1979.

[61] W. G. Weeker, "Compensation for dynamic errors of coordinate measuring machine," Technische Universiteit Eindhoven, Eindhoven, Netherlands, 1996.

[62] Z. Pandilov and V. Dukovski, "Survey of the Dominant Error Types at Parallel Kinematics Machine Tools," *Annals of Fuculty Engineering Hunedoara-International Journal of Engineering,* no. 1, pp. 1584 - 2665, 2010.

[63] Rugbani, Ali; Schreve, Kristiaan;, "Modelling and analysis of the geometrical errors of a parallel manipulator micro-CMM," in *Precision Assembly Technologies and Systems: International Precision Assembly Seminar, IPAS 2012*, Chamonix, Springer Berlin Heidelberg, 2012, pp. 105-117.

[64] Z. Yu, L. Tieminb and T. Xiaoqiang, "Geometric Error Modeling of Machine Tools Based on Screw Theory," in *International Conference on Advances in Engineering*, Beijing, China, 2011.

[65] W. A. Khan and W. Chena, "Correlation between linear and angular kinematic errors in prismatic joint of machine tools," in *The International Society for Optical Engineering*, Beijing 100191, P. R. China., 2009.

[66] J. Wang and J. Guo, "Geometric error identification algorithm of numerical control machine tool using a laser tracker," *proceedings of the Institution of Mechanical Engineers, Part B: Journal of Engineering Manufacture,* vol. 230, no. 11, pp. 2004 - 2015, 2016.

[67] G. Hermann, "Geometric Error Correction coordinate Measurement," *Acta Polytechnica Hungarica,* vol. 4, no. 1, pp. 47 - 62, 2007.

[68] X. Wei, Z. Su, X. Yang, Z. Lv, Z. Yang, H. Zhang, X. Li and F. Fang, "A Novel Method for the Measurement of Geometric Errors in the Linear Motion of CNC Machine Tools," *Applied Science (MDPI),* vol. 9, no. 3357, pp. 1 - 11, 2019.

[69] H. Liu, H. Xiang, J. Chen and R. Yang, "Measurement and compensation of machine tool geometry error based on Abbe principle," *The International Journal of Advanced Manufacturing Technology,* 2018.

[70] J. Loh, J. McBride, M. Hill and D. Zhang, "Analysis of linear and angular errors of a small coordinate measuring machine (SCMM)," *Transactions on Engineering Sciences,* vol. 44, no. 6, pp. 245 - 255, 2003.

[71] L. Guiqiang, J. Zhang and Z. Feifai, "Geometric Error Modeling of a Vertical Machining Center," *Advanced Materials Research,* Vols. 694-697 , pp. 1842-1845, 2013.

[72] N. A. Barakat, A. D. Spence and M. A. Elbestawi, "Adaptive Compensation of Quasi-Static Error for an Intrinsic Machine," *International Journal of Machine Tools and Manufacture,* vol. 40, no. 15, pp. 2267 - 2291, 2000.

[73] A. C. Okafor and Y. M. Ertekin, "Derivation of Machine Tool Error Models and Error Compensation Procedure for Three Axes Vertical Machining Center Using Rigid Body Kinematics," *Internationaal Journal of Machine Tool and Manufacture,* vol. 40, no. 8, pp. 1199 - 1213, 2000.

[74] T. -C. Chen, C. -J. Chang, J. -P. Hung, R. -M. Lee and C. -C. Wang, "Real-time compensation for thermal errors of the milling machine," *Applied Science,* vol. 6, no. 4, 2016.

[75] M. O. Dos Santos, G. F. Batalha, E. C. Bordinassi and G. F. Miori, "Numerical and experimental modeling of thermal errors in a five-axis CNC machining center," *The International Journal of Advanced Manufacturing Technology,* vol. 96, no. (5 - 8), pp. 2619 - 2642, 2018.

[76] L. Weng, W. Gao, Z. Lv, T. Liu, Y. Wang, X. Qi and Y. Tian, "Influence of external heat sources on volumetric thermal errors of precision machine tools," *The International Journal of Advanced Manufacturing Technology,* pp. 475 - 495, 2018.

[77] J. P. Allen, S. R. Postlethwaite and D. G. Ford, "Practical application of thermal error correction - 4 case studies," *Transactions on Engineering Sciences,* vol. 16, pp. 1743 - 3533, 1997.

[78] J. Yang, J. Yuan and J. Ni, "Thermal error mode analysis and robust modeling for error compensation on a CNC turning center," *International Journal of Machine Tools & Manufacture,* vol. 39, pp. 1367 - 1381, 1999.

[79] J. S. Chen, J. Yuan and J. Ni, "Thermal error modelling for real-time error compensation," *The International Journal of Advanced manufacturing Technology,* vol. 12, pp. 266 - 275, 1996.

[80] M. Putz, J. Regel, A. Wenzel and M. Braunig, "Thermal errors in milling: Comparison of displacement of the machine tootl, tool and workpiece," in *17th CIRP Conference on Modelling of Machining Operations*, Chemnitz, Germany, 2019.

[81] T. -j. Li, C. -y. Zhao and Y. -m. Zhang, "Prediction method of thermal errors of the screw system in lathes based on moving thermal network," *Precision Engineering,* vol. 59, pp. 166 - 173, 2019.

[82] J. Yang, D. Zhang, B. Feng, X. Mei and Z. Hu, "Thermal-Induced Errors Prediction and Compensation for a Coordinate Boring Machine Based on Time Series Analysis," *Mathematical Problems in Engineering,* pp. 1 - 13, 2014.

[83] W. G. Weekers and P. H. Schellekens, "Assessment of Dynamic Errors of CMMs for Fast Probing," *Annals of the CIRP,* vol. 44, no. 1, pp. 469 - 474, 1995.

[84] C. Dong, C. Zhang and B. Wang, "Prediction and Compensation of Dynamic Errors for Coordinate Measuring Machines," *Journal of Manufacturing Science and Engineering,* vol. 124, pp. 509 - 514, 2002.

[85] C. Yanling, P. Yuning and W. Zhonghai, "FEM Study on the dynamic effects of CMM geometric errors," *Advanced Materials Research,* Vols. 605-607, pp. 972 - 975, 2013.

[86] A. Keck, O. Sawodny, M. Gronle, T. Haist and W. Osten, "Active compensation of dynamic errors in a coordinate measuring machine," vol. 49, no. 21, pp. 636 - 641, 2016.

[87] Y. Echerfaoui, A. El Ouafi and A. Chebak, "Experimental investigation of dynamic error in coorninate measuring machine for high speed measurement," *International Journal of Precision Engineering and Manufacturing,* vol. 19, no. 8, pp. 1115 - 1124, 2018.

[88] Z. Pandilov, "Dominant Types of Errors at Parallel Kinematics Machine Tools," *FME Transactions,* vol. 45, pp. 491 - 495, 2017.

[89] M. Jiang, L. Jiang, D. Jiang, J. Xiong, J. Shen, S. H. Ahmed and H. Song, "Dynamic measurement error prediction for sensors based on frirefly algorithm optimize support vector machine," *Sustainable cities and Scociety,* vol. 35, pp. 250 - 256, 2017.

[90] D. Yuan, X. Tao, C. Xie, H. Zhao, D. Ren and X. Zhu, "Calibration and compensation of dynamic abbe error of coordinate meachuring machine," *Journal of Dynamic System,* vol. 140, no. 5, 2017.

[91] M. Karun, "A Comparison of Mechanical Artefacts used in Calibration of Coordinate Measuring Machines (CMMs)," *AMSE JOURNALS-AMSE IIETA publication-2017-Series: Modelling B;,* vol. 86, no. 1, pp. 312 - 320, 2017.

[92] K. Umetsu, R. Furutnani, S. Osawa, T. Takatsuji and T. Kurosawa, "Geometric calibration of a coordinate measuring machine using a laser tracking system," *Measurement Science and Technology,* vol. 16, no. 12, pp. 2466 - 2472, 2005.

[93] G. Dai, M. Neugebauer, M. Stein, S. Butefisch and U. Rube-Neuschaefer, "Overview of 3D Micro- and Nanocoordinate Metrology at PTB," *Applied Sciences,* vol. 6, no. 257, pp. 1 - 17, 2016.

[94] D. Kim, K. Kim, S. H. Park and S. Jang, "Calibration of the straightness and orthogonality error of a laser feedback high-precision stage using self-calibration methods," *Measurement Science and Technology,* vol. 25, pp. 1 - 10, 2014.

[95] T. Lai, X. Peng, J. Liu, G. Tie and M. Guo, "High accurate measurement and calibration of the squareness on ultra-precision machine based on error separation," in *Proceedings of the institution of Mechanical Engineers, Part B:,* 2017.

[96] W. T. Estler, "Calibration and use of optical straightedges in the metrology of precision machines," *Optical Engineering,* vol. 24, no. 3, pp. 372-379, 1985.

[97] N. Chanthawong, S. Takahashi and H. Matsumoto, "High accuracy calibration of CMM using temporal-coherence fiber interferometer with fast-repetition comb laser," *Key Engineering Materials,* vol. 625, pp. 66 - 72, 2014.

[98] S. Ruffa, G. D. Panciani, F. Ricci and G. Vicario, "Assessing measurement uncertainty in CMM measurements comparison of different approaches," *Journal of Metrology and Quality Engineering,* vol. 4, no. 4, pp. 163 - 168, 2013.

[99] Joint Committee for Guides in Metrology, *Evaluation of measurement data-guide to the expression of uncertainty in measurement,* 2008.

[100] A. Jalid, S. Hariri, A. El Gharad and J. P. Senelaer, "Comparison of the GUM and Monte Carlo methods on the flatness uncertainty estimation in coordinate measuring machine," *International Journal of Metrology and Quality Engineering,* vol. 7, no. 3, p. 302, 2016.

[101] D. Heibelmann, M. Franke, K. Rost, K. Wendt, T. Kistner and C. Schwehn, "Determination of measurement uncertainty by Monte Carlo simulation," in *WSPC Proceedings*, Braunschweig, Germany, 2019.

[102] R. G. Wilhelm, R. Hocken and H. Schwenke, "Task specific uncertainty in coordinate measurement," *CIRP,* vol. 50, no. 2, pp. 553 - 563, 2001.

[103] B. Strbac, V. Radlovacki, B. Acko, J. V. Spasic, L. Zupunski and M. Hadzistevic, "The use of Monte Carlo simulation in evaluating the uncertainty of flatness measurement on a cmm," *Journal of Production Engineering,* vol. 19, no. 2, pp. 69 - 72, 2016.

[104] J. Caja, P. Maresca and E. Gomez, "A model to determinate the influence of probability density function (PDFs) of input quantities in measurments.," *Applied Science,* vol. 6, no. 7, p. 190, 2016.

[105] Joint Committee for Guides in Metrology, *Evaluation of measurement data — Supplement 1 to the "Guide to the expression of uncertainty in measurement" Propagation of distributions using a Monte Carlo method,* 2008.

[106] P. R. Guimaaraes Couto, J. C. Damasceno and P. S. de Oliveira, "Monte Carlo Simulations Applied to Uncertainty in Measurement," in *Theory and Applications of Monte Carlo Simulations*, 2013, pp. 27 - 51.

[107] H. Kwawasaki, "Robot Kinematic and Dynamics," Japan.

[108] U. Akula, V. Nanavara and N. R. Bhumireddy, "A Review of Methods Used for Kinematic Modeling of a Manipulator," *International Journal of Mechanical Engineering and Technology,* vol. 8, no. 7, pp. 1854 - 1861, 2017.

[109] C. C. Obasi, I. A. Braimoh, V. A. Balogun, A. Odaba and L. I. Ogbewey, "Computational Analysis of Kinematics of 3-Links Articulated Robotic Manipulator," *International Journal of Engineering and Advanced Technology,* vol. 9, no. 2, pp. 2249 - 8958, December, 2019.

[110] L. Barinka and R. Berka, "Inverse kinematics-Basic Methods," *Central European Seminar on Computer Graphics,* 2002.

[111] K. W. Chase, J. Gao, S. P. Magleby and C. D. Sorensen, "Including Geometric Feature Variations in Tolerance Analysis of Mechanical Assemblies," *IIE Transections,* vol. 28, no. 10, pp. 795 - 807, 1996.

[112] Dejan, "How to Setup GRBL & Control CNC Machine with Arduino," How To Mechatronics, 2020. [Online]. Available: https://howtomechatronics.com/tutorials/how-to-setup-grbl-control-cnc-machine-with-arduino/. [Accessed 13 03 2022].

[113] S. Kucuk and Z. Bingul, "Robot Kinematics: Forward and Inverse Kinematics," in *Industrial Robotics: Theory, Modelling and Control*, InTech, 2006, pp. 117 - 148.

[114] A. Jansen, N. Rosielle and P. Schellekens, "A fully elastically guided 3-D CMM with a measuring volume of 1cm3," *Preceedings of the American Society of Precision Engineering,* vol. 20, pp. 452-455, 1999.

[115] J. F. Zhang, P. F. Feng, Z. J. Wu, D. W. Yu and C. Chen, "Thermal Structure Design and Analysis of a Machine Tool Headstock," *Mechanika,* vol. 19, no. 4, 2013.

Appendices

Appendix A: Novel CMM Design Drawings

Appendix A-1 : The side view, top view and the from view of the novel design

Appendix A-2 : Manipulation system with mirror table.

Appendix A-3 : Metrology Frame

Appendix A-1: The side view, top view, and the front view of the novel design
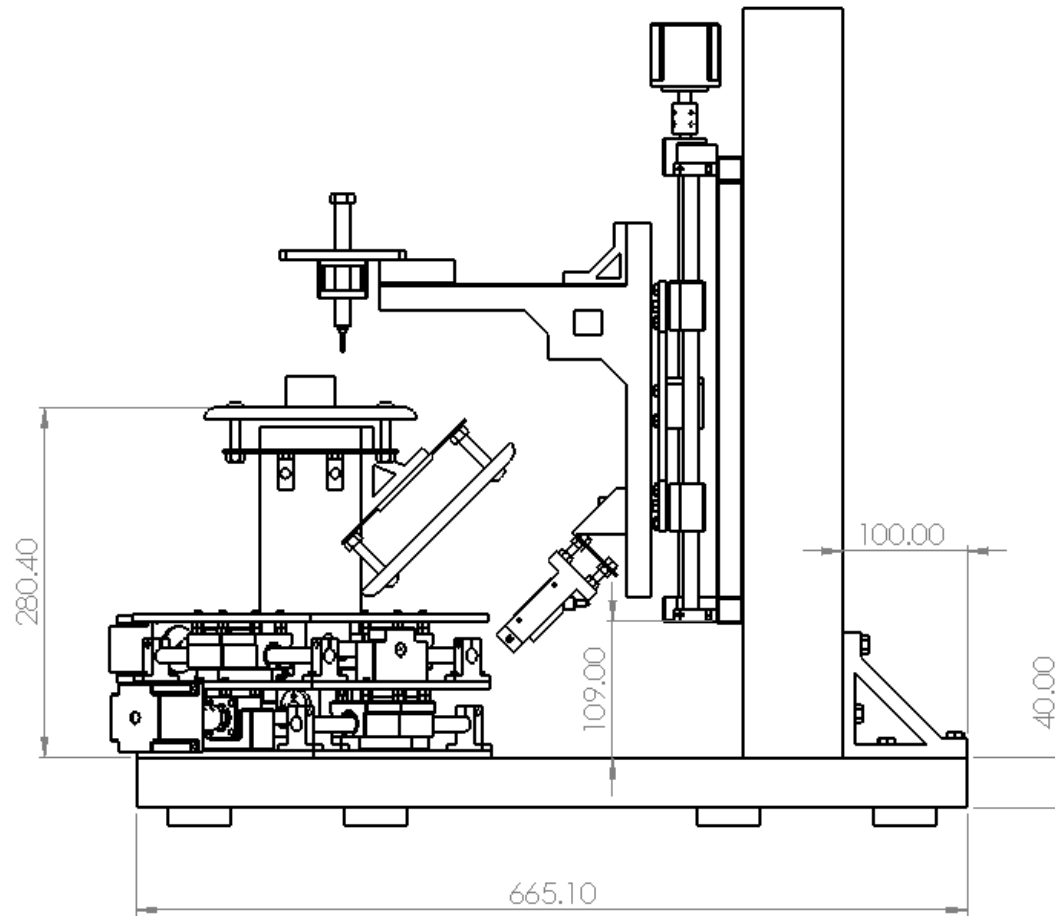
Side view dimensions
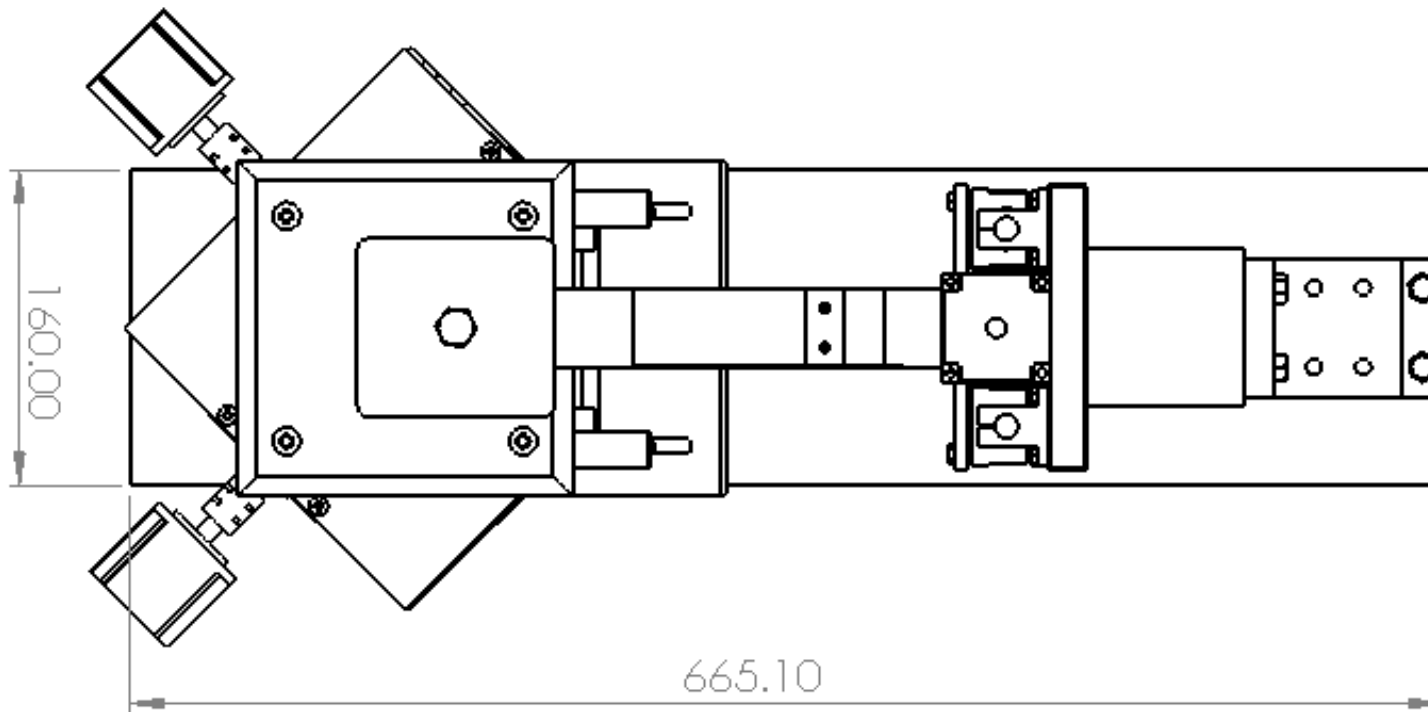
Top view dimensions of the design

600.00

160.00
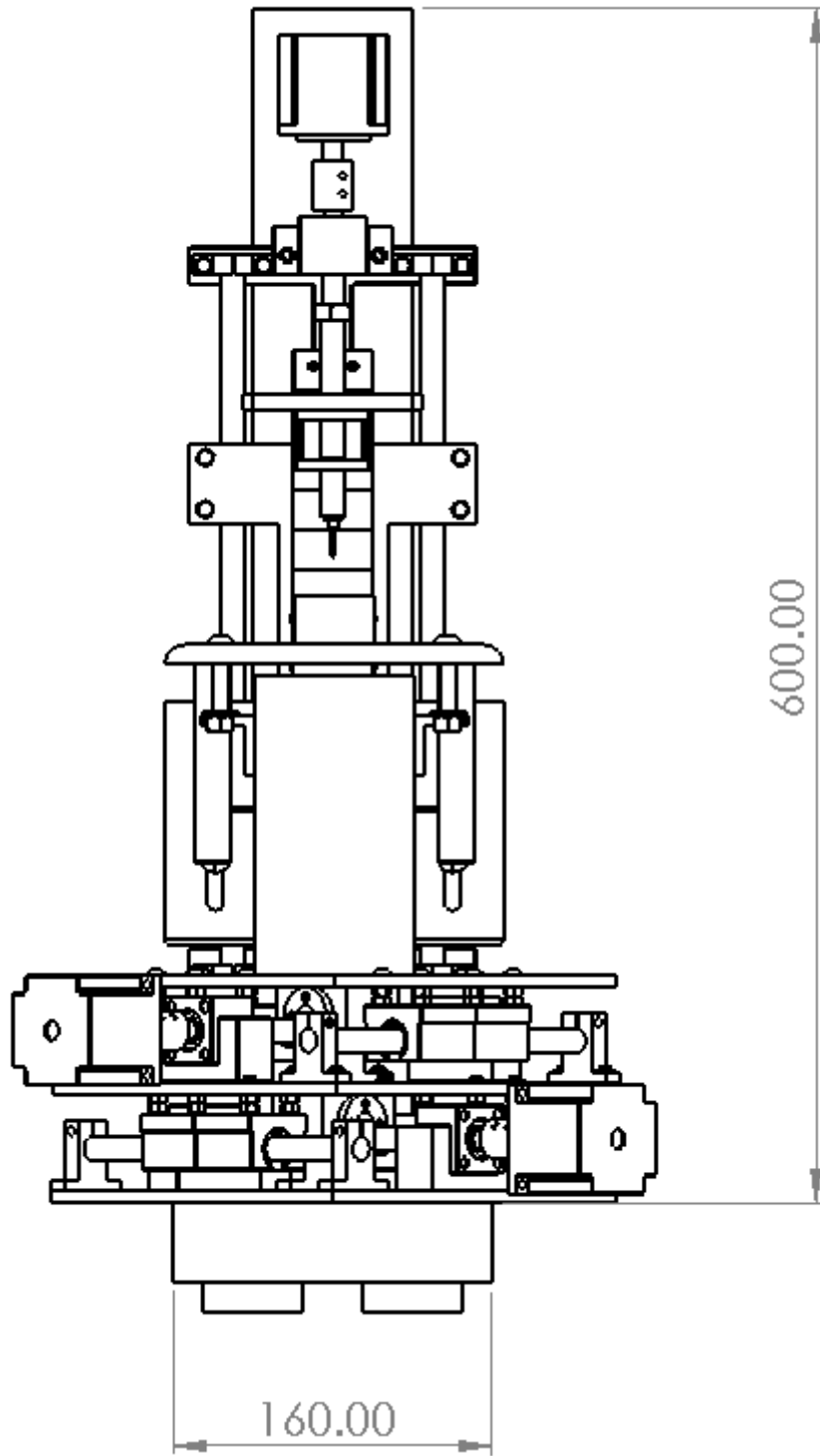
Front view

Appendix A-2: Manipulation system with mirror table.
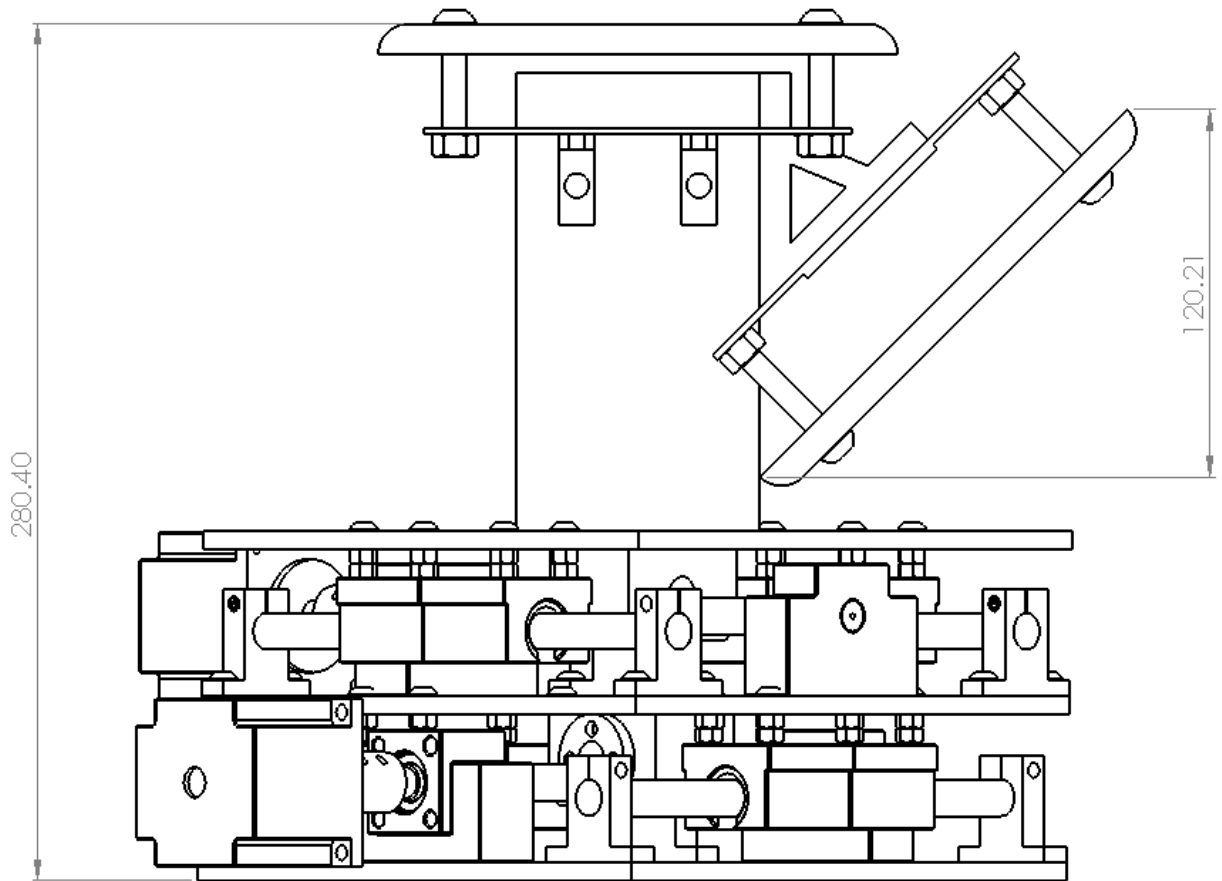
Manipulation system side view
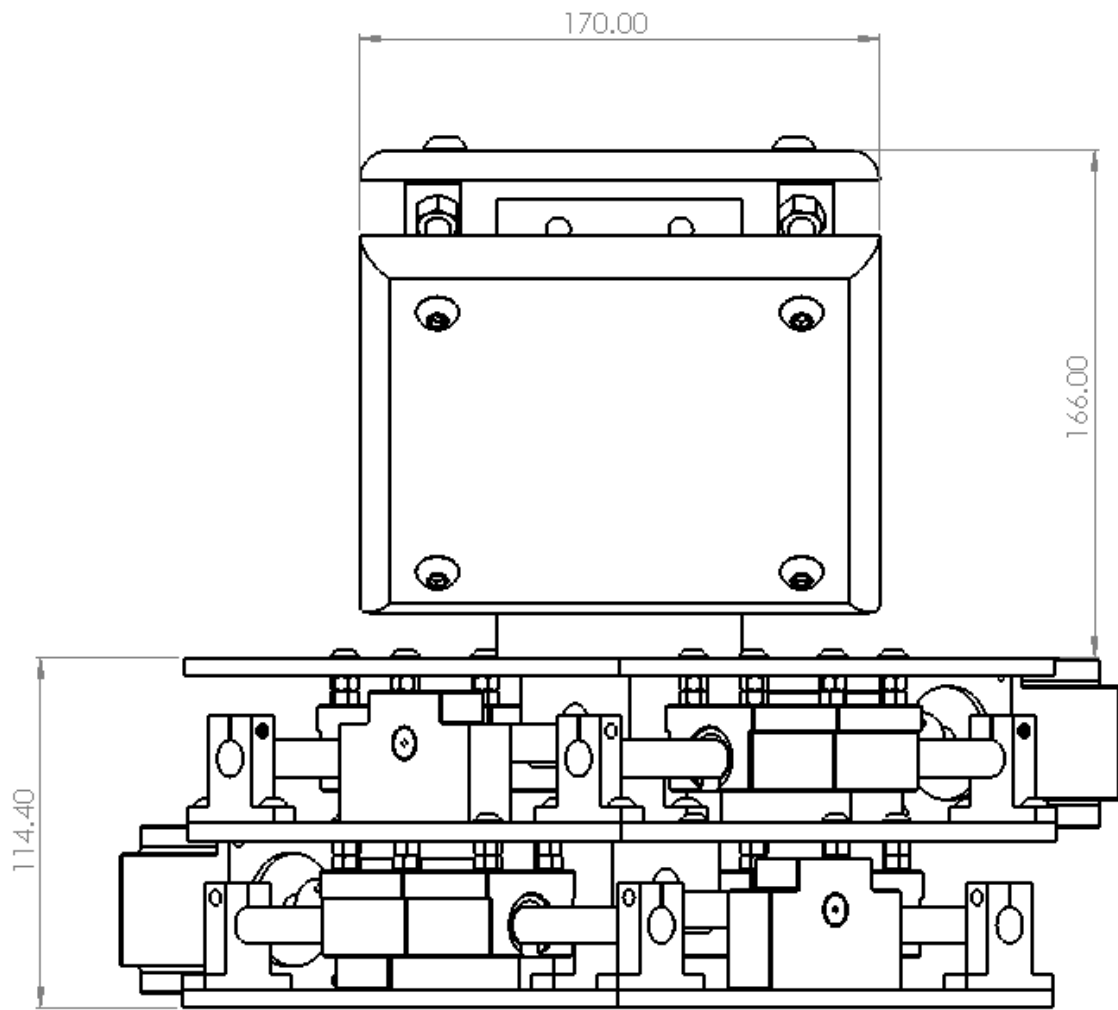
Manipulation system front view
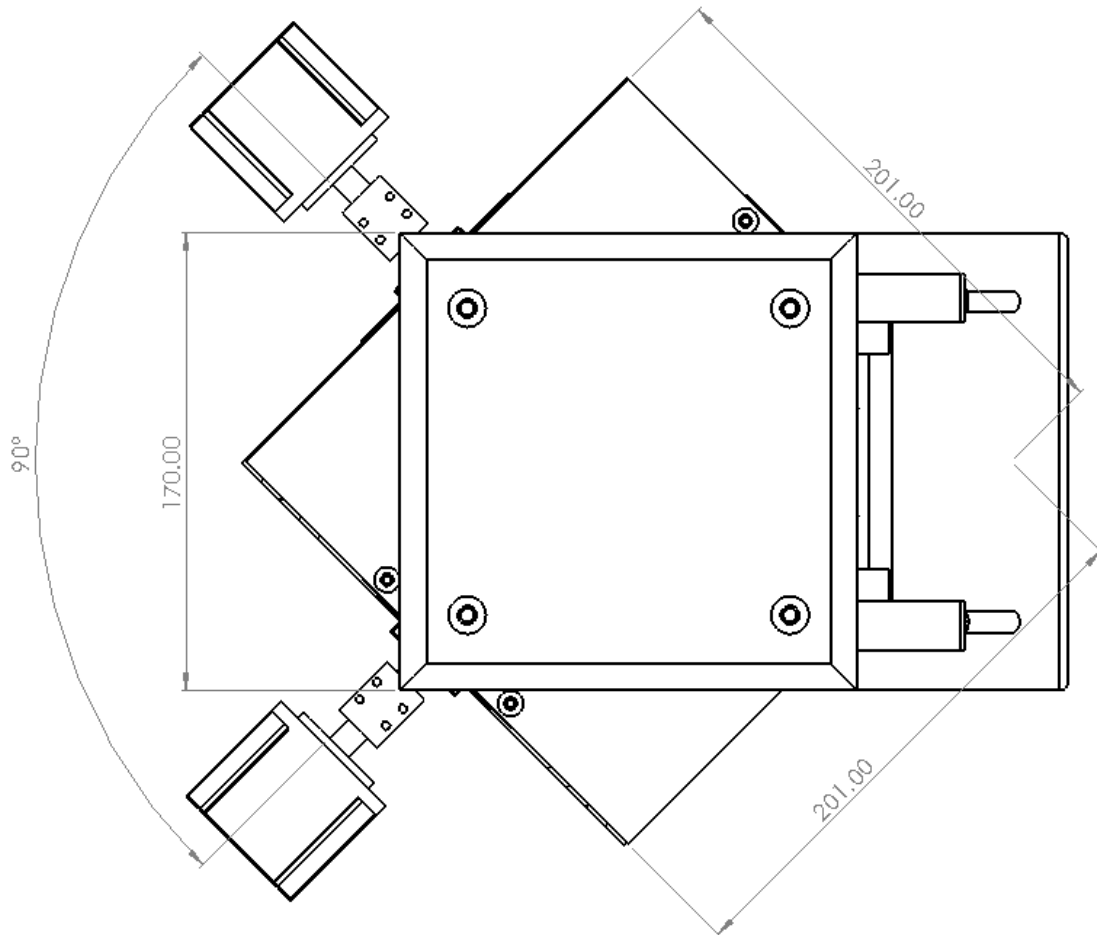
Manipulation system top view

Appendix A-3: Metrology Frame
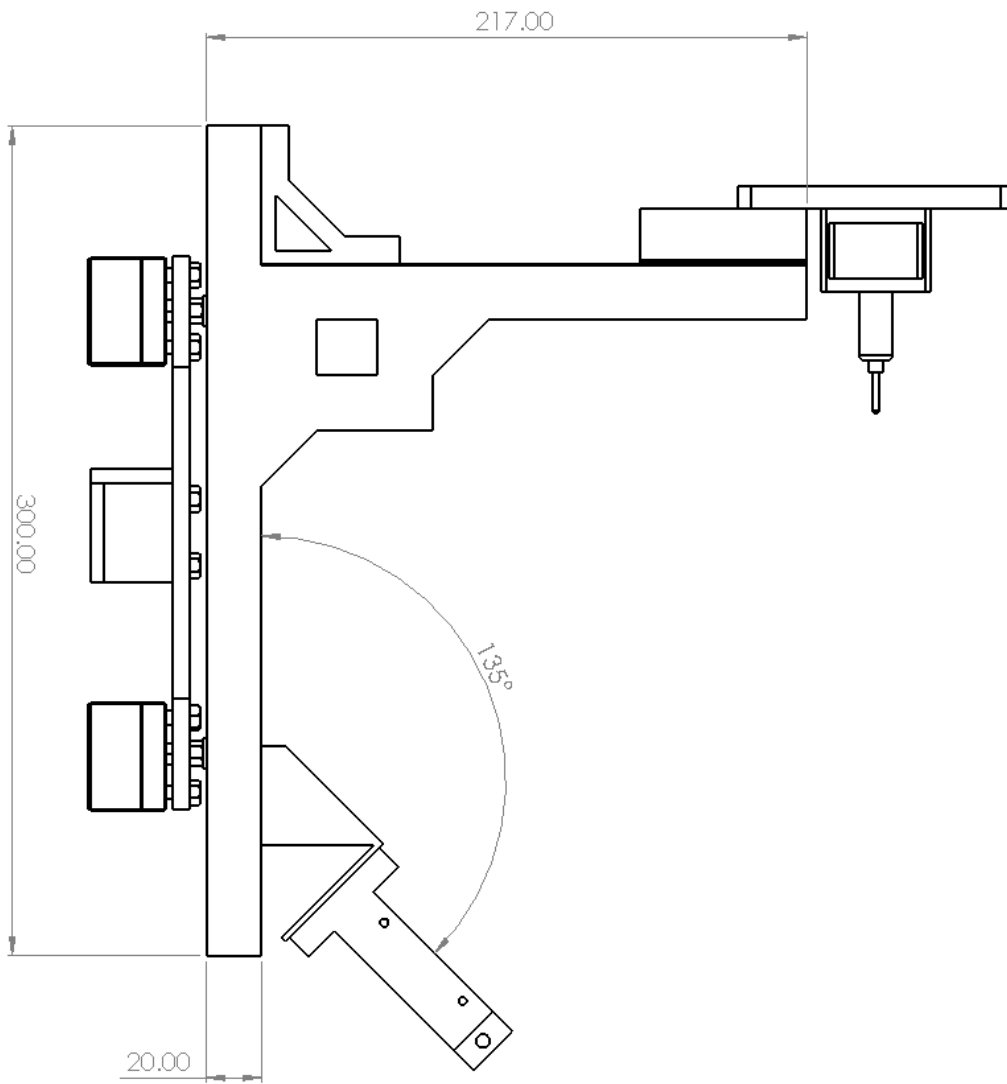
Metrology Frame

Appendix B: X-Y stage parts (Manipulation System)

Appendix B-1 : Stepper Motor Technical Details

Appendix B-2 : Ball Screw with Nut, Technical Details

Appendix B-3 : Ball Screw with Nut, Technical Details

Appendix B-4 : Linear chrome steel rod, Technical Details

Appendix B-1: Stepper motor technical details

 NEMA 23 stepper motors are used on bigger 3D printers and CNC machines. This is a high torque stepper motor and comes with 300mm leads.

The stepper driver we recommend with this motor is the MKS TB6600 or the Wantai DQ542MA stepper driver.

Specifications:

- Size: NEMA 23 (57mm x 57mm)
- Length: 51mm
- Step angle: 1.8 Degrees
- Rated voltage: 2.6V
- Current/Phase: 2.8A
- Resistance/Phase: 0.83 Ohm
- Inductance/Phase: 2.2 mH
- Holding Torque: 10.1 kg.cm (1.01 Nm)
- Number of leads: 4
- Weight: 0.61 kg
- Max Radial Force on output shaft: 75N (10mm from flange)
- Max Axial Force on output shaft: 15N
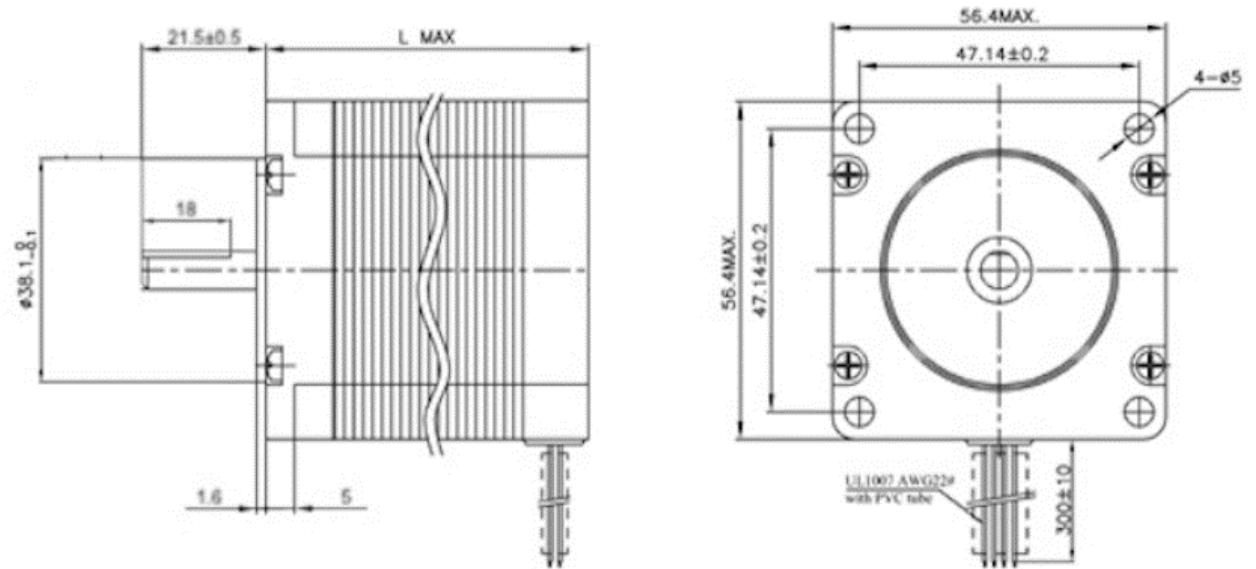
Appendix B-1: Ball screw with technical details

Ball screw with nut to transfer rotation movement into linear movement. This is a high-quality ball screw with machined ends for easy assembly to bearing blocks.

Specifications:

- Ball screw rod diameter: 12mm

- Pitch: 4mm per revolution

- Length from end to end: 400mm

- Effective travel length: 300mm

- Product code: SFU1204

- Static load rating: 6.7kN

- Dynamic load rating: 4.0kN

- Fixed end machined for BK10 or FK10 bearing block

- Floating end machined for FK10 or FF10 bearing block
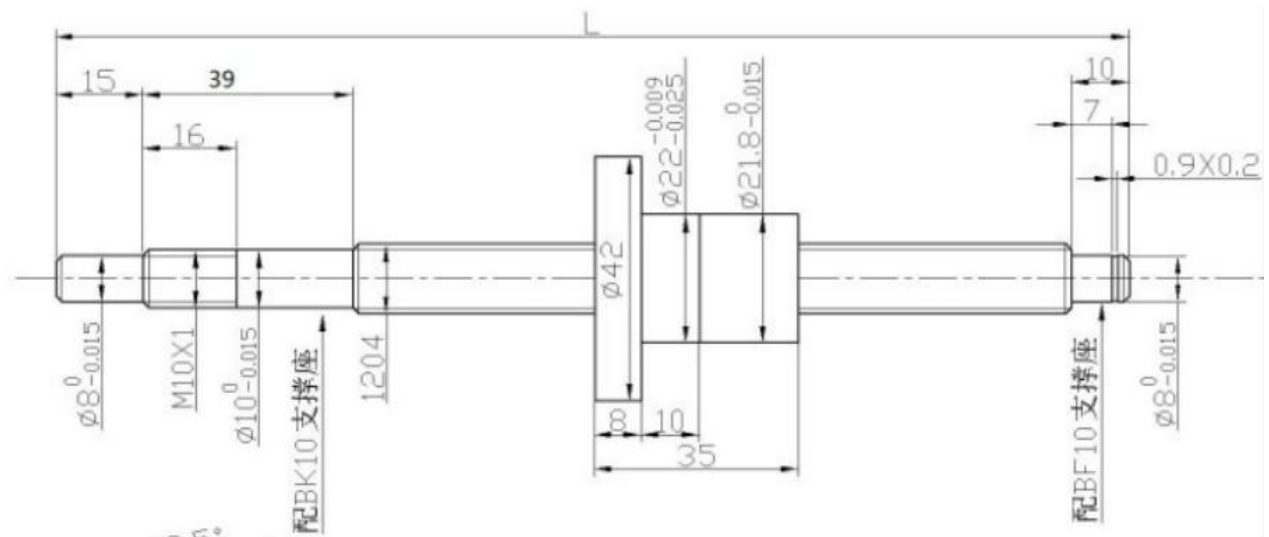
- Please see machining dimensions below:

Appendix B-3: Linear bearing with housing SBR12UU

- The SBR12UU bearing is a linear ball bearing with aluminum housing used on a 12mm supported linear shaft for accurate linear motion. The aluminum housing has 4 tapped holes at the bottom for easy mounting to plate or bracket.
- It is generally used on 3D printers and CNC machines. The main advantage of the supported rails is that it is a lot stronger, because it is supported all the way along the rod and not just at the ends. These bearings have proven to be long lasting and provide precise low friction linear movement. General maintenance required is to clean the shafts occasionally and keep the shafts lightly oiled or greased.
- There are two grub screws on each bearing, one at the top and one on the side. These two grub screws are used to set the play of the bearing on the shaft. Both these grub screws are tightened in the factory to make sure they do not fall out during shipping. This means the grub screws must be adjusted to ensure smooth linear motion on the shaft it is fitted to.
- Specifications:

- Model number SBR12UU

- Designed for supported linear shaft: 12mm

- Dynamic load rating = 420kg

- Static load rating = 610kg
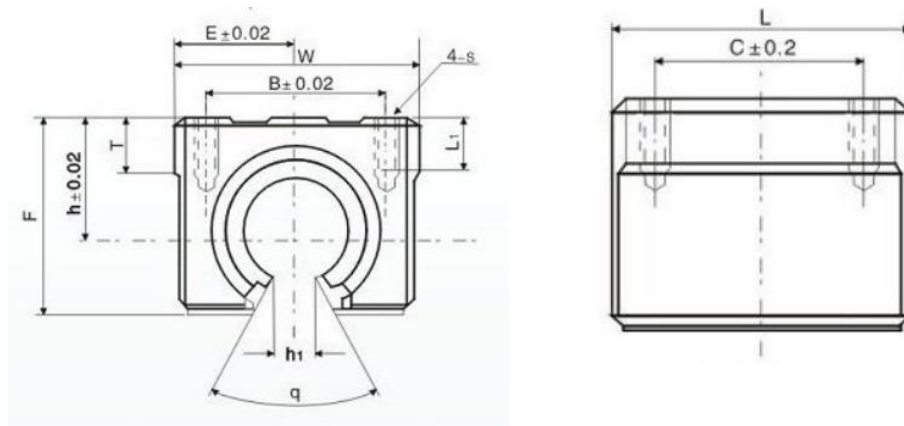
滑块型号 Unit Designation	主要尺寸 Dimensions (mm)												配合直线轴承Slide bush			重量 weight (g)
	h	E	W	L	F	h1	q	B	C	S	L1	T	型号 Designation	基本负荷率 Basic load rating dynamic C (kgf)	static Co(kgf)	
SBR 10UU	15	18	36	32	24	6	80°	25	20	M5	10	7	LM10UU–OP	372	549	65
SBR 12UU	17.5	20.5	41	39	28	7.5	80°	28	26	M5	10	9	LM12UU–OP	420	610	100

Appendix B-4: Linear chrome steel rod

Linear chromed steel rod for linear motion used on 3D Printers and CNC machines. High quality surface finish for low friction, accurate silent linear movement. To be used with 12mm linear bearings.

Specifications:

- Diameter: 12mm

- Length: 1000mm

- Material: GCr15 Steel

- Surface treatment: Chromed

- Surface hardness: HRC60 - 62

- Diameter tolerance: g6 (please see table below)

- Surface finish tolerance: 0.4 micron

Appendix C: Technical details of 1320-100 displacement sensor

Appendix C-1: Micro-Epsilon ILD 1320-100 Calibration Certificate

Kalibrierprotokoll Ausgang
Calibration final inspection
optoNCDT

MICRO-EPSILON

Modell	Model	ILD1320-100
Serien-Nr.	Serial-no.	21040047
Messbereich [mm]	Measuring range [mm]	100
geprüft von	Tested by	JJO
Datum	Date	2021-05-06

Legend: Deviation in % — Upper limit — Lower limit

X-axis: Weg / Displacement [mm]
Y-axis: Linearit. - Abweichung / Linearity Deviation [%]

Dieser Prüfbericht gilt für die angegebene Systemzusammenstellung (DT251).
Messobjekt für den Test: Keramik weiss und eben
Die ermittelte Kennlinie ist als Werkskalibrierung im System hinterlegt.
Abweichungen von diesen Daten können auftreten durch:
- Rauigkeit der Oberfläche
- Sensormontage (Verkippung)
- Temperaturschwankungen während der Messung
- Zirkulation warmer Luft zwischen Sensor und Messobjekt
- abweichende Reflexionseigenschaften der Oberfläche
Für weitere Informationen beachten Sie bitte die Hinweise in der Bedienungsanleitung.

This Test Report is valid for the reported system configuration (DT251).
Target: white ceramic (flat)
The above characteristics is stored as factory calibration.
Differneces of these data can appear because of:
- roughness of surface
- sensor mounting (tilt)
- fluctuations of temperature during the measurement
- circulation of hot air between sensor and target
- deviation of reflection attribute of surface
Further the statements in the operating manual is valid.

MICRO - EPSILON - Messtechnik GmbH / Königbacher Str. 15 / D 94496 Ortenburg
Tel.: +49 / 8542 / 168 - 0; Fax: +49 / 8542 / 168 - 90; e-mail: info@micro-epsilon.de; http://www.micro-epsilon.com

1 / 1

136

Appendix C-2: Dimensional drawing and free space for optics and optical free space
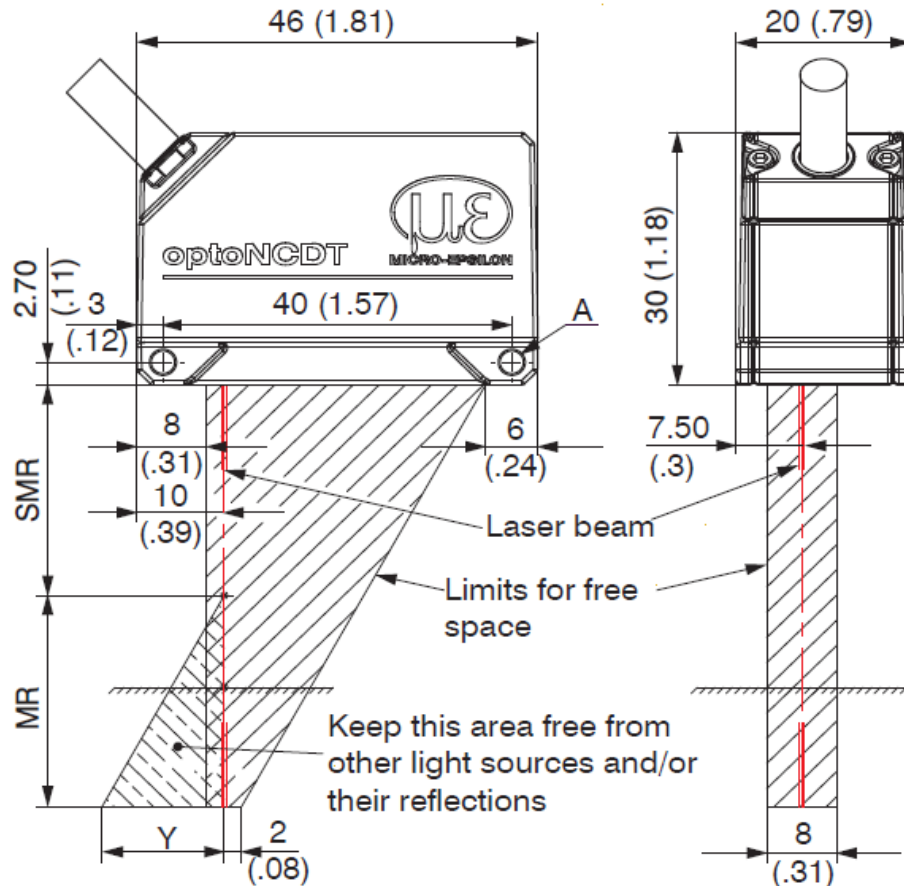
ILD 1320-		10	25	50	100
MR	mm	10	25	50	100
SMR	mm	20	25	35	50
EMR	mm	30	50	85	150
Y	mm	10	21	28	46

The indicated free space in the reception area, see Fig. 10, has to be kept clear from foreign objects and extraneous light of other laser sensors at least until the end of measuring range.

MR = Measuring range
SMR = Start of measuring range
MMR = Mid of measuring range
EMR = End of measuring range
FSO = Full scale output

Appendix C-3: Technical Data

Model	ILD1320-10	ILD1320-25	ILD1320-50	ILD1320-100	Available for OEM series ILD1320-200
Measruing range	10 mm	25 mm	50 mm	100 mm	200 mm
Start of measuring range	20 mm	25 mm	35 mm	50 mm	60 mm
Mid of measuring range	25 mm	37.5 mm	60 mm	100 mm	160 mm
End of measuring range	30 mm	50 mm	85 mm	150 mm	260 mm
Measuring rate [1]	4 adjustable stages: 2 kHz / 1 kHz / 0.5 kHz / 0.25 kHz				
Linearity	$< \pm 10 \, \mu m$	$< \pm 25 \, \mu m$	$< \pm 50 \, \mu m$	$< \pm 100 \, \mu m$	$< \pm 200 \, \mu m$
	$< \pm 0.10 \, \%$ FSO				
Repeatability [2]	$1 \, \mu m$	$2.5 \, \mu m$	$5 \, \mu m$	$10 \, \mu m$	$20 \, \mu m$
Temperature stability	$\pm 0.015 \, \%$ FSO / K			$\pm 0.01 \, \%$ FSO / K	
Light spot diameter (±10 %) — SMR	$90 \times 120 \, \mu m$	$100 \times 140 \, \mu m$	$90 \times 120 \, \mu m$	$750 \times 1100 \, \mu m$	
MMR	$45 \times 40 \, \mu m$	$120 \times 130 \, \mu m$	$230 \times 240 \, \mu m$		
EMR	$140 \times 160 \, \mu m$	$390 \times 500 \, \mu m$	$630 \times 820 \, \mu m$		
smallest ø	$45 \times 40 \, \mu m$ with 24 mm	$55 \times 50 \, \mu m$ with 31 mm	$70 \times 65 \, \mu m$ with 42 mm	-	
Light source	Semiconductor laser <1 mW, 670 nm (red)				
Laser safety class	Class 2 in accordance with IEC 60825-1: 2014				
Permissible ambient light [3]	30,000 lx			20,000 lx	7,500 lx
Supply voltage	11 ... 30 VDC				
Power consumption	< 2 W (24 V)				
Signal input	1 x HTL laser on/off; 1 x HTL multifunction input: trigger in, zero setting, mastering, teach				
Digital interface	RS422 (16 bit) / PROFINET [4] / EtherNet/IP [4]				

Appendix C-4: Connection possibilities
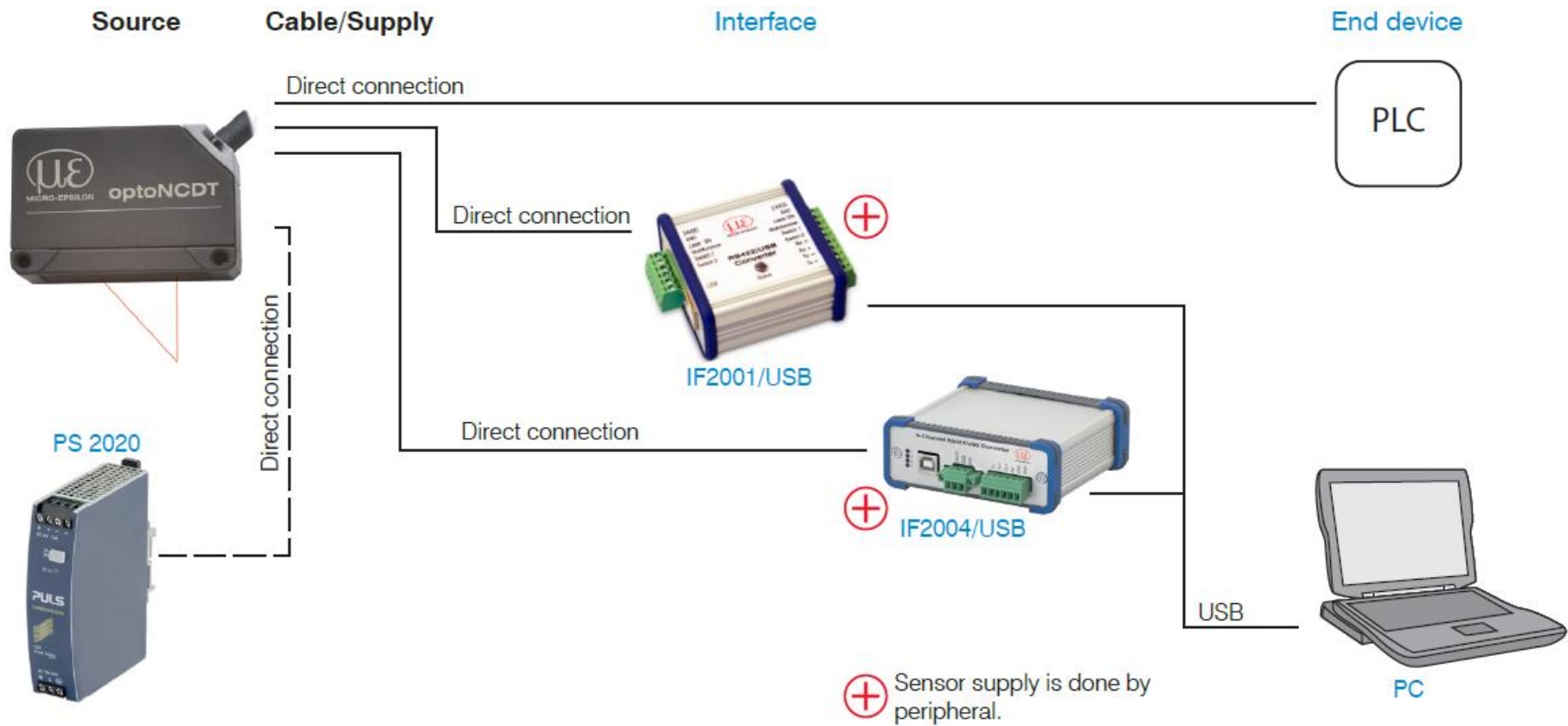
Appendix C-5: Pin Assignment

Signal	Color sensor cable	Description	Specification
RS422 Rx+	green	Serial input	Internally terminated with 120 Ohm
RS422 Rx-	yellow		
RS422 Tx+	gray	Serial output	Terminate externally with 120 Ohm
RS422 Tx-	pink		
$+U_B$	red	Supply voltage	11 ... 30 VDC, typ. 24 VDC, P < 2 W
Laser on/off	black	Switch input	Laser is active, if input is connected with GND
Functional input	violet		Trigger, Zero/Master, Teaching
Error	brown	Digital output	I_{max} = 100 mA, U_{max} = 30 VDC, Programmable switching characteristic: (NPN, PNP, Push-Pull)
I_{OUT}	white	4 ... 20 mA	R_{Load} = 250 Ohm: U_{OUT} 1 ... 5 V with U_B > 11 V R_{Load} = 500 Ohm: U_{OUT} 2 ... 10 V with U_B > 17 V
GND	blue	Ground potential	Supply and signal ground
Connector housing	Shield	Sensor housing	Connect with potential equalization

Appendix C-6: The indicator elements at sensor

LED State	Meaning
green	Measuring object within sensor range
yellow	Mid range
red	Error - e.g. Poor target or out of range
off	Laser off

LED Output	Meaning
green	RS422 measurement value output
yellow	RS422 and current output are switched off. The RS422 and the current output can be switched on. Web interface can also be switched on.
red	Current 4 ... 20 mA measurement value output
off	Sensor off, no supply
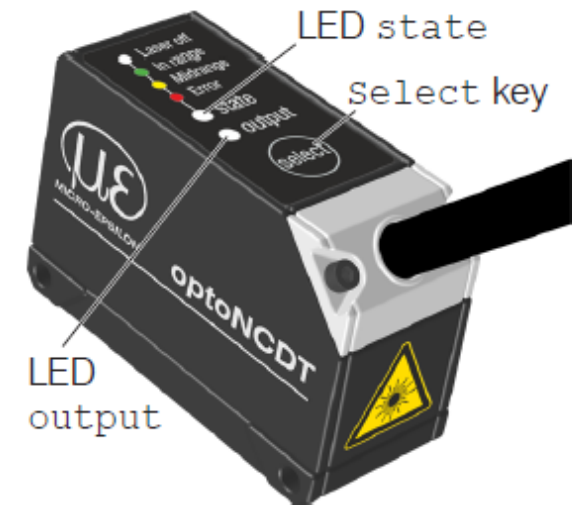
Appendix D: Technical details of Renishaw TP20 probe

Appendix D-1 : TP20 System

Appendix D-2 : Technical Data

Appendix D-1: TP20 System

- A kinematic, module changing touch-trigger probe system for manual and DCC CMMs
- Rapid exchange (manually or automatically) between stylus configurations without the need to re-calibrate
- Direct replacement for TP2-5W probe
- A choice of seven stylus modules, giving 5 or 6-axis operation, allow optimisation of probe and stylus performance for each application
- Easily retrofitted to all Renishaw standard probe heads (M8 or autojoint) and compatible with existing TTP interfaces
- Metrology performance equivalent to TP2-5W probe
- Compatible with the full range of Renishaw probe heads and accessories

Appendix D-2: TP20 Technical Specification

Product compatibility	The TP20 is suitable for use with all Renishaw probe interfaces and probe heads which service the TP1, TP2 and TP6 touch-trigger probes. The TP20 is compatible with the PEL, PK, PAA and PEM series of probe extensions / adaptors.
Diameter	13.2 mm
Length - LF / SF / MF / EF	38 mm
Length - EM1 STD	88 mm
Length - EM2 STD	113 mm
Length - 6-way	42 mm
Probe mount	Thread M8 x 1.25 x 5 mm
Stylus mount	Thread M2 x 0.4
Sense directions - LF / SF / MF / EF / EM1 STD / EM2 STD	5-way (± X, ± Y, + Z)
Sense directions - 6-way	6-way (± X, ± Y, ± Z)
Probe module pull-off force	10 N (1 kgf) maximum
Sealing	IP30
Cable length	50 m with (24 awg) conductors
Probe modules life	25,000 changes

Appendix E: Random calibration samples

Appendix E-1 : Random samples before calibration

Appendix E-2 : Random samples after calibration

Appendix E-1: Samples before the calibration

Table 0-1: Samples before calibration during x-axis translation

Samples	L_0 (mm)	L_{0x} (mm)	Tm (mm)	e_x (mm)	Mirror angle (degrees)
1	91.387	66.531	50.000	-0.329	44.671
2	91.396	66.671	50.000	-0.630	44.370
3	91.409	66.602	50.000	-0.441	44.559
4	91.386	66.683	50.000	-0.680	44.320
5	91.403	66.444	50.000	-0.094	44.906
6	91.396	66.457	50.000	-0.139	44.861
7	91.401	66.634	50.000	-0.535	44.465
8	91.403	66.532	50.000	-0.296	44.704
9	91.397	66.490	50.000	-0.213	44.787
10	91.410	66.445	50.000	-0.081	44.919
11	91.388	66.709	50.000	-0.735	44.265
12	91.386	66.377	50.000	0.020	45.020
13	91.399	66.605	50.000	-0.472	44.528
14	91.407	66.577	50.000	-0.390	44.610

Table 0-2: Samples before calibration during y-axis translation

Samples	L_0 (mm)	L_{0y} (mm)	Tm (mm)	e_y (mm)	Mirror angle (degrees)
1	91.342	66.440	50.000	-0.226	44.774
2	91.325	66.630	50.000	-0.699	44.301
3	91.317	66.448	50.000	-0.300	44.700
4	91.344	66.409	50.000	-0.148	44.852
5	91.336	66.430	50.000	-0.215	44.785
6	91.332	66.544	50.000	-0.487	44.513
7	91.342	66.377	50.000	-0.081	44.919
8	91.335	66.701	50.000	-0.839	44.161
9	91.329	66.652	50.000	-0.740	44.260
10	91.340	66.379	50.000	-0.090	44.910
11	91.325	66.499	50.000	-0.398	44.602
12	91.320	66.645	50.000	-0.746	44.254
13	91.322	66.641	50.000	-0.730	44.270
14	91.344	66.412	50.000	-0.156	44.844

Table 0-3: Samples before calibration during z-axis translation

Samples	L_0 (mm)	L_{0y} (mm)	T_m (mm)	e_z (mm)	Mirror angle (degrees)
1	96.685	61.543	50.000	-0.389	44.611
2	96.659	61.548	50.000	-0.402	44.598
3	96.683	61.546	50.000	-0.358	44.642
4	96.661	61.542	50.000	-0.339	44.661
5	96.669	61.538	50.000	-0.396	44.604
6	96.674	61.547	50.000	-0.347	44.653
7	96.692	61.537	50.000	-0.322	44.678
8	96.657	61.541	50.000	-0.370	44.630
9	96.657	61.539	50.000	-0.381	44.619
10	96.672	61.545	50.000	-0.387	44.613
11	96.670	61.545	50.000	-0.334	44.666
12	96.665	61.546	50.000	-0.403	44.597
13	96.671	61.539	50.000	-0.389	44.611
14	96.661	61.543	50.000	-0.342	44.658

Appendix E-2: Samples after the calibration

Table 0-4; Samples after calibration during x-axis translation

x-axis	Laser displacement measured value at original position	Component of the laser displacement before translation	Distance travelled by the surface of the mirror	Laser displacement value when traslated	Component of the laser displacement when translated
	L_0	L_2	Tm_x	L_{0x}	L_{2x}
1	91.388	129.242	50.000	66.399	93.902
2	91.411	129.275	50.000	66.394	93.895
3	91.390	129.245	50.000	66.379	93.874
4	91.386	129.239	50.000	66.395	93.897
5	91.397	129.255	50.000	66.376	93.870
6	91.398	129.256	50.000	66.387	93.885
7	91.386	129.239	50.000	66.392	93.892
8	91.400	129.259	50.000	66.386	93.884
9	91.388	129.242	50.000	66.378	93.873
10	91.377	129.227	50.000	66.389	93.888
Aver	91.392	129.248	50.000	66.388	93.886
Max	91.411	129.275	50.000	66.399	93.902
Min	91.377	129.227	50.000	66.376	93.870
Diff	0.034	0.048	0.000	0.023	0.033

Table 0-5: Samples after calibration during y-axis translation

y-axis	Laser displacement measured value at original position	Component of the laser displacement before translation	Distance travelled by the surface of the mirror	Laser displacement value when traslated	Component of the laser displacement when translated
	L_0	L_2	Tm_y	L_{0y}	L_{2y}
1	91.325	129.153	50.000	66.336	93.813
2	91.347	129.184	50.000	66.337	93.815
3	91.331	129.162	50.000	66.340	93.819
4	91.343	129.179	50.000	66.332	93.808
5	91.326	129.154	50.000	66.341	93.820
6	91.325	129.153	50.000	66.315	93.784
7	91.322	129.149	50.000	66.315	93.784
8	91.316	129.140	50.000	66.333	93.809
9	91.323	129.150	50.000	66.311	93.778
10	91.323	129.150	50.000	66.332	93.808
Aver	91.328	129.157	50.000	66.329	93.804
Max	91.347	129.184	50.000	66.341	93.820
Min	91.316	129.140	50.000	66.311	93.778
Diff	0.031	0.044	0.000	0.030	0.042

Table 0-6: Samples after calibration during z-axis translation

z-axis	Laser displacement measured value at original position	Component of the laser displacement before translation	Distance travelled by the surface of the mirror	Laser displacement value when traslated	Component of the laser displacement when translated
	L_0	L_2	Tm_z	L_{0z}	L_{2z}
1	96.668	136.709	50.000	61.313	86.710
2	96.655	136.691	50.000	61.310	86.705
3	96.669	136.711	50.000	61.307	86.701
4	96.672	136.715	50.000	61.315	86.713
5	96.665	136.705	50.000	61.321	86.721
6	96.661	136.699	50.000	61.313	86.710
7	96.658	136.695	50.000	61.313	86.710
8	96.652	136.687	50.000	61.311	86.707
9	96.673	136.716	50.000	61.302	86.694
10	96.668	136.709	50.000	61.308	86.703
Aver	96.664	136.704	50.000	61.311	86.707
Max	96.673	136.716	50.000	61.321	86.721
Min	96.652	136.687	50.000	61.302	86.694
Diff	0.021	0.030	0.000	0.019	0.027

Samples taken after the calibration

Appendix F: Drawings of the measured part

Appendix F-1 : The drawings of the Halcon Gauge

Appendix F-2 : The measurement results from Executive Engineering Company.
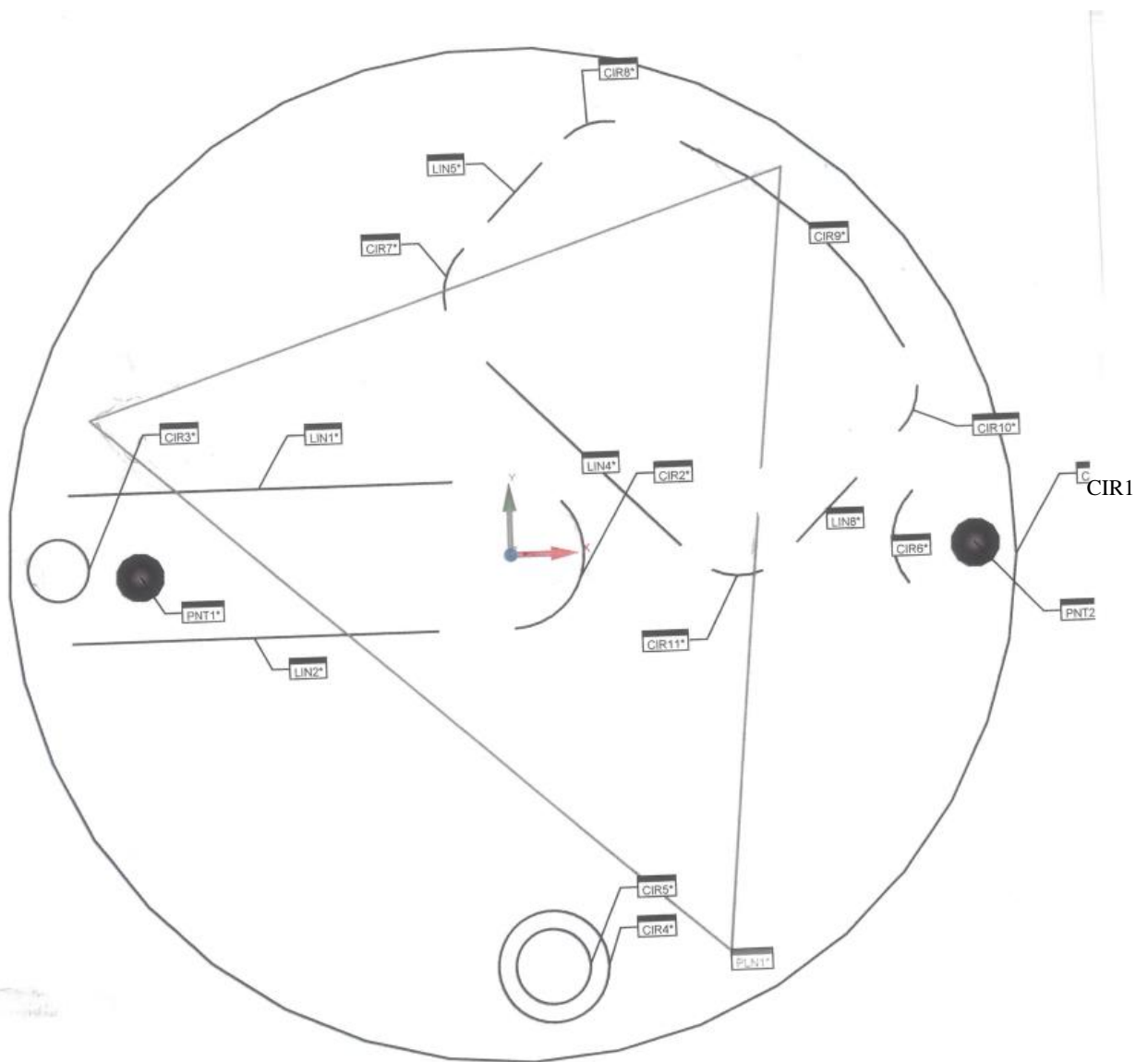
			PART NAME :	Halcon Gauges			February 18, 2022	10:42
Pc		REV NUMBER :			SER NUMBER :		STATS COUNT :	1

⊕	MM	LOC1 - CIR1						
AX		NOMINAL	+TOL	-TOL	MEAS	DEV	OUTTOL	
D		40.900	0.050	-0.050	40.904	0.004	0.000	

⊕	MM	LOC2 - CIR2						
AX		NOMINAL	+TOL	-TOL	MEAS	DEV	OUTTOL	
D		6.000	0.050	-0.050	5.976	-0.024	0.000	

⊕	MM	LOC3 - CIR3						
AX		NOMINAL	+TOL	-TOL	MEAS	DEV	OUTTOL	
D		2.500	0.050	-0.050	2.518	0.018	0.000	

⊕	MM	LOC4 - CIR4						
AX		NOMINAL	+TOL	-TOL	MEAS	DEV	OUTTOL	
D		4.500	0.050	-0.050	4.507	0.007	0.000	

⊕	MM	LOC5 - CIR5						
AX		NOMINAL	+TOL	-TOL	MEAS	DEV	OUTTOL	
D		3.000	0.050	-0.050	3.026	0.026	0.000	

⊕	MM	LOC6 - CIR6						
AX		NOMINAL	+TOL	-TOL	MEAS	DEV	OUTTOL	
D		5.500	0.050	-0.050	5.509	0.009	0.000	

⊕	MM	LOC7 - CIR7						
AX		NOMINAL	+TOL	-TOL	MEAS	DEV	OUTTOL	
D		5.100	0.050	-0.050	5.066	-0.034	0.000	

⊕	MM	LOC8 - CIR8						
AX		NOMINAL	+TOL	-TOL	MEAS	DEV	OUTTOL	
D		5.100	0.050	-0.050	5.105	0.005	0.000	

⊕	MM	LOC9 - CIR9						
AX		NOMINAL	+TOL	-TOL	MEAS	DEV	OUTTOL	
D		35.800	0.050	-0.050	35.814	0.014	0.000	

⊕	MM	LOC10 - CIR10						
AX		NOMINAL	+TOL	-TOL	MEAS	DEV	OUTTOL	
D		5.000	0.050	-0.050	4.992	-0.008	0.000	

⊕	MM	LOC11 - CIR11						
AX		NOMINAL	+TOL	-TOL	MEAS	DEV	OUTTOL	
D		5.000	0.050	-0.050	4.946	-0.054	0.004	

↔	MM	DIST1 - LIN2 TO LIN1 (YAXIS)						
AX		NOMINAL	+TOL	-TOL	MEAS	DEV	OUTTOL	
M		6.000	0.010	-0.010	6.005	0.005	0.000	

152